Sensing Applications of Nanomechanical Resonators

by

Muhammad Ruhul Amin

A thesis submitted in partial fulfilment of the requirements for the degree of

Master of Science

Department of Physics

University of Alberta

©Muhammad Ruhul Amin, 2017

Abstract

Nanomechanical resonators are explored as mass sensors and molecular sensors due to their high sensitivity and real time label-free detection ability, respectively. One downside of mechanical molecular sensing is the lack of chemical information carried in the signal. For this reason, a secondary technique such as functionalized surface, gas chromatography, or photothermal spectroscopy, must be combined with mass sensing for chemical specificity. As an alternative to this approach, we have developed a metallized nanomechanical resonator, capable of electrical local heating. Here, we explore the use of local temperature as a secondary molecular indicator similar to thermogravimetric analysis. In the present study, we explore the desorption of a polymer from these electrical nanostring sensors above room temperature and the adsorption of acetone below room temperature.

To my dear wife Nazia and my lovely son Rafsan.

Acknowledgements

I would like to thank all the people who contributed in some way to the work described in this thesis. Most importantly, I express my profound gratitude to my honourable supervisor, Professor John P. Davis for believing in me and giving me the opportunity to study in this great country. During my two years in his group, he generously provided me with support, inspiration, guidance, encouragement, and the freedom to pursue this research. I am grateful for the opportunity he has given me by taking on the role of my supervisor. As a foreign student, I am extremely happy to experience the very collaborative and supportive environment he has cultivated in the entire group. I would like to thank my committee members, Professor John Beamish, Professor Lindsay J. LeBlanc, and Professor Joseph Maciejko for their guidance and serving in my exam committee.

I am grateful to the other members in the Davis lab who were not just my colleagues during the last two years, but also my teammates and friends. Firstly, I am very thankful to Tushar Shuvra Biswas, who worked on the same nanostring project. He trained me on experimental skills on a day-to-day basis, and shared his research ideas and thoughts with me. Secondly, I would like to thank Dr. Fabien Souris who was always willing to help and give his best suggestions. Particularly, he helped me to write a labview program to ramp up current for my measurement. A very special thank goes to Hugh Ramp who proofread this entire thesis. I would also like to thank Paul Kim, who suggested various things related to fabrication processes of my devices to me, and Callum Doolin who programmed most of the instruments I used. Finally, I would like to thank Bradley Hauer, Thomas Clark, and Clinton Potts with whom I had less overlap but who were nonetheless wonderful friends and colleagues.

I would like to thank Greg Popowich, our experienced technical staff, who always solved my equipment related problems immediately. Special thanks go to the nanofab staff at University of Alberta who trained me to fabricate the devices for this thesis. The staff of the physics machine shop were also incredibly helpful in solving many of the practical problems that arose in my experiment.

I recognize that this research would not have been possible without the financial assistance of the University of Alberta and Alberta Innovates Health Solutions, and express my gratitude to them.

Finally, I would like to thank my family, my parents Md. Abdul Khaleque and Nourjahan Begum for their endless support, unconditional love and constant encouragement. A very special thank goes to eternal love Nazia, my wife who came in Canada from eleven thousand kilometres away to accompany me. She is taking care of me and our son Rafsan, who is my main inspiration to work hard. His smiling face always helped me to erase any hard times and encouraged me to look forward. Thank you all.

Contents

Abstract ii

Acknowledgements iv

List of Tables viii

List of Figures x

1 Introduction **1**

1.1 Outline of the thesis 5

2 Theoretical Background **7**

2.1 Simple harmonic oscillation 7

2.2 Damped harmonic oscillator 8

2.3 Driven damped harmonic oscillation 9

2.4 Beam theory 12

2.5 Frequency shift in response to additional mass 17

2.6 Thermomechanical calibration of resonator motion 19

3 Fabrication of Nanostrings **25**

3.1 Material selection to fabricate nanostrings 25

3.2 Mechanical nanostring design 27

3.3 Wafer cleaning 30

3.4 Deposition of gold 31

3.5 Dicing of wafer 33

3.6 Lithography process 33
3.6.1 Deposition of photoresist layer 35
3.6.2 Patterned chips by mask aligner 37
3.6.3 Cleaning the photomask 40
3.7 Etching 40
3.7.1 Wet-etching of Au and Cr layer 41
3.7.2 Dry-etching (Reactive-ion etching) of Si_3N_4 42
3.7.3 Wet-etching the sacrificial layer of SiO_2 43

4 Measurement Techniques 46
4.1 Experimental schematic 46
4.2 Laser power attenuation 50
4.3 Vacuum chamber 51
4.3.1 Vacuum parts 51
4.3.2 Beaker of acetone 52
4.3.3 Constant current source 52
4.3.4 Thermoelectric temperature controller 52
4.4 Resonance frequency of phase-locked loop mode 53

5 Detection of Mass of Polymer 55

6 Results of Acetone Detection 78

7 Conclusions 86
7.1 Future work 88

A Frequency shift for a monolayer acetone 99

List of Tables

5.1 Dimensions of 215 μm long polymer coated nanostring resonators, which were measured using the SEM image of the device shown in Fig. 5.2. The density of nanostring materials (Si_3N_4, Cr, and Au) [34] and polymer (HPR 504 photoresist) [83, 84] were also included. From the density and volume relationship, the mass of each layer of the nanostring was calculated. 58

5.2 Dimensions of 195 μm long polymer coated nanostring resonators, which were measured using the SEM image of the device. The density of nanostring materials (Si_3N_4, Cr, and Au) [34] and polymer (HPR 504 photoresist) [83, 84] were also included. From the density and volume relationship, the mass of each layer of the nanostring was calculated. 58

5.3 Material properties of nanostring resonators and substrate. The table is taken from Ref. [34]. 58

5.4 Qualitative measurement of desorption of polymer of the 215 μm long polymer coated device using frequency shift after each current sweep, which was taken from Fig. 5.9. The total mass of the device was taken from table 5.1, which is 1251 pg and the effective mass of the device is 626 pg. 66

5.5 Qualitative measurement of desorption of polymer of the 195 μm long polymer coated device using frequency shift after each current sweep which was taken from Fig. 5.10. The total mass of the device was taken from table 5.2, which is 933 pg and the effective mass of the device is 466.5 pg. 67

5.6 Desorption of polymer for 10 minute period for different values of current. It was calculated using Eq. 2.43, where $\frac{\Delta f}{f}$, the relative resonance frequency, was taken from the Fig. 5.17 and f was the initial resonance frequency of that corresponding current. 76

List of Figures

2.1 (a) In-phase, (b) quadrature and, (c) absolute amplitude response of a driven damped harmonic oscillator as a function of driving frequency ω_d, (d) Phase response as a function of driving frequency ω_d. This graph is taken from Ref. [53]. 11

2.2 A schematic diagram of a double clamped beam of length l, thickness, t and width w. The beam displacement in the x direction. This diagram is adapted from Ref. [55]. 13

2.3 A differential element of length dz is subject to forces $F_x(z + dz)$ and $F_x(z)$, and bending moments $M_y(z + dz)$ and $M_y(z)$, which generate the displacement $U(z, t)$. This diagram is adapted from Ref. [56]. . . 14

2.4 First four bending modes ($n = 1, 2, 3$ and 4) of a doubly clamped beam seen from the side. The y-axis corresponds to the amplitude and x-axis the position where 0 and 1 indicate the clamped ends of the beam. The figure is taken from Ref. [55]. 16

3.1 Q-factor in mechanical resonators varying in size from the microscale to the nanoscale. This graph is taken from Ref. [68]. 26

3.2 (a) A designed photomask using L-edit software, (b) 5 inch $\times$ 5 inch hard mask with the same pattern as in (a). 27

3.3 Fabrication process for gold coated silicon nitride device. (a) a Si_3N_4 chip, (b) deposition of 10 nm Cr at first and then 45 nm of Au on Si_3N_4 wafer by sputtering, (c) spin coating of ethyl lactate polymer (HPR 504 photoresist), (d) patterned of photoresist by optical photolithography technique, (e) wet etching of Au at first and then Cr, (f) dry etching of Si_3N_4 by reactive-ion etching (RIE), (g) removed of HPR 504 photoresist by acetone and IPA, (h) wet etching of sacrificial SiO_2 layer by buffered oxide etch (BOE) process. 28

3.4 Fabrication process for ethyl lactate polymer (HPR 504 photoresist) coated gold nanostring. (a) a Si_3N_4 chip, (b) deposition of 10 nm Cr at first and then 45 nm of Au on Si_3N_4 wafer by sputtering, (c) spin coating of ethyl lactate polymer (HPR 504), (d) patterned of Photoresist by optical photolithography technique, (e) wet etching of Au at first and then Au, (f) dry etching of Si_3N_4 by reactive-ion etching (RIE), (g) wet etching of sacrificial SiO_2 layer by buffered oxide etch (BOE) process. 29

3.5 (a) Doug sputtering system at nanoFab in University of Alberta, (b) 4-inch diameter silicon nitride wafer before deposition, (c) the same wafer after at first deposition of 10 nm Cr and then 45 nm Au, using the sputtering system. 32

3.6 (a) Dicing saw (Disco DAD 321) in the nanoFab, and (b) a wafer is diced into 10 mm by 15 mm pieces using this dicing saw. 33

3.7 UV exposure through a patterned photomask and development of, (a) positive photoresist, (b) negative photoresist. This diagram is reproduced from Ref. [78]. 34

3.8 A beaker with HPR 504 photoresist is shown on the left. A dropper is used to pour sufficient amount of HPR 504 on the chip. Two 10 mm × 15 mm chips which are used to pattern HPR 504 photoresist. . . . 34
3.9 The variation of photoresist HPR 504 film thickness with respect to the spinner rotation speed. The data is taken from the nanoFab SOP for HPR 504. 35
3.10 Spin coating process, (a) Resist dispensing (few mL) on the chip, (b) preliminary rotation step of 500 RPM for 10 s to spread the photoresist over the whole chip, (c) final spinning step of 4000 RPM for 40 s. This diagram is reproduced from Ref. [78]. 36
3.11 Alpha step profilometre scan of HPR 504 photoresist (polymer) showing thickness (1.241μm) and average roughness. 36
3.12 (a) ABM mask aligner with Ultra-violate source, (b) The full wafer is mounted on the right big chuck and a small chip is mounted on the left small chuck. 37
3.13 Top view images of 215 μm device just after lithography process, (a) patterned photoresist on the chip, (b) zoom in image of string (pink inset), (c) 10× more zoom in image of the same device. 38
3.14 Top view of 215 μm long device after uncontrolled gold etching, (a) Etching of gold using existing solution in nanoFab, and (b) Most of the gold of a small portion of the device is etched by the existing solution. 41
3.15 Reactive-ion etching (RIE) machine in nanoFab. A snap of the parameters those are used to etch 250 nm Si_3N_4 layer. 42
3.16 A 215 μm long released gold coated silicon nitride string, (a) Top view, (b) 65° tilted view which shows the undercut of the device. 43

3.17 A 215 μm long released ethyl lactate coated gold nanostring, (a) Top view, (b) 65° tilted view which shows the undercut of the device, and (c) zoom in image of a portion of the string. 44

4.1 (a) Schematic of our experimental setup, and (b) Picture of our experimental setup. 47

4.2 Optical interferometric displacement detection in mechanical resonators. A laser beam is focused on the centre of a nanostring through an objective lens. In Fabry-Pérot interferometry, reflected light from the mechanical resonators structure is collimated through the same lens and is directed on to a photodetector. This diagram is adapted from Ref. [39]. 48

4.3 Picture of our experimental setup for injection of acetone into the vacuum chamber. 49

4.4 Left-top is the constant current source (Keithley-2401) and bottom one is thermoelectric temperature controller. Right top is the Peltier element and bottom one is the resistance temperature detector (PT-1000). The figures of Peltier element and resistance temperature detector are taken from thorlabs website. 49

4.5 (a) A home made vacuum chamber, (b) zoom in (pink inset part) of the important parts of vacuum chamber. 50

4.6 Block diagram of the phase-locked loop (PLL) comprising three main components: phase detector, loop filter, and voltage-controlled oscillator (VCO). This diagram is reproduced in Ref. [81]. 54

5.1 Fundamental mode resonance response. Power spectral density of, (a) a gold mechanical resonator (b) a polymer coated mechanical resonator. Red lines are fit of the data to the Lorentzian profile. 56

5.2 (a) SEM image of 215 μm long nanostring. It shows that the thickness of polymer layer is approximately 650 nm, (b) zoom in image of the same nanostring. 57

5.3 Schematic diagram of cross-sectional area of (a) gold coated silicon nitric nanostring, (b) polymer coated gold nanostring. 59

5.4 Resonance frequency versus current of gold nanostring. The blue line (lower current region) is the first segment of the phase-locked loop data and the deep blue (higher current region) is the second segment of the phase-locked loop data. Red line is the theoretical model of Eq. 5.3, where $f_n(0)$ is the resonance frequency (842.17 kHz) at current zero. 61

5.5 Relative resonance frequency shift versus current of gold nanostring. The blue line (lower current region) is the first segment of the phase-locked loop data and the deep blue (higher current region) is the second segment of the phase-locked loop data. Red line is the theoretical model of Eq. 5.3. 62

5.6 Resonance frequency versus current for both 215 μm long gold (blue for lower current region and deep blue for higher current region) and polymer coated (cyan for lower current region and green for higher current region) devices. Red line is the theoretical model of Eq. 5.3, where $f_n(0)$ is the resonance frequency (842.17 kHz) at current zero. The frequency difference between these two same dimension of devices is due to the additional mass of polymer. 63

5.7 Relative resonance frequency shift versus current for both 215 μm long gold (blue for lower current region and deep blue for higher current region) and polymer coated (cyan for lower current region and green for higher current region) devices. Red line is the theoretical model of Eq. 5.3. The frequency difference between these two same dimension of devices is due to the additional mass of polymer. 64

5.8 Relative shift of the resonance frequency as a function of current for three different dimensions of polymer coated devices. Blue one is 215 μm long, red one is 205 μm long, and cyan one is 195 μm long. I used two different colours for each device to indicate different segments of phase-locked loop data. 65

5.9 Resonance frequency as a function of current for different current sweeps of 215 μm long device. I used two different colours for each current sweep to indicate different segments of phase-locked loop data. The frequency shift after each current sweep is due to the desorption of polymer. 67

5.10 Resonance frequency as a function of current for different current sweeps of 195 μm long device. I used two different colours for each current sweep to indicate different segments of phase-locked loop data. The frequency shift after each current sweep is due to the desorption of polymer. 68

5.11 (a) SEM image of 215 μm long device after current sweeps. It shows that the thickness of the device after current sweeps is smaller around (406nm) than before (650 nm), (b) SEM image of the same device but different position. It shows that polymer is removed from the device due to Ohmic heating, (c) SEM image of 195 μm long device after current sweeps. (d) SEM image of the same device but different position. 69

5.12 Resonance frequency as a function of time for different values of current for gold device. It describes that the resonance frequency is fairly constant with time for all values of current. 70
5.13 Resonance frequency as a function of time for different values of current for polymer coated device. It describes that the resonance frequency remains the same for lower current, but for higher current it changes significantly. 71
5.14 Resonance frequency as a function of current for two different waiting time of current (gold nanostring). Blue one is at the starting time of current through the device and red one is after 10 minutes from the starting point. 72
5.15 Resonance frequency as a function of current for two different waiting time of current (polymer coated nanostring). Blue one is at the starting time of current through the device and red one is after 10 minutes from the starting point. 72
5.16 Derivative of the change in frequency of the nanostrings. Black circle is the gold nanostring and green circle is the polymer coated nanostring. It is shown that up to 400 μA the derivative (black circle) is constant for gold device, after that it increases a little bit. However, for polymer coated device, the derivative increase sharply, and there is a big jump from 500 μA to 600 μA. 73
5.17 Relative resonance frequency shift as a function of time for different values of current for polymer coated device. It describes that the relative resonance frequency shift remains the same (close to zero) for lower current (from 0 μA to 400 μA), but for higher current it changes significantly. 74

5.18 Resonance frequency shift as a function of time for both gold and polymer coated string at current 600 μA. It describes that the relative resonance frequency shift is linear and close to zero for gold device but for polymer coated device, it increases sharply. 75

5.19 Desorption of ethyl lactate polymer as a function of time for different values of current. It describes that there is no desorption of polymer at lower current, but for higher current it occurs significantly. 75

6.1 Resonance frequency of the fundamental mode in vacuum versus temperature as the chip is heated by Peltier element without filling the chamber with acetone vapour. Black line is theoretical model by Eq. 6.2, where $f_n(T_0)$ (1066.295 kHz) is the resonance frequency at room temperature and cyan circular dots are the experiment. 79

6.2 Resonance frequency of the fundamental mode in vacuum versus temperature for both without and with 50 mTorr acetone vapor. Both follow the same nature. The black line is the theoretical model by Eq. 6.2 in the case of without acetone, where $f_n(T_0)$ (1066.295 kHz) is the resonance frequency at room temperature. 80

6.3 Relative resonance frequency in vacuum versus current for both without and with 50 mTorr acetone vapour at $-7.5°$ C. 82

6.4 Relative resonance frequency shift in vacuum as a function of time at -7.5^o C for both without and with 50 mTorr acetone vapour. 83

7.1 Vapour pressure of acetone (log scale) based on formula $\log_{10}P_{mmHg} = 7.02474 - \frac{1161.0}{224+T}$ from [85]. The red star point on the graph indicates the temperature that we can reach using our existing cooling system, and the maximum pressure that we can measure the frequency response of nanostring. 89

7.2 Ellipsometric thickness and layer index of adsorbed acetone on graphite surface as a function of relative vapour pressure at 184 K. This graph is taken from [86]. 90

Chapter 1

Introduction

An electromechanical device is a mechanical element that is coupled to an electronic circuit, where the energy from the motion of the mechanical part is converted into electrical energy. Before the miniaturization of electromechanical devices, they were widely used in complicated systems, including electric typewriters [1], teleprinters [1], and television systems [2, 3]. In the last fifteen years, rapid progress in fabrication techniques has led to the development of electromechanical devices with dimensions in the micrometer scale, which are known as microelectromechanical systems (MEMS). MEMS technology has been inspired by the rapid development and technical advancements in the semiconductor technology. In recent years, further miniaturization of electromechanical devices has led to the nanoelectromechanical systems (NEMS) with even smaller dimensions. MEMS/NEMS devices have allowed the sensitive detection of spin [4, 5], molecular mass [6, 7, 8], quantum state [9], force [10], thermal fluctuation [11, 12, 13], and biochemical reaction [8, 14, 15, 16, 17]. Among MENS/NEMS devices nanomechanical resonators, cantilevers and doubly clamped beams have been highlighted most for applications in on-chip mass sensing due to their two important properties [17, 18, 19]. The first property is that they have small masses which allow them to detect very small masses. The second property is that they have high

mechanical quality (Q-factor) and detection capability with high signal to noise ratio.

When the nanomechanical resonator vibrates of resonance frequency, it can be used for mass sensing. For mass that is added onto a resonator, the detection sensitivity is given by the relation [6, 7, 8, 18, 19]:

$$\frac{\Delta f}{f} = -\frac{\Delta m}{2m}, \tag{1.1}$$

where f and m represent the resonance frequency and the effective mass of a device respectively, while Δf and Δm indicate the resonance frequency shift and the added mass. Assumptions for establishing Eq. 1.1 are that the amount of adsorbed mass is much smaller than the effective mass of the device and the force constant (stiffness constant) is the same before and after additional mass. From Eq. 1.1, we see that higher the frequency measurement accuracy $\frac{\Delta f}{f}$, and smaller the effective resonator mass, results in lower minimum resolvable mass Δm. This allows nanomechanical resonators to have unprecedented mass sensing resolution. Theoretical calculations for physically realizable devices indicate that nanomechanical resonator mass sensitivity below a single dalton is achievable [20]. Experimental measurements of nanomechanical mass sensing at the 1000 Da level [21] and, more recently, below the 200 Da level [22] have been demonstrated.

High-Q resonators have been fabricated using high stressed materials such as silicon nitride [23, 24], the polymer SU-8 [25], aluminum [26]. Among them, researchers have been using silicon nitride resonators for many applications such as mass sensing at the level of individual molecules [27], force sensing at the attonewton level [10, 27], and heat sensing below the yoctocalorie level [28]. These resonators behave like

strings rather than doubly clamped beam due to their high intrinsic tensile stress.

The main challenge for molecular sensing applications is to affix molecules on the surface of nanostring. Silicon nitride nanostrings have many applications, but, they are not very good candidates for molecular sensing applications [29] due to inert nature of silicon nitride. For molecular sensing applications, the nanostrings should have a surface that can affix molecules. The most common process of affixing molecules on the nanostring surface is chemical functionalization [30]. In most cases, the silicon nitride resonators are coated with gold to make them chemically functionalizable [31, 32]. The disadvantage of metallization is that it reduces the Q-factor [33], resulting in degradation of sensor performance. However, our group [34] found that the Q-factor of the fundamental frequency is not adversely affected by a relatively thick metallic layer (43 nm) on the top of silicon nitride nanostring.

Another important property of gold is that it is a good electrical conductor [35], so it is easy to flow current along the metallic gold layer of the gold coated nanostrings. Ohmic heating can be generated on the surface of the nanostring by flowing current through it, thus the temperature of the nanostrings can be varied by generating this ohmic heating on the nanostrings surface. Recently, our group [34] was able to generate the Ohmic heating by passing current through the gold nanostring device. It was shown that this local heating can be used to actuate the gold nanostring by passing alternating current (AC) along the length of the device. Very recently, S. Bose *et al.* [36] have characterized the glass transition temperature of polymers (PDLLA and PLLA) using silicon nitride microstring from the variation of resonance frequency and Q-factor as a function of temperature. I have been motivated to study the desorption of ethyl lactate polymer using a similar concept of this paper [36]; with the adaptation of tuning current instead of temperature. So, the first goal in

this study is to detect the mass of ethyl lactate polymer using gold coated nanostring with the conjunction of on-chip local heating which is generated by passing current through the gold metallic layer.

The gold coated silicon nitride and ethyl lactate polymer coated gold nanostring were fabricated using a standard optical lithography process, which is easier and cheaper than other techniques like electron-beam lithography. We established an experimental setup following the principle of optical Fabry-Pérot interferometic technique [37, 38, 39, 40] for the measurements of the motion of the nanostring. We detected the change in mass of the polymer in the presence of sufficient ohmic heating on the polymer coated nanostring, like thermogravimetric analysis.

The second aim of my study is to use the gold coated silicon nitride nanostrings to detect metabolic molecules, particularly acetone. Acetone is a colourless, volatile, flammable liquid which produced during biosynthetic processes and escapes the body through the exhaled breath of a person with certain diseases, such as diabetes and lung cancer [41, 42]. Pregnant women and children also have high level of acetone [43]. The main challenge for acetone detection is that it does not stick well to the surface of nanostrings. It is well known that there are two different process to stick the molecules on the nanostring surface which are chemisorption and physisorption. For chemisorption, which is more common, the adsorbate molecules form a direct bond with the nanostring surface [30]. Sometimes an additional layer like polymeric films [7], thiols [44], antibodies [45], enzyme [16, 46], and other chemical linker, is needed to establish a bond between the surface of the nanostring and adsorbate molecules. For physisorption, only weak physical forces (Van der waals force) hold adsorbate molecules on the nanostring surface.

Our group, including me, already studied the chemisorption of acetone on gold surface in high vacuum at room temperature. We used 3-amino-1-propanethiol chemical linker to establish a carbon-nitrogen double bond between gold layer of nanostring and acetone. We expected that when the acetone reacted with 3-amino-1-propanethiol in the gas phase, there was a carbon-nitrogen double bond formed that could be observabed as a signature in the photothermal spectroscopy. Unfortunately, we could not get any fruitful outcome from this measurement due to the absence of bonds forming between carbon and nitrogen in high vacuum. Then, we moved from chemisorption to physisorption of acetone. For physisorption of acetone, we used a thermoelectric temperature controller (TEC), that allowed us to cool down the chip of nanostrings to attach acetone vapor. The advantages of this process were that the TEC only cools down the chip of nanostrings, and did not adversely affect any other part of our experimental system. However, the physisorption alone cannot provide complete information of the particular molecule adsorbed (acetone in this case). Therefore, it must be coupled with a second technique that gives chemical specificity, such as gas chromatography [47, 48] or photothermal spectroscopy [49, 50, 51, 52]. However, we expect an on-chip Ohmic heating can determine the chemical signature of acetone by causing a sharp frequency shift at a specific temperature. The final goal of this thesis is to establish a technique that provides complete information about adsorbent molecules like acetone.

1.1 Outline of the thesis

Chapter 2 provides the theoretical background describing the calculation of the resonant frequency of doubly clamped beam in several different limits using methods of continuum mechanics. The theory described in this section is used to analyze the results in Chapter 5 and 6.

Chapter 3 describes the fabrication process of mechanical resonators. It contains the fabrication process of gold coated silicon nitride and polymer coated gold devices thoroughly.

The experimental setup for the respective studies and different measurement techniques are described in Chapter 4. It provides the measurement technique of resonance frequency versus current at above the room temperature for mass sensing of polymer.

In Chapter 5, we present the results of mass sensing of polymer. The quantitative measurements of mass are also included in this Chapter.

The results of physisorption of acetone are presented in Chapter 6.

Concluding remarks and a discussion of future plan for the exciting area of research presented in this thesis are provided in Chapter 7.

Chapter 2

Theoretical Background

This chapter presents the theoretical foundations used to analyze the mechanical behaviour of nanomechanical resonators. Nanomechanical resonators can be modelled as harmonic oscillators. First few sections in this chapter provide a brief overview of the properties of harmonic oscillators. The governing equations for the flexural vibrations of doubly-clamped beams are described using the methods of continuum mechanics, which is presented in section 2.4. The effect of additional mass of molecules on the nanostring surface is explained in section 2.7. Finally the calibration of the displacement of the mechanical resonator is explained in the last section of this chapter.

2.1 Simple harmonic oscillation

The simplest example of a resonator is a spring of mass m and spring constant k [53, 54]. Using Hooke's law, when the mass is displaced from its equilibrium position, the spring exerts a restoring force, $\vec{F} = -k\vec{x}$, where $\vec{x}$ is the displacement. The equation of motion for such a one-dimensional system can be described by the mathematical equation [54]

$$m\ddot{x}(t) + kx(t) = 0, \tag{2.1}$$

or

$$\ddot{x}(t) + \omega_o^2 x(t) = 0, \tag{2.2}$$

where $\omega_o = \sqrt{\frac{k}{m}}$ is the angular frequency of the system about the equilibrium position. The solution of Eq. 2.2 describes the motion of a simple harmonic oscillation [54],

$$x(t) = A\cos(\omega_o t + \phi), \tag{2.3}$$

where ϕ is the phase angle. Since there is no damping mechanism in the system, the oscillation continues on forever. However, in a realistic situation, the motion of a resonator is damped, where the damping term depends on the velocity of the resonator.

2.2 Damped harmonic oscillator

In real mechanical resonators, damping force is always present, which is proportional to the velocity of the mass and can be represented by the damping constant b. Therefore, the equation for damped harmonic oscillator is [53, 54]

$$m\ddot{x}(t) = -kx(t) - b\dot{x}(t). \tag{2.4}$$

We can write this equation by

$$\ddot{x}(t) + \gamma\dot{x}(t) + \omega_o^2 x(t) = 0, \tag{2.5}$$

where $\gamma = \frac{b}{m}$. The solution of Eq. 2.5 can be written as [53] $x(t) = \mathrm{Re}[x_o e^{i\omega t}]$, where x_o is the amplitude and ω is the oscillation frequency. Substituting this solution into

Eq. 2.5 gives $-\omega^2 + i\gamma\omega + \omega_o^2 = 0$ with solution,

$$\omega_\pm = i\frac{\gamma}{2} \pm \sqrt{\omega_o^2 - \frac{\gamma^2}{4}} = i\frac{\gamma}{2} \pm \omega_o\sqrt{1 - \frac{\gamma^2}{4\omega_o^2}}. \tag{2.6}$$

In the limit of small damping, the term inside the square root can be simplified by defining a new parameter

$$Q = \frac{\omega_o}{\gamma}, \tag{2.7}$$

the quality factor, which quantifies the damping in the system [53]. The displacement in terms of the Q-factor is

$$\begin{aligned} x(t) &= \mathrm{Re}[x_o e^{-\frac{\omega_o t}{2Q}} e^{\pm i\omega_o' t}] \\ &= x_o e^{-\frac{\omega_o t}{2Q}} \cos(\omega_o' t), \end{aligned} \tag{2.8}$$

where the natural frequency of the system is

$$\omega_o' = \omega_o\sqrt{1 - \frac{1}{4Q^2}}. \tag{2.9}$$

For the underdamped case ($Q \gg 1$), the system's motion can be approximated to that of a simple harmonic oscillator, $\omega_o' = \omega_o$. On the other hand, for a strongly damped system (Q$\approx$ 1), the natural frequency is lower than ω_o, and the displacement decreases rapidly within a few oscillations.

2.3 Driven damped harmonic oscillation

In general, the damped harmonic oscillator will die out after a certain period of time. Due to this reason, a driven force can be applied to the oscillator to keep continuation of the motion. Thus a more realistic oscillating system such as nanomechanical

resonator can be modelled as a driven damped harmonic oscillator [53, 54] with an equation of motion

$$m\ddot{x}(t) + m\gamma\dot{x}(t) + m\omega_o^2 x(t) = F_d \cos(\omega_d t), \tag{2.10}$$

where it assumes that the external force is sinusoidal with amplitude F_d and carrier frequency ω_d. In terms of Q-factor, Eq. 2.10 can be written as [53]

$$m\ddot{x}(t) + m\frac{\omega_o}{Q}\dot{x}(t) + m\omega_o^2 x(t) = F_d \cos(\omega_d t). \tag{2.11}$$

The solution to Eq. 2.11 is the sum of a homogenous solution, found by setting $F_d = 0$, and a particular solution, which is the force periodic with frequency ω_d.

The homogenous solution is simply the displacement of the undriven damped harmonic oscillation Eq. 2.5. Since the amplitude of transient solution is time-dependent and becomes smaller for increasing periods of oscillations, this solution can be ignored for sufficiently high Q-factor, when considering steady state solutions of Eq. 2.11. The particular solution is of the form $\mathrm{Re}[Ce^{i\omega_d t}]$, where C is the amplitude response function of the oscillation [53]

$$C = \frac{\frac{F_d}{m}}{-\omega_d^2 + i\frac{\omega_d\omega_o}{Q} + \omega_o^2}, \tag{2.12}$$

and it is a complex number which can be written as $C = C_x + iC_y$, where

$$C_x = \frac{\frac{F_d}{m}(\omega_o^2 - \omega_d^2)}{\sqrt{(\omega_o^2 - \omega_d^2)^2 + \frac{\omega_d^2\omega_o^2}{Q^2}}}, \tag{2.13}$$

and

$$C_y = \frac{\frac{F_d}{m}\frac{\omega_o\omega_d}{Q}}{\sqrt{(\omega_o^2 - \omega_d^2)^2 + \frac{\omega_d^2\omega_o^2}{Q^2}}}. \tag{2.14}$$

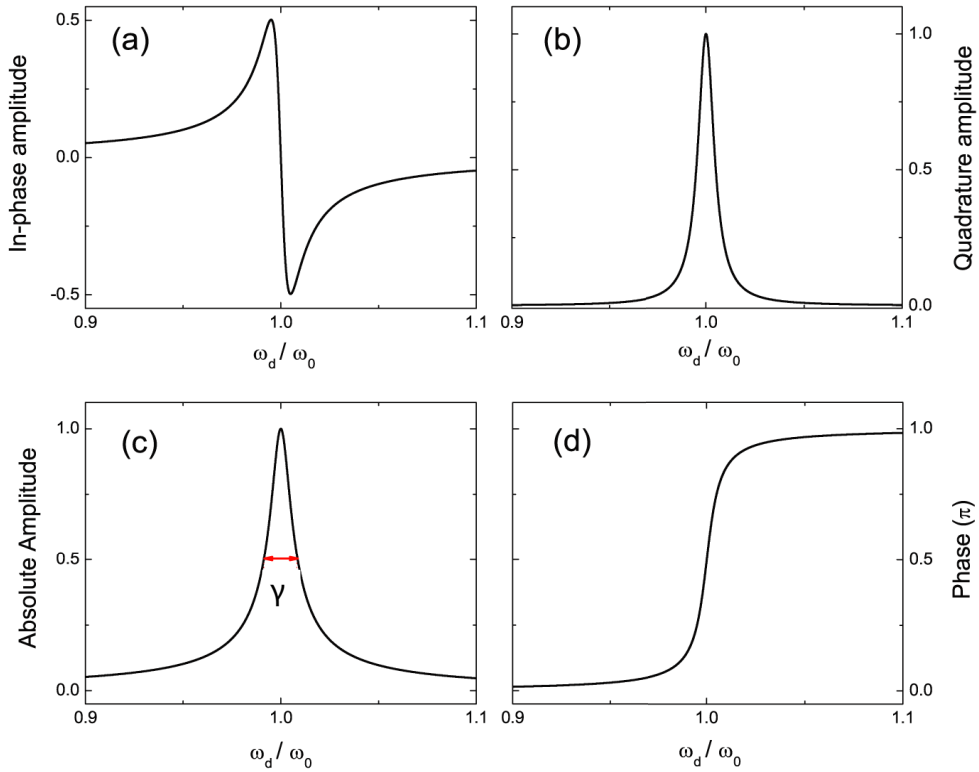

Figure 2.1: (a) In-phase, (b) quadrature and, (c) absolute amplitude response of a driven damped harmonic oscillator as a function of driving frequency ω_d, (d) Phase response as a function of driving frequency ω_d. This graph is taken from Ref. [53].

The real part C_x is known as the in-phase amplitude and the imaginary part C_y is the quadrature amplitude. The corresponding lineshapes are shown in Figs. 2.1(a) and 2.1(b).

The resonance response can also be written in the form $C = c_o e^{-i\phi}$, where, c_o and ϕ are written as [53]

$$c_o = \frac{\frac{F_d}{m}}{\sqrt{(\omega_o^2 - \omega_d^2)^2 + \frac{\omega_d^2 \omega_o^2}{Q^2}}}, \tag{2.15}$$

and

$$\phi = \tan^{-1}[\frac{\omega_d \omega_o}{Q(\omega_o^2 - \omega_d^2)}] \qquad \omega_d < \omega_o$$

$$= \pi + \tan^{-1}[\frac{\omega_d \omega_o}{Q(\omega_o^2 - \omega_d^2)}] \qquad \omega_d > \omega_o. \tag{2.16}$$

Figure 2.1(d) describes the phase response as a function of driving frequency ω_d. Initially, for $\omega_d < \omega_o$, the resonator response is in phase with the periodic driving force. However, near the natural resonance frequency, the resonator starts to increasingly lag behind the driving force. On resonance, where $\omega_d = \omega_o$, the phase difference between the driving force and the oscillator motion is $\frac{\pi}{2}$ radians. Beyond the natural resonance frequency, $\omega_d > \omega_o$, the phase difference becomes π radians. The Q-factor of a harmonic oscillator can be determined easily from the resonance peak in the amplitude response by dividing the natural resonance frequency ω_o with the full-width half-max γ of the resonance peak ($Q = \frac{\omega_o}{\gamma}$) which is shown in Fig. 2.1(c).

2.4 Beam theory

The principal goal of this section is to study basic beam theory and modes of operations of a rectangular structure of beam. While many beam theories exist, the simplest and most useful theory is Euler-Bernoulli beam theory. For discussing Euler-Bernoulli beam theory, I have followed mostly in Ref. [55].

Let us consider a beam of thickness t, length l, and width w, aligned along z-axis as shown in Fig 2.2. Suppose, dz is an elemental section of the beam as shown in Fig. 2.3. The internal shear force applied upward on the left hand side of the section and the internal shear force applied downward on the right hand side of the section are $F_x(z)$ and $F_x(z + dz)$, respectively. The bending moments applied on the left hand side and the right hand side of the section are $M_y(z)$ and $M_y(z + dz)$, respectively. Suppose, $f(z)$ is the loading force per unit length of the beam.

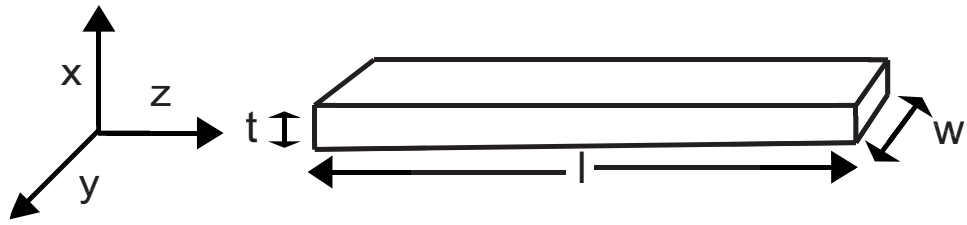

Figure 2.2: A schematic diagram of a double clamped beam of length l, thickness, t and width w. The beam displacement in the x direction. This diagram is adapted from Ref. [55].

Since $\rho A dz \frac{\partial^2 U(z,t)}{\partial t^2}$ is the inertia force acting on the elemental section of the beam, the balancing forces in x direction can be written using Fig. 2.3 as

$$F_x(z+dz) - F_x(z) + f(z)dz = \rho A dz \frac{\partial^2 U(z,t)}{\partial t^2}, \tag{2.17}$$

where $U(z,t)$ is the transverse displacement due to forces along x-axis and moments along y-axis, ρ is the density and A is the cross-sectional area of the beam. The moment equation about the y axis using Fig. 2.3 can be written as

$$M_y(z+dz) - F_x(z+dz)dz + f(z)dz\frac{dz}{2} - M_y(z) = 0. \tag{2.18}$$

Using Taylor series for forces and toques about the z point and keeping only first order terms in dz, then Eqs. (2.17) and (2.18) can be written as

$$-\frac{\partial F_x(z)}{\partial z} + f(z) = \rho A \frac{\partial^2 U(z,t)}{\partial t^2}, \tag{2.19}$$

and

$$F_x(z) = \frac{\partial M_y}{\partial z}. \tag{2.20}$$

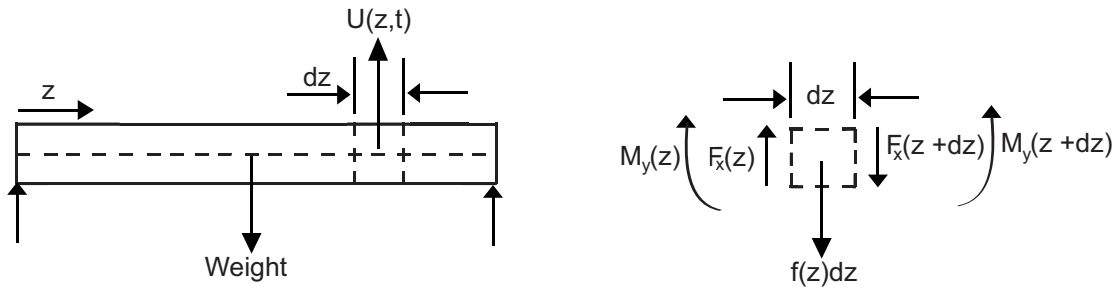

Figure 2.3: A differential element of length dz is subject to forces $F_x(z+dz)$ and $F_x(z)$, and bending moments $M_y(z+dz)$ and $M_y(z)$, which generate the displacement $U(z,t)$. This diagram is adapted from Ref. [56].

When the deflection is small compared to its length, the moment-curvature relationship for a homogenous beam is given by

$$M_y = EI_y \frac{\partial^2 U(z,t)}{\partial z^2}, \tag{2.21}$$

where E is the Young's modulus of the beam and I_y is the cross-sectional moment of inertia. Combining Eqs. (2.19) and (2.20) and using (2.21), it can be written as

$$\frac{\partial^2}{\partial z^2}\left(EI_y \frac{\partial^2 U(z,t)}{\partial z^2}\right) + \rho A \frac{\partial^2 U(z,t)}{\partial t^2} = f(z). \tag{2.22}$$

If the beam's bending moment I_y is constant along the length of the beam, then Eq. (2.22) may be written as

$$EI_y \frac{\partial^4 U(z,t)}{\partial z^4} + \rho A \frac{\partial^2 U(z,t)}{\partial t^2} = f(z). \tag{2.23}$$

For free vibration, $f(z) = 0$, and the equation of motion becomes

$$EI_y \frac{\partial^4 U(z,t)}{\partial z^4} + \rho A \frac{\partial^2 U(z,t)}{\partial t^2} = 0. \tag{2.24}$$

More generally, if we assume a harmonic time dependence for the displacement, $U(z,t) = U(z)e^{i\omega t}$, the spatial dependence must satisfy the differential equation

$$\frac{\partial^4 U(z)}{\partial z^4} = \frac{\rho A}{EI_y}\omega^2 U(z). \tag{2.25}$$

Defining $\beta = \left(\frac{\rho A}{EI_y}\right)^{\frac{1}{4}} \omega^{\frac{1}{2}}$ and assuming a spatial dependence of the form $U(z) = e^{\kappa z}$, the solutions are $\kappa = \pm\beta$, $\pm i\beta$. Hence the general solution has the form

$$U(z) = Ae^{i\beta z} + Be^{-i\beta z} + Ce^{\beta z} + De^{-\beta z}. \tag{2.26}$$

In terms of real function, the solution becomes,

$$U(z) = a\cos(\beta z) + b\sin(\beta z) + c\cosh(\beta z) + d\sinh(\beta z). \tag{2.27}$$

For a beam clamped at both ends, the displacements $U(0)$ and $U(l)$ are zero, as are the slopes $\frac{dU}{dz(0)}$ and $\frac{dU}{dz(l)}$. Using general solution (2.27), these boundary conditions imply that, $a = -c$ and $b = -d$, and the allowed values of β are from a discrete set, satisfying

$$\cos(\beta_n l)\cosh(\beta_n l) - 1 = 0. \tag{2.28}$$

The zeroes of this function can be found numerically with $\beta_n l = 0$, 4.730004, 7.8532, 10.9956, 14.1372, $\cdots\cdots$. The solution $\beta = 0$ is trivial that is discarded. The displacement is then given by

$$U_n = a_n(\cos(\beta_n z) - \cosh(\beta_n z)) + b_n(\sin(\beta_n z) - \sinh(\beta_n z)). \tag{2.29}$$

The relative amplitudes for the two terms for the first modes are $\frac{a_n}{b_n} = 1.0178, 0.99923,$ $1.0006, \cdots\cdots$, found from the boundary conditions. The corresponding frequencies

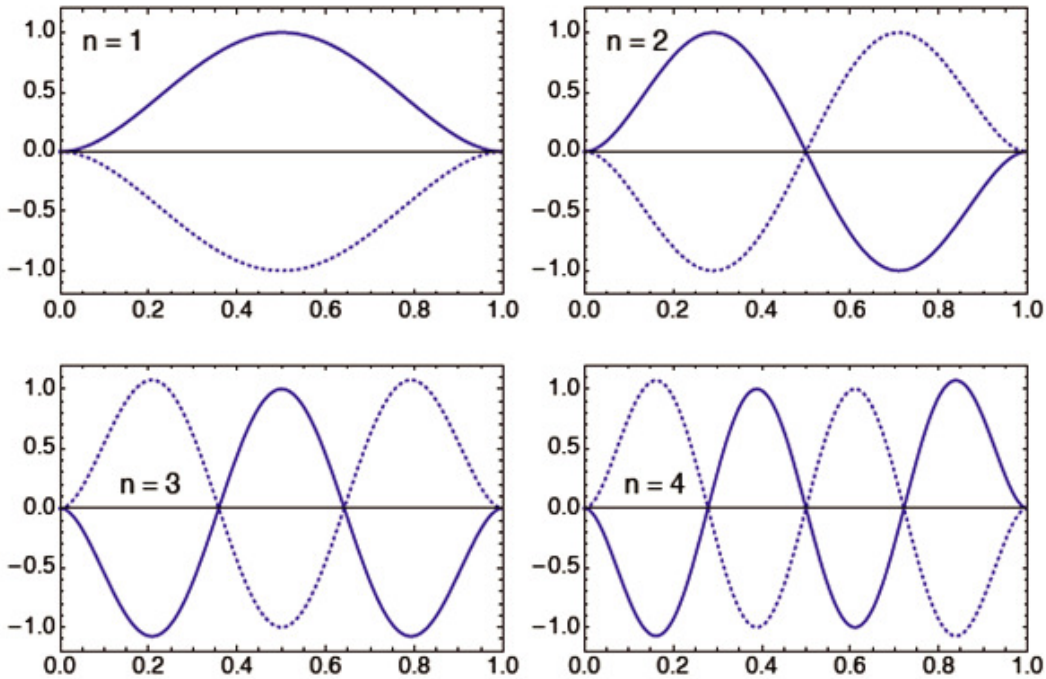

Figure 2.4: First four bending modes ($n = 1, 2, 3$ and 4) of a doubly clamped beam seen from the side. The y-axis corresponds to the amplitude and x- axis the position where 0 and 1 indicate the clamped ends of the beam. The figure is taken from Ref. [55].

are given by

$$\omega_n = \sqrt{\frac{EI_y}{\rho A}}\beta_n^2, \tag{2.30}$$

or

$$f_n = \frac{1}{2\pi}\sqrt{\frac{EI_y}{\rho A}}\beta_n^2. \tag{2.31}$$

The spatial dependence for the lowest four solutions (n = 1 to 4) for the doubly-clamped flexural beam are shown in Fig. 2.4. Identifying the beam-dynamics of an individual resonance mode with that of a harmonic oscillator, the eigenfrequency can generally be expressed as [57]

$$f_n = \frac{1}{2\pi}\sqrt{\frac{k}{m_{\text{eff}}}}, \tag{2.32}$$

where k is the spring constant and m_{eff} is the effective mass of the beam.

The effective mass of a resonating double clamped beam can be calculated through

equating the kinetic spring energy of the resonator to the kinetic energy along the beam [58]

$$\frac{1}{2}m_{\text{eff}}\omega_n^2 U_n^2(l) = \frac{1}{2}\frac{m}{l}\omega_n^2 \int_0^l U_n(z)^2 dz, \tag{2.33}$$

where m is the true mass of the beam given by $m = \rho wtl$. Applying Eq. 2.27 into Eq. 2.33, the effective mass is found to be a half of the mass of total double clamped beam, independent of the mode number

$$m_{\text{eff}} = \frac{m}{2}. \tag{2.34}$$

2.5 Frequency shift in response to additional mass

The change in the effective mass of a beam due to mass loading will lead to a change in its resonant frequency, as described in this section. In the following analysis, it is assumed that the analyte mass is much smaller than the beam mass and the addition of the analyte does not affect other beam properties such as the mode shape or spring constant of the beam. The following discussion follows closely from Ref. [59].

Consider a nanostring of length l, width w, and thickness t, with the long axis along $\hat{z}$. The total mechanical energy (kinetic and potential) of a string vibrating in one of its normal modes [59]

$$E_n = \int_0^l \mu(z)\omega_n^2 U_n^2(z) dz, \tag{2.35}$$

where z measures the distance along the string, ω_n and $U_n(z)$ are the angular frequency and displacement profile of mode n, and $\mu(x)$ is the mass per unit length at position x. A small mass perturbation, arising from deposition of a distribution of molecules on the surface of the string, leads to a modified mass distribution $\mu(z) \to \mu(z) + \Delta\mu(z)$ and a corresponding frequency shift $\omega_n \to \omega_n + \Delta\omega_n$. The total

energy after deposition of molecules of mass Δm is

$$\begin{aligned} E'_n &= \int_0^l (\mu(z) + \Delta\mu(z))(\omega_n + \Delta\omega_n)^2 U_n^2(z) dz \\ &= \int_0^l (\mu(z) + \Delta\mu(z))(\omega_n^2 + \Delta\omega_n^2 + 2\omega_n \Delta\omega_n) U_n^2(z) dz. \end{aligned} \tag{2.36}$$

Keeping up to the first order perturbation, we find

$$E' = \int_0^l [\mu(z)\omega_n^2 U_n^2(z) + \Delta\mu(z)\omega_n^2 U_n^2(z) + 2\mu(z)\omega_n \Delta\omega U_n^2(z)] dz. \tag{2.37}$$

Energy conservation law says that the variation of $\Delta\mu(z)$ and $\Delta\omega_n$ leave the energy stationary *i.e.*, $dE = 0$; hence

$$0 = \int_0^l [\Delta\mu(z)\omega_n^2 U_n^2(z) + 2\mu(z)\omega_n \Delta\omega U_n^2(z)] dz, \tag{2.38}$$

which implies

$$-\frac{2\Delta\omega_n}{\omega_n} = \frac{\int_0^l \Delta\mu(z) U_n^2(z) dz}{\int_0^l \mu(z) U_n^2(z) dz}. \tag{2.39}$$

If the unperturbed string has a uniform mass distribution $\mu(z) = \frac{m}{l}$, then

$$-\frac{2\Delta\omega_n}{\omega_n} = \frac{l}{m} \frac{\int_0^l \Delta\mu(z) U_n^2(z) dz}{\int_0^l U_n^2(z) dz}. \tag{2.40}$$

For a high-tension string, the mode shape is a sinusoid, $U_n(z) = \sqrt{\frac{2}{l}} sin(\frac{n\pi z}{l})$, therefore

$$-\frac{2\Delta\omega_n}{\omega_n} = \frac{2}{m} \int_0^l \Delta\mu(z) sin^2(\frac{n\pi z}{l}) dz. \tag{2.41}$$

If the mass is distributed uniformly, then $\Delta\mu = \frac{\Delta m}{l}$. Putting this value in Eq. 2.39

$$-\frac{\Delta\omega_n}{\omega_n} = \frac{\Delta m}{2m}. \tag{2.42}$$

In terms of resonance frequency, $\omega_n = 2\pi f_n$ and frequency shift, $\Delta\omega_n = 2\pi\Delta f_n$ due to the mass of landing molecules, Eq. 2.42 can be written as

$$-\frac{\Delta f_n}{f_n} = \frac{\Delta m}{2m}. \tag{2.43}$$

From Eq. 2.43, we see that a higher the frequency measurement accuracy $\frac{\Delta f_n}{f_n}$ and smaller the effective resonator mass m, results in a lower minimum resolvable mass Δm.

2.6 Thermomechanical calibration of resonator motion

When incoherent thermal forces are applied to a mechanical resonators, the measurement of its motion can be calibrated to give the absolute displacement. This calibration is important for both sensing applications and fundamental tests of quantum mechanics. The non-invasive and precise approach for thermomechanical calibration is followed from the paper by Hauer *et al* [60].

Suppose the position of a mechanical resonator as a function of time is denoted by $z(t)$. Then the autocorrelation function $R_{zz}(t)$ describes how the signal $z(t)$ is related to itself at a later time $t + t'$ [61]

$$R_{zz}(t) = \lim_{\tau_m \to \infty} \frac{1}{\tau_m} \int_{-\tau_m}^{\tau_m} dt' z(t') z(t + t'). \tag{2.44}$$

The two-sided power spectral density (PSD) of $z(t)$, $P_{zz}(\omega)$ is defined as the Fourier transform of $R_{zz}(t)$ [61]

$$P_{zz}(\omega) = \int_{-\infty}^{\infty} dt R_{zz}(t) e^{i\omega t}. \tag{2.45}$$

Similarly, the autocorrelation function can be produced by performing the inverse Fourier transform

$$R_{zz}(t) = \frac{1}{2\pi}\int_{-\infty}^{\infty} d\omega P_{zz}(\omega)e^{-i\omega t}, \tag{2.46}$$

where $P_{zz}(\omega)$ is a function, defined over all positive and negative frequencies, which will be proportional to the total energy in the signal $z(t)$, when integrated over the entire frequency range. In the most experiments, negative frequency are not physical, so we define the single sided PSD $S_{zz}(\omega)$ over positive frequencies such that $\int_{-\infty}^{\infty} d\omega P_{zz}(\omega) = \int_0^{\infty} d\omega S_{zz}(\omega)$. Since any physically meaningful classical $P_{zz}(\omega)$ is an even function [62], $S_{zz}(\omega) = 2P_{zz}(\omega)$ in positive frequency domain.

We can model each of the resonator's modes as a damped harmonic oscillator driven only by incoherent thermal forces $F(t)$. Then the equation of motion for the position of the resonator $z(t)$ is

$$m_{\text{eff}}\ddot{z}(t) + m_{\text{eff}}\gamma\dot{z}(t) + m_{\text{eff}}\omega_o^2 z(t) = F(t), \tag{2.47}$$

where γ is the linear damping rate and ω_o is the angular frequency of the mechanical mode. The effective mass, m_{eff}, is mode-dependent and accounts for the extended nature of the mechanical resonator. It is given by [60]

$$m_{\text{eff}} = \int dV \rho(\vec{r})|\vec{z}(\vec{r})|^2, \tag{2.48}$$

where ρ is the density of the material and $\vec{z}(\vec{r})$ is the displacement of the resonator at each point $\vec{r}$ in space, normalized such that the maximum of $|\vec{z}(\vec{r})|$ has unit magnitude. We can solve Eq. 2.47 in the frequency domain by taking its Fourier transform. To do so, we define a function $h(t)$ as

$$H(\omega) = \int_0^{\infty} dt e^{i\omega t} h(t). \tag{2.49}$$

So, Eq. 2.49 gives using Eq. 2.47 as

$$X(\omega)\left[-\omega^2 + i\omega\gamma + \gamma^2\right] = \frac{F(\omega)}{m_{\text{eff}}}, \tag{2.50}$$

where $X(\omega)$ and $F(\omega)$ are the Fourier transforms of the position $z(t)$ and thermal force $F(t)$, respectively. The single-sided PSD, $S_{zz}(\omega)$ of the resonator's motion can be related to $X(\omega)$ [60]

$$S_{zz}(\omega) = \lim_{\tau_m \to \infty} \frac{1}{\tau_m} |X(\omega)|^2. \tag{2.51}$$

We can write Eq. 2.50 in terms of the PSDs of the mechanical motion and the thermal forces. Note that the thermal forces described by $F(t)$ are incoherent and therefore across the frequency range of interest, we can take $S_{FF}(\omega) = \lim_{\tau_m \to \infty} \frac{1}{\tau_m} |F(\omega)|^2 = S_{FF}^{\text{th}}$ to be constant and

$$S_{zz}(\omega) = |\chi(\omega)|^2 S_{FF}^{\text{th}}. \tag{2.52}$$

Here

$$\chi(\omega) = \frac{1}{m_{\text{eff}}\left[\omega_o^2 - \omega^2 - i\omega\gamma\right]}, \tag{2.53}$$

is the mechanical susceptibility, which relates $S_{zz}(\omega)$ to the PSD of the applied force $S_{FF}(\omega)$.

The constant S_{FF}^{th} can be determined from the equipartition theorem, which states that every degree of freedom that contributes a quadratic term to the total energy of a system has an energy of $\frac{k_B T}{2}$ [63]

$$\frac{1}{2} m_{\text{eff}} < z^2(t) > \Omega^2 = \frac{k_B T}{2}, \tag{2.54}$$

where T is the temperature of the mechanical mode. The root-mean-squared amplitude of the position, z_o is defined by

$$z_o^2 =< z^2(t) >= \frac{k_B T}{m_{\text{eff}}\omega_o^2}. \tag{2.55}$$

We can calculate $< z^2(t) >$ using Eq. 2.44 with $t = 0$

$$< z^2(t) >= R_{zz}(0) = \lim_{\tau_m \to \infty} \frac{1}{\tau_m} \int_0^{\tau_m} dt' \left[z(t')\right]^2, \tag{2.56}$$

as long as the duration of the measurement τ is taken to be much longer than the period of oscillation of the mechanical mode ($2\pi\omega^{-1}$). From Eq. 2.45 we see that we can recover the autocorrelation function $R_{xx}(t)$ by taking the inverse Fourier transform of $P_{zz}(\omega)$ (or equivalently, of $S_{zz}(\omega)$) over the appropriate domain. From here, we find that

$$< z^2(t) >= R_{zz}(0) = \int_0^\infty d\omega S_{zz}(\omega). \tag{2.57}$$

Integrating Eq. 2.52 and substituting the result into Eq. 2.57, we find [60]

$$< z^2(t) >= \frac{S_{FF}^{\text{th}} Q_m}{4\Omega^3 m_{\text{eff}}^2}. \tag{2.58}$$

We already have introduced the mechanical quality factor in Eq. 2.7, $Q = \frac{\omega_o}{\gamma}$. Finally, equating Eqs. 2.55 and 2.58, we have

$$S_{FF}^{\text{th}} = \frac{4k_B T m_{\text{eff}}\omega_o}{Q}, \tag{2.59}$$

and

$$S_{zz}(\omega) = \frac{4k_B T\omega_o}{m_{\text{eff}} Q\left[(\omega_o^2 - \omega^2)^2 + (\frac{\omega_o\omega}{Q})^2\right]}. \tag{2.60}$$

However, since the frequency we read off our instrument is given in terms of natural frequency, f, and not an angular frequency, so it is convenient to express S_{zz} in terms

of f. This is done by taking $\omega = 2\pi f$ and $\omega_o = 2\pi f_o$ (where f_o is the resonance frequency)

$$S_{zz}(f) = \frac{k_B T f_o}{2\pi^3 m_{\text{eff}} Q \left[(f_o^2 - f^2)^2 + (\frac{f_o f}{Q})^2 \right]}. \tag{2.61}$$

Eqs. 2.60 and 2.60 provide the power spectrum for the thermal noise of our resonator. However, there are also a number of other sources of noise to be present in our detection system, such as detector dark current and optical short noise [64]. These signals combine with the thermal noise of the resonator to produce the power spectrum read out for the undriven device S_{VV}^{w}. Therefore, we can write [60],

$$S_{vv}(f) = S_{VV}^{w} + \alpha S_{zz}(f) \tag{2.62}$$

where, S_{vv} is the noise of the detection apparatus and α is a detection dependent scaling factor, which describes how the motion of the resonator $z(t)$ is transducer into the voltage signal.

The experimental PSD can be fitted with Eq. 2.62 near a thermal resonance using S_{vv}, $A = \frac{\alpha k_B T}{2\pi^3 m_{\text{eff}}}$, f_o, and Q as a fit parameters. If we know the temperature and effective mass of the resonator, we can determine α. Once α has been determined, it can be used to convert the experimental PSD from units V^2/Hz to m^2/Hz. The resonators displacement spectrum is then determined from the square root of experimental PDS in unit of m/$\sqrt{\text{Hz}}$ [65].

In this chapter, we have described the principal equations which describe the flexural motion of nanomechanical resonators in the linear response (harmonic) regime. The natural frequencies of the resonators can be described using methods of continuum mechanics. An equation has been explained to detect mass of the adsorbent molecules from the frequency shift based on the assumptions that the mass of the adsorbent molecules is small compared to the mass of the resonators and the spring constant is the same before and after landing molecules. Finally, the thermomechanical cal-

ibration of motion of the resonator has been demonstrated to measure the actual displacements of the resonators.

Chapter 3

Fabrication of Nanostrings

Fabrication of nanostring resonators is the most challenging part of the sensing applications. It takes place in a particular environment called clean room, where particle density, temperature and humidity are controlled. In fact, if dust particles that have dimensions comparable with microstructure of device are capable of destroying the devices. More over, in order to obtain robust and repeatable processes, temperature and humidity must have always the same value with very low fluctuations. The University of Alberta has wonderful clean room facilities, which are used to fabricate the devices for this study. There are many techniques to fabricate nanostring resonators. Here, I have used a standard optical lithography process, which is easier and cheaper than other technique like electron-beam lithography. In this project, I have fabricated two types of devices: gold coated silicon nitride and polymer coated gold devices. The details of the fabrication process of devices are discussed in this Chapter.

3.1 Material selection to fabricate nanostrings

At first, we should select right materials for the device. It is always challenging to select right materials for fabrication of the device. People have been using different materials such as Platinum [66], Nickel [67], Aluminium [26], Gold [30, 31, 32, 34],

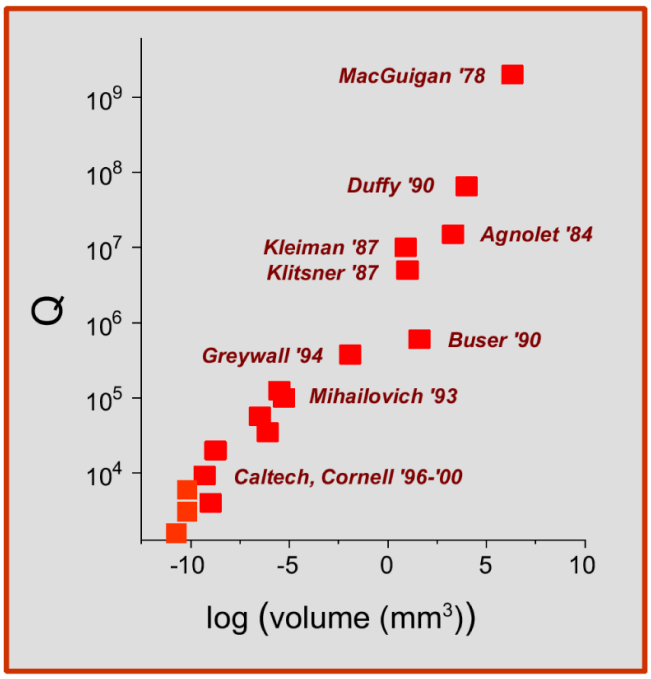

Figure 3.1: Q-factor in mechanical resonators varying in size from the microscale to the nanoscale. This graph is taken from Ref. [68].

Silicon based materials [23, 24], and some others [25] for fabrication of the device depending on their applications. For dynamic mode dependent applications, such as mass detection [6, 8], viscosity determination [69], mass density and mechanical properties of materials determination [70], silicon based materials are generally preferred for their high Young's modulus to obtain high resonance frequency. On the other hand, for static mode based applications, such as in chemical sensing [8, 71], temperature sensing [11, 13], in detection of biomarkers [14, 15] or specific DNA sequences [72] and material characterization [73, 74], polymer based materials are preferred because of their lower Young's modulus to achieve larger bending. In this project, our goal is to generate ohmic heat on the surface of the device by passing current through it. Based on this goal, we have selected gold for fabrication of our device due to its high electrical conductivity [35]. The additional advantage of using gold materials is that it is also chemically functionalizable [31, 32]. We have selected Si_3N_4 as a base material for the device due to its extremely high tensile stress

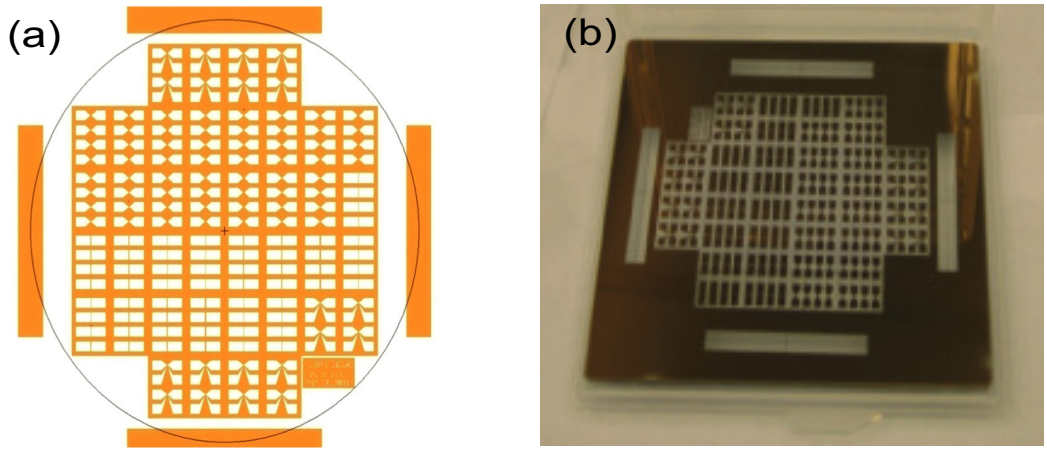

Figure 3.2: (a) A designed photomask using L-edit software, (b) 5 inch × 5 inch hard mask with the same pattern as in (a).

(σ = 0.8GPa) [23, 75, 76]. In addition, chromium is used between gold and Si_3N_4 layers to make better adhesion between them [30, 34].

3.2 Mechanical nanostring design

Nanomechanical resonators have been studied for applications in on chip mass sensing for many years due to two important reasons [17, 18, 19]. The first reason is that they have very small masses which allow them to detect very small masses. The second reason follows from their high mechanical quality factors (Q-factor), which allows for a high signal to noise ratio. To design the nanomechanical resonators, we need to select right volume of them. This is because, the Q-factor strongly depends on the volume of the device, as demonstrated in Fig. 3.1 [68]. It shows that Q-factor deceases with volume of the device, which is contrary to what is popularly believed. For my study, I have chosen the volume of device around 10^{-4}mm^3 which corresponds to Q-factor of 10^4. For getting exact volume of the device, we use a hard optical photomask during optical lithography process. A transparent substrate with a thin, opaque patterned layer is used to make a photomask. A transparent soda lime glass covered with a thin layer of chromium (opaque to UV-light) is used as a substrate

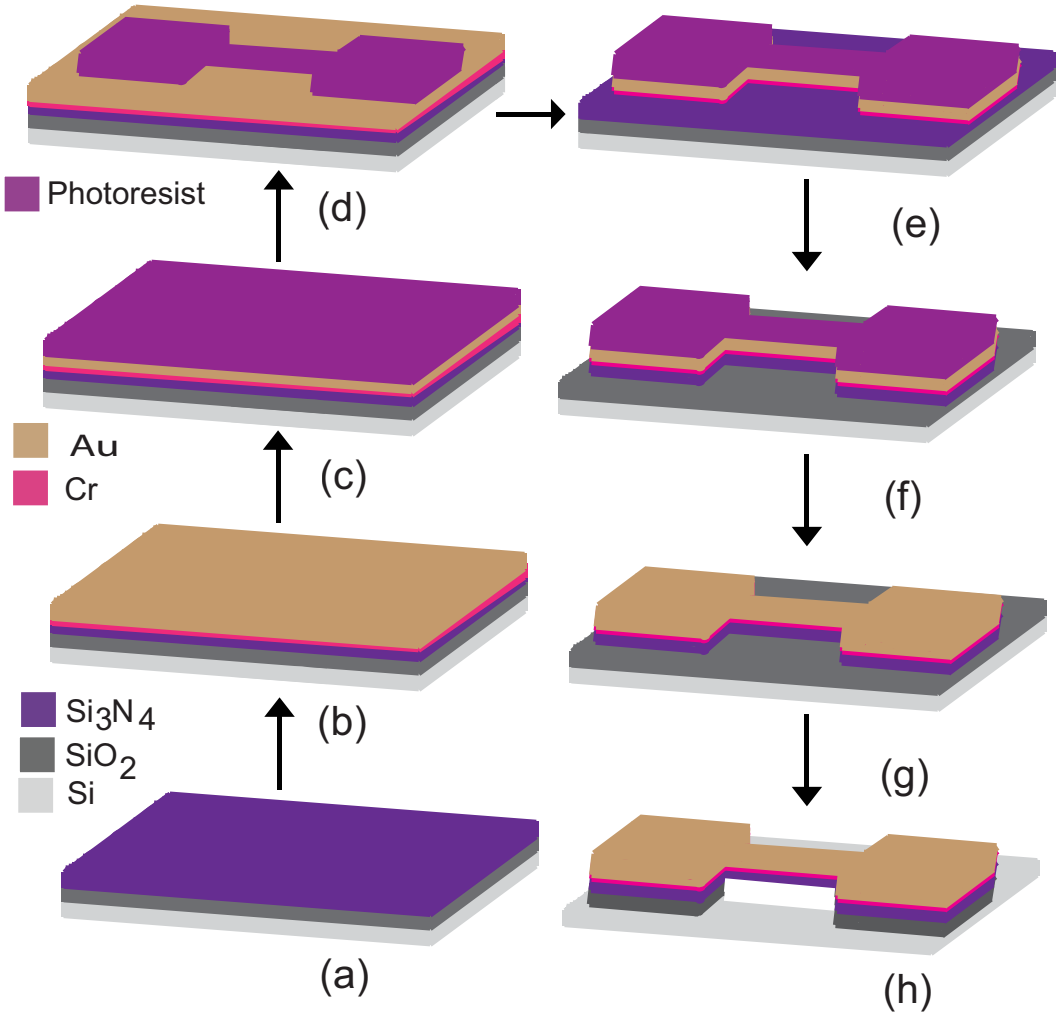

Figure 3.3: Fabrication process for gold coated silicon nitride device. (a) a Si_3N_4 chip, (b) deposition of 10 nm Cr at first and then 45 nm of Au on Si_3N_4 wafer by sputtering, (c) spin coating of ethyl lactate polymer (HPR 504 photoresist), (d) patterned of photoresist by optical photolithography technique, (e) wet etching of Au at first and then Cr, (f) dry etching of Si_3N_4 by reactive-ion etching (RIE), (g) removed of HPR 504 photoresist by acetone and IPA, (h) wet etching of sacrificial SiO_2 layer by buffered oxide etch (BOE) process.

to make a hard mask. We use pattern generator software, like L-edit, to design our mask. I have used a photomask for my device fabrication, which is designed by L-edit software as shown in Fig. 3.2(a). Many devices of different geometries and dimensions can be patterned into a single mask. A 5-inch by 5-inch patterned hard mask, which can be used for optical lithography is shown in Fig. 3.2(b).

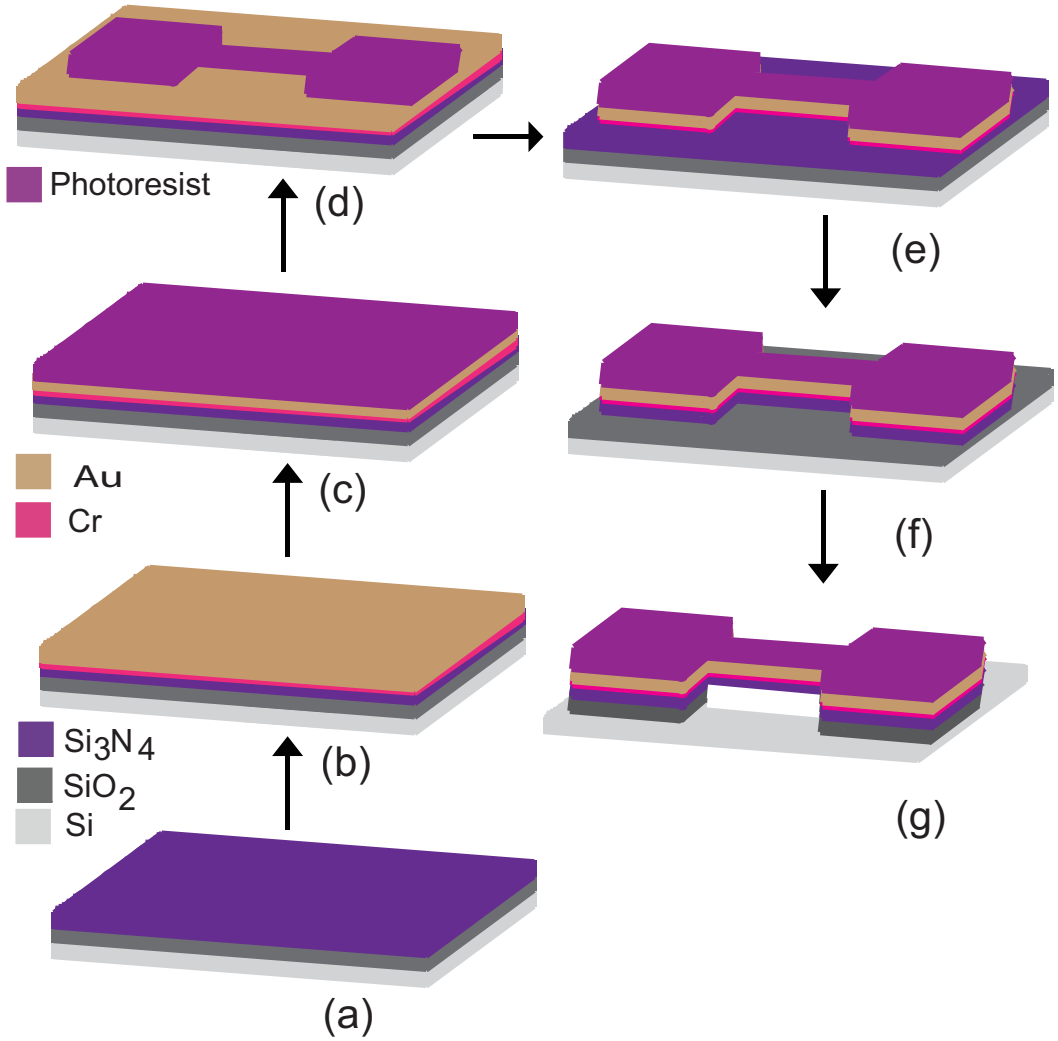

Figure 3.4: Fabrication process for ethyl lactate polymer (HPR 504 photoresist) coated gold nanostring. (a) a Si_3N_4 chip, (b) deposition of 10 nm Cr at first and then 45 nm of Au on Si_3N_4 wafer by sputtering, (c) spin coating of ethyl lactate polymer (HPR 504), (d) patterned of Photoresist by optical photolithography technique, (e) wet etching of Au at first and then Au, (f) dry etching of Si_3N_4 by reactive-ion etching (RIE), (g) wet etching of sacrificial SiO_2 layer by buffered oxide etch (BOE) process.

I have already mentioned earlier in this chapter that my goal is to fabricate two types of devices, the first one is gold coated silicon nitride devices and the other one is polymer coated gold devices. Ethyl lactate, also known as HPR 504 photo resist is used here as a polymer. So, the second type of device means it is HPR 504 photoresist coated gold devices. The overall process flow for both gold coated silicon nitride device and polymer coated gold devices are presented in Fig. 3.3 and Fig. 3.4, respectively. Note that, HPR 504 photoresist is deposited on the gold surface at the beginning of the optical lithography process for transferring the pattern of the devices from the photomask to the chip. There are two main differences between the fabrication of gold and polymer coated gold devices. For fabrication of polymer (HPR 504 photoresist) coated gold devices, HPR 504 photoresist is kept on the chip for whole fabrication process. However, it is shown in the process flow for gold coated silicon nitride device that photoresist has been removed from the chip before buffered oxide etch (BOE) process (step (h) $\rightarrow$ (g)). The another difference is that, after BOE process, we have released the gold devices by either a solvent method or a critical point drier to avoid the striction of the devices. For polymer coated devices, we have avoided both of these methods because the ingredients of these methods also etch the HPR 504 photoresist. All of the fabrication steps are processed carefully at the Nanofab cleanroom to properly handle hazardous chemicals namely piranha, and hydrofluoric acid (HF) solutions.

3.3 Wafer cleaning

We start with a 4-inch diameter wafer with layers of 250 nm high stress silicon nitride (Si_3N_4) on a 2μm silicon dioxide (SiO_2) sacrificial layer on 0.5 mm silicon (Si) substrate wafer, which is shown in 3.5(b) for fabrication of the devices. This wafer needs to be cleaned before deposition of Cr and Au metals as the nano-devices are very

sensitive to unwanted particles, metals, organics, native oxides, commonly known as contaminations. The goal of wafer cleaning is to remove contaminants without damaging the wafer surface. There are different techniques to clean wafer. The Piranha is the cheapest method for removing such these contaminants from the wafer surface. It is a mixture of Sulphuric Acid (H_2SO_4) and Hydrogen peroxide (H_2O_2) with the ratio of 3 : 1, that produces an exothermic solution near 120°C and actively strips any organic material and many metals [77].

Therefore, the piranha wet-deck is specially isolated from other wet-benches to prevent any organic or other chemicals from mixing with this aggressive piranha solution. Chemical gear including protective apron, latex gloves, and face shields must be worn always during the process. For a 4-inch diameter silicon nitride wafer, a mixture of 300 mL of sulphuric acid and 100 mL of hydrogen peroxide was used for a 15-minutes cleaning cycle. After completion of cleaning, the wafer was thoroughly rinsed with distilled water and dried with a nitrogen-gun followed by a dehydration cycle on a hotplate 110°C for 10 minutes.

3.4 Deposition of gold

After cleaning the wafer, we need to deposit metals of Cr and Au immediately to get high quality surface and avoid further contaminations. There are several issues, such as quality of the thin film, uniformity of the film, processing temperature and film stress, related to thin film deposition, which determine the choice of a deposition process. Considering these issues, I have used sputtering system (Doug) as shown in Fig. 3.5(a) for deposition of Cr and Au which is available in nanoFab at University of Alberta. In the sputtering system, a plasma is struck in an inert gas such as Ar, using rf high-voltage electric fields. Ions from the plasma are accelerated by static electric fields, generated by using a blocking capacitor in rf sputtering. The high-energy ions

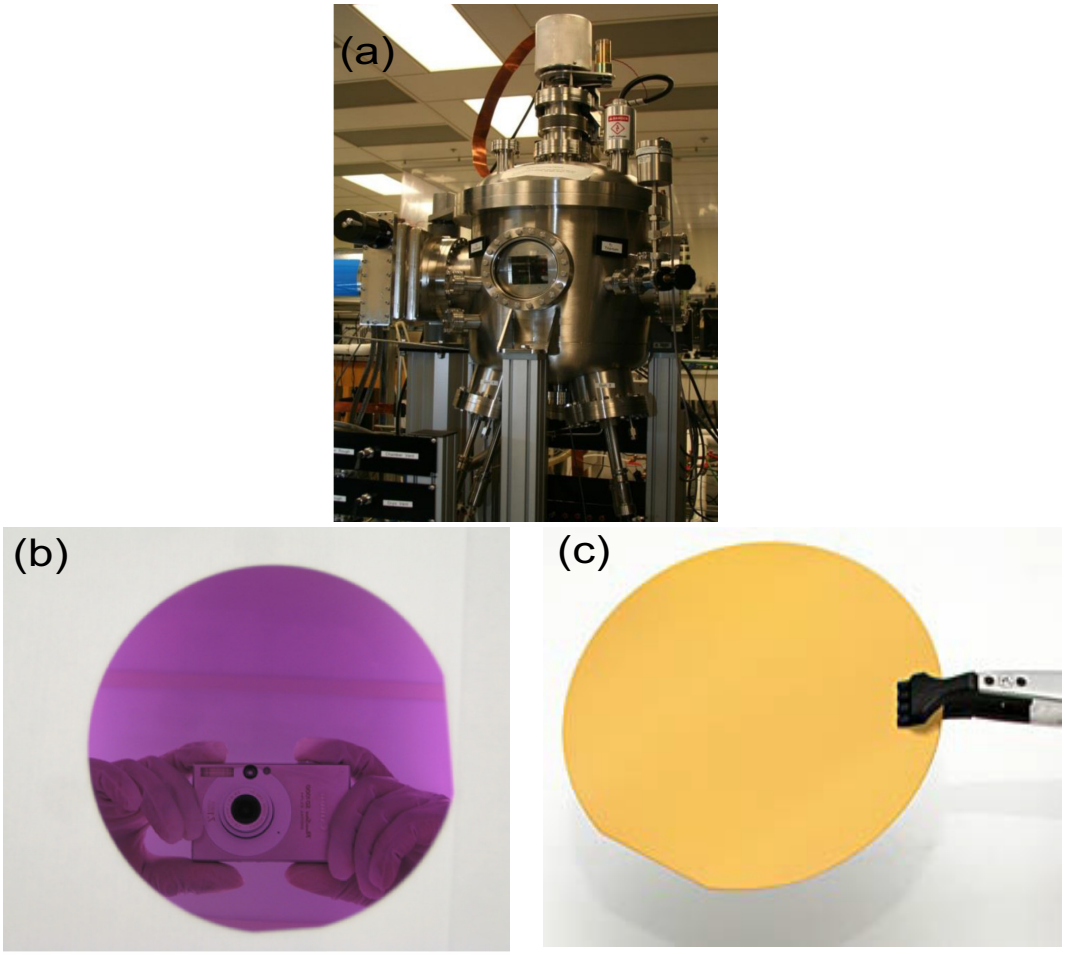

Figure 3.5: (a) Doug sputtering system at nanoFab in University of Alberta, (b) 4-inch diameter silicon nitride wafer before deposition, (c) the same wafer after at first deposition of 10 nm Cr and then 45 nm Au, using the sputtering system.

are directed to strike a target made from the source material to be deposited. Atoms are ablated from the source and are then transported to the substrate by residual kinetic energy. The sputtering tool has been used to deposit 10 nm chromium layer followed by a 45 nm gold layer on the top of Si_3N_4 wafer. The role of chromium layer here is to make better adhesion of gold layer on Si_3N_4 wafer. Deposition rates are 23.10 nm/min and 16.60 nm/min for chromium and gold, respectively. Figures 3.5(b) and (c) show the wafer before and after Cr and Au deposition, respectively. After deposition of Cr and Au, film thickness was measured using a profilometre to ensure the accuracy of the sputtering system.

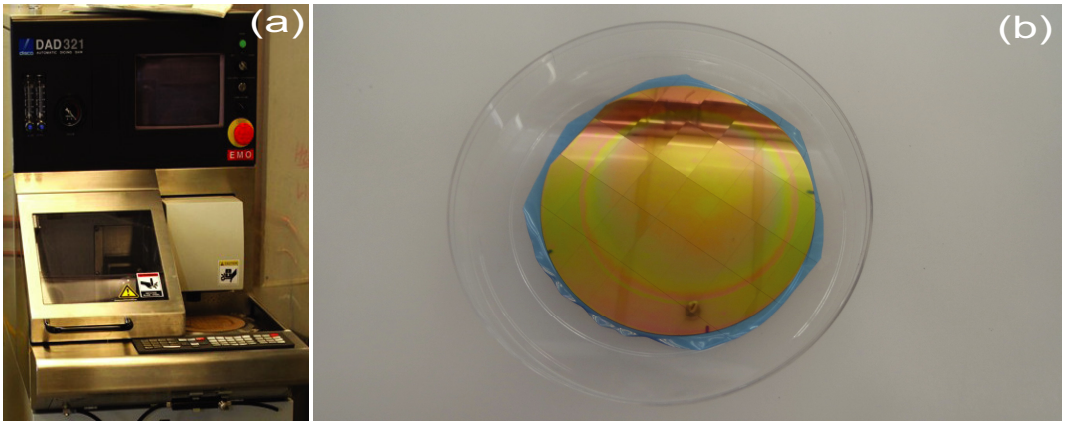

Figure 3.6: (a) Dicing saw (Disco DAD 321) in the nanoFab, and (b) a wafer is diced into 10 mm by 15 mm pieces using this dicing saw.

3.5 Dicing of wafer

After the deposition of Cr and Au on the silicon nitride wafer, the wafer must be diced into suitable pieces which are easy to handle and are fitted to our measurement setup. Before dicing, we deposite a protective layer of photoresist (HPR 504) on the wafer. We dice the gold coated silicon nitride wafer using a mechanical sawing process (Disco DAD 321) as shown in Fig. 3.6(a), to create small pieces with dimensions of 10 mm by 15 mm as shown in Fig. 3.6(b) and 3.8. After dicing wafer, the protective layer of photoresist is removed by using acetone and IPA.

3.6 Lithography process

The most widely used form of lithography is photo lithography, also known UV-lithography. It is the easiest and cheapest technique to create specific patterns on wafer. UV-lamps or UV-lasers are used to expose photosensitive film through photomask. The steps involved in the photolithography process are described in this section.

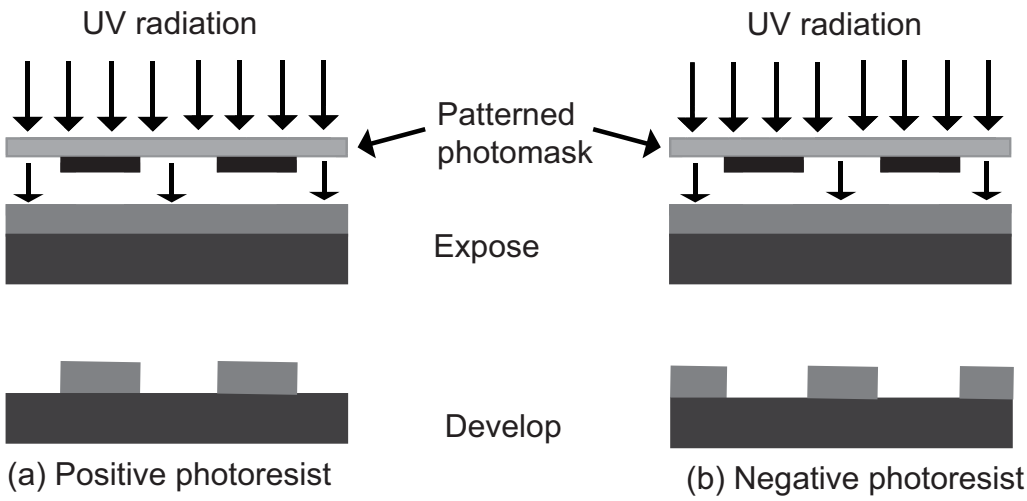

Figure 3.7: UV exposure through a patterned photomask and development of, (a) positive photoresist, (b) negative photoresist. This diagram is reproduced from Ref. [78].

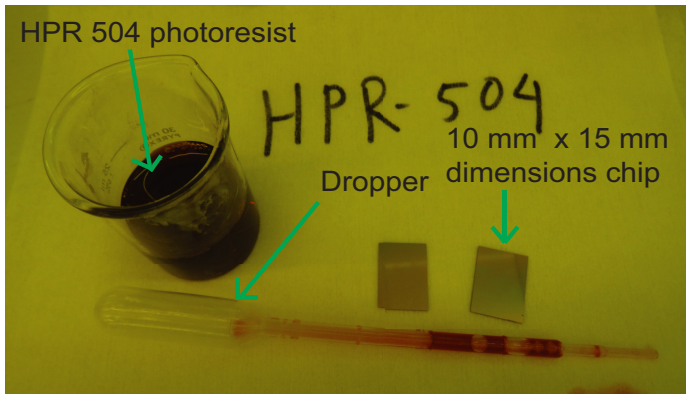

Figure 3.8: A beaker with HPR 504 photoresist is shown on the left. A dropper is used to pour sufficient amount of HPR 504 on the chip. Two 10 mm × 15 mm chips which are used to pattern HPR 504 photoresist.

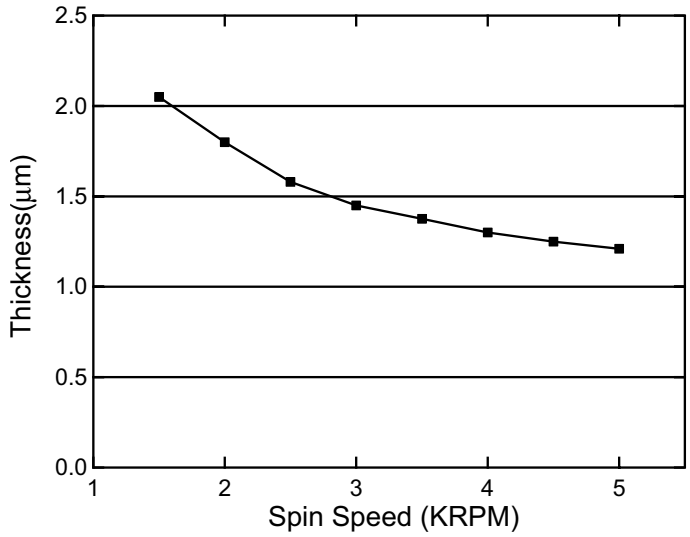

Figure 3.9: The variation of photoresist HPR 504 film thickness with respect to the spinner rotation speed. The data is taken from the nanoFab SOP for HPR 504.

3.6.1 Deposition of photoresist layer

A clean wafer is needed to start depositing a thin film of photoresist on the gold coated silicon nitride wafer. Sometimes we perform Piranha cleaning again if there are visible contaminants on the wafer. The photoresist is a photosensitive organic film containing a photoactive compound, a base resin and an organic solvent system. It is classified as either positive or negative. Positive photoresist is only soluble in a developer if it is exposed to UV shown in Fig. 3.7(a). If a negative photoresist is exposed by UV, the exposed area is insoluble in a developer shown in Fig. 3.7(b). The behaviour of photoresist depends on its sensitivity, contrast and spectral response. In general, the resolution of a positive photoresist is better than of a negative photoresist [78].

For the patterning of my devices, I used HPR 504 photoresist (ethyl lactate polymer), which is shown in Fig. 3.8. Figure 3.9 describes the variation of film thickness of HPR 504 photoresist with the rotation speed of wafer. The photoresist thickness deceases rapidly with increasing rotation speed up to 3500 RPM, while the thickness varies slowly from 3500 RPM to 5000 RPM. For getting 1.25μm uniform thickness of photoresist, I have followed the following steps: firstly, I used a dropper as shown

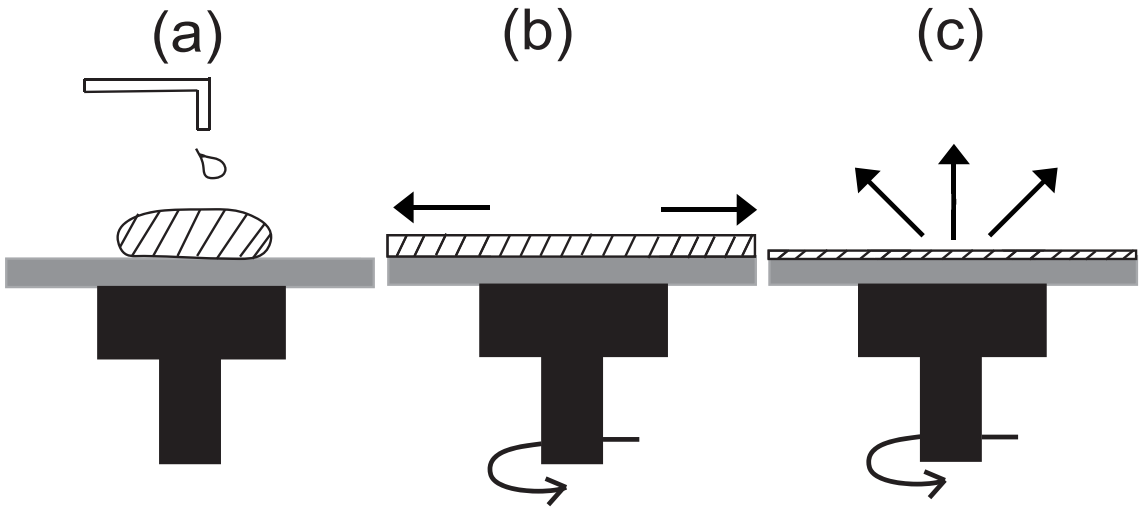

Figure 3.10: Spin coating process, (a) Resist dispensing (few mL) on the chip, (b) preliminary rotation step of 500 RPM for 10 s to spread the photoresist over the whole chip, (c) final spinning step of 4000 RPM for 40 s. This diagram is reproduced from Ref. [78].

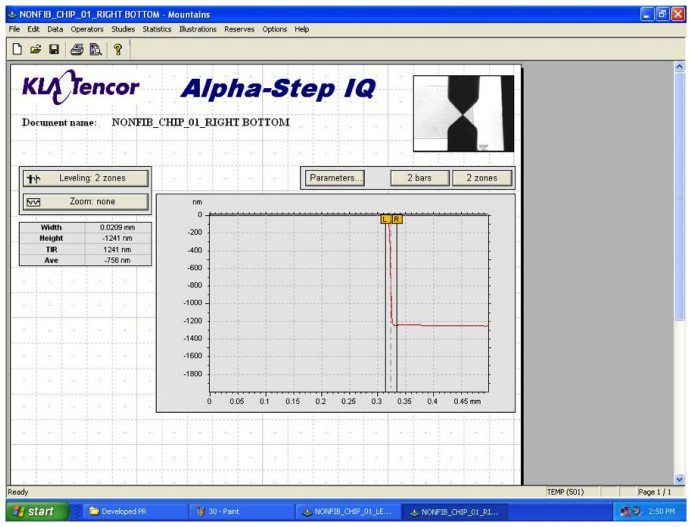

Figure 3.11: Alpha step profilometre scan of HPR 504 photoresist (polymer) showing thickness (1.241μm) and average roughness.

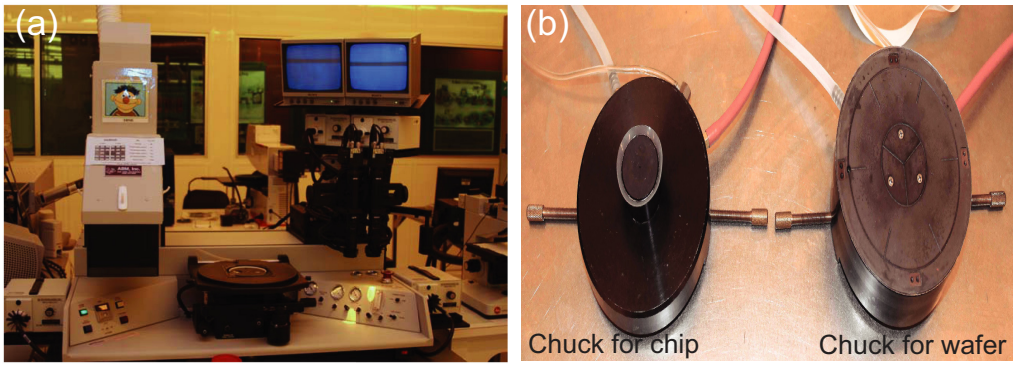

Figure 3.12: (a) ABM mask aligner with Ultra-violate source, (b) The full wafer is mounted on the right big chuck and a small chip is mounted on the left small chuck.

in Fig. 3.8 for pouring sufficient amount of photoresist on the 10 mm by 15 mm chip, which is attached on the chuck of the Solitec spinner as shown in shown in Fig. 3.10(a), after that, I have added a preliminary rotation step of 500 RPM for 10s to spread the photoresist over the whole chip shown in Fig. 3.10(b) and finally, I have spun the chip of 4000 RPM for 40 s which is shown in Fig. 3.10(c). The chip is then soft baked at 120°C for 90 s on a hot plate to drive out any extra solvents. After that, the wafer must be re-hydrated approximately 15 minutes for proper exposure and developing the photoresist. This recipe generates approximately 1.25μm uniform film thickness of HPR 504 photoresist on a clean chip, which is measured by alpha step profilometer shown in Fig. 3.11.

3.6.2 Patterned chips by mask aligner

After re-hydration of chip, it is ready to perform optical lithography. The first and most important step of lithography is mask alignment. For my device, I have used the ABM mask aligner in the nanoFab, which has a UV source, mask aligner, wafer chuck and a mask holder as shown in Fig. 3.12(a) for alignment. The mask aligner can move in 4 translation axes (x, y, z, and θ) including the rotation to align the chip carefully using an optical microscope. The patterned photomask is installed in the mask holder position and a suitable wafer chuck is selected for alignment. The

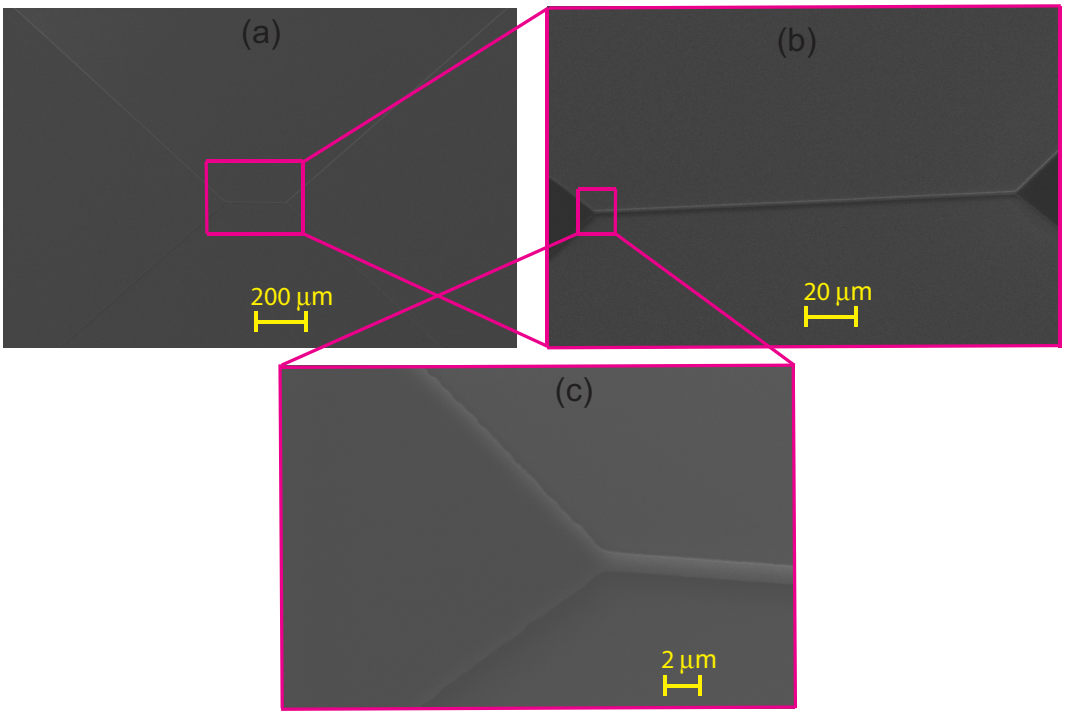

Figure 3.13: Top view images of 215 μm device just after lithography process, (a) patterned photoresist on the chip, (b) zoom in image of string (pink inset), (c) 10× more zoom in image of the same device.

resist-coated chip is in contact with the photomask mask to get very high resolution using the ABM mask aligner. To successfully translate the features patterned in the photomask onto a photoresist chip, good contact by vacuum is preferred to eliminate the gap between the photomask and the chip to minimize diffraction error. However, it is not always possible due to the small chuck as shown in Fig. 3.12(b), that was used to hold small 10 mm × 15 mm chip. The travel distance of the stage did not allow the chip to map all the areas of the 5 inch × 5 inch photomask illustrated in 3.2(b). In this case, the hard contact method should be used. After making contact between photoresist coated chip and photomask, the chip must be exposed to the UV source and developed to transfer the pattern onto the photoresist layer. It is necessary to find the appropriate exposure time for a particular photoresist thickness to get a accurate features.

Exposure time can be estimated by the following relationship,

$$\text{Exposure time} = \frac{\text{Exposure energy}}{\text{Exposure factor}}. \tag{3.1}$$

Since, the exposure energy is constant for a known thickness of a specific photoresist, the exposure time (ET) depends on the exposure factor of the UV system. At a particular exposure factor, it is recommended to tune the ET for proper exposure of that photoresist. After getting the proper ET at that exposure factor, the exposure energy can be calculated easily. Usually, the exposure factor decreases over time for a UV system. Since the exposure energy is constant for a specific photoresist, it is easy to find a new ET at the new exposure factor for that UV system. If the photoresist coated chip is exposed longer than the appropriate ET then the photoresist is over exposed and the corners of the feature on the photoresist are broken. However, if the chip is exposed to UV less than the appropriate ET, then the photoresist is underexposed. In this case, photoresist remains on the exposed area of substrate, even after developing for a long time. For my device, I have optimized ET, which is 1.9 s for approximately 1.25μm thick HPR 504 photoresist for an exposure factor at 68.7mW/cm^2. After exposing the chip by UV-light, the pattern of the nanostring is transferred from the photomask to the surface of the chip. The exposed chip is then developed in a photoresist developer for getting the final pattern. Every photoresist has its specific developer, for HPR 500 photoresist series, the developer is called 354. The development time is also important for getting desired pattern of the device. I found that 45 s is the optimized time for my device. Figure 3.13 shows the SEM images of the top view of a 215μm long nanostring for different zoom in positions just after the lithography process. The thickness of the patterned photoresist is measured and found to be approximately 1.24μm by alpha-step profilometre, which

is shown in Fig. 3.11.

3.6.3 Cleaning the photomask

After performing optical lithography with the same photomask several times, the photomask inevitably collects residue from the photoresist. To clean the photomask, I have used soap and deionized (DI) water to remove the residue from the photomask. When this fails to completely clean the photomask, cold piranha is used to remove any remaining residue. The cleaning process is same as the previous section, with the difference of letting the solution cool down to room temperature. The hot piranha etches the chromium slowly, so the piranha solution must be cooled prior to mask cleaning. The cleaning is done typically for 20 minutes depending on the condition of the mask.

3.7 Etching

After getting the desired pattern of the photoresist on the top of wafer, the underlying materials must be etched to get final pattern of the device. The role of photoresist in this case is to protect the areas where the material needs to remain. Thus, the open areas are etched. There are two types of etching mechanism: Wet etching uses liquid chemicals or etchants to remove materials isotropically (uniformity in all direction), whereas dry etching uses plasmas or etchant gasses that remove materials anisotropically (uniformity in vertical direction only). For fabrication of both gold coated silicon nitride and polymer coated gold nanostring, I used wet etching to remove Au, Cr, and sacrificial SiO_2 layer and dry etching of reaction ion etching (RIE) to remove the Si_3N_4 layer.

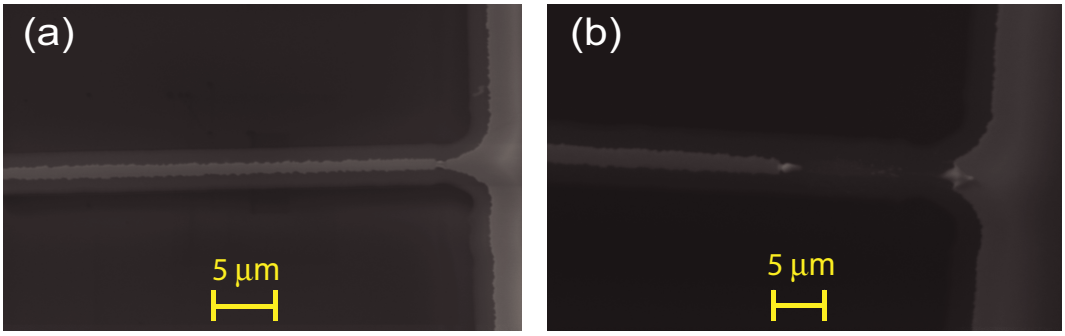

Figure 3.14: Top view of 215 μm long device after uncontrolled gold etching, (a) Etching of gold using existing solution in nanoFab, and (b) Most of the gold of a small portion of the device is etched by the existing solution.

3.7.1 Wet-etching of Au and Cr layer

Wet etching is performed by dipping the patterned chip into aqueous acids or bases which preferentially remove the exposed materials. At first, we need to remove gold layer from the wafer. I have used a gold etchant solution (mixture of Potassium Iodine, Iodine and water). The tentative etching rate of the existing gold etchant solution is 5.3 nm/s which is very fast for etching only 45 nm thick gold layer. This aggressive chemical reaction leaves rough edges after etching, as shown in Fig. 3.14(a). The required time for 45 nm thick gold layer etching is 8.5 s, which is hard to control and sometimes most of the gold from a portion of the string is etched away as shown in Fig.3.14(b). The best way to overcome this problem is to reduce the etching rate of solution by adding DI water. I have made a solution using the existing solution of Au etchant and DI water in a 3 : 1 ratio. This solution reduces the etching rate to approximately 2 nm/s, which produces relatively smooth gold edges. After gold etching, we remove the 10 nm chromium layer using commercially available chromium etchant solution (mixture of ceric ammonium, nitric acid and water). Similarly, the etching rate of this existing solution (3.7 nm/s) is reduced half by adding same amount of DI water with it. This new solution has an etching rate of approximately 1.5 nm/s which allows better control while etching the 10 nm thin layer of Cr.

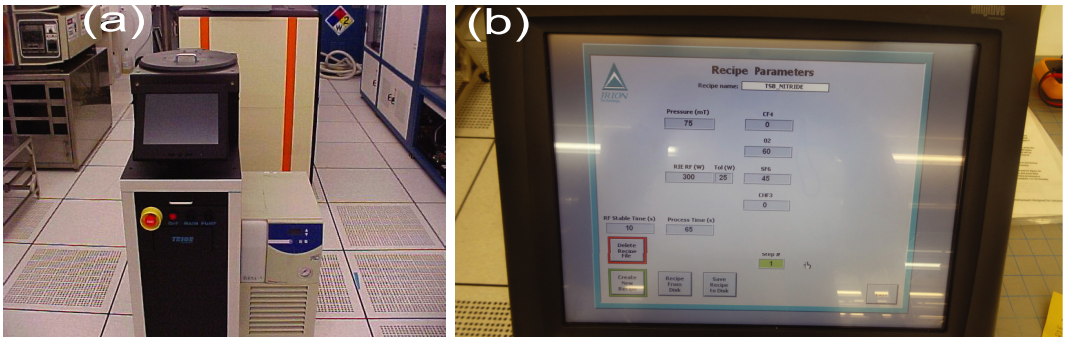

Figure 3.15: Reactive-ion etching (RIE) machine in nanoFab. A snap of the parameters those are used to etch 250 nm Si_3N_4 layer.

3.7.2 Dry-etching (Reactive-ion etching) of Si_3N_4

Dry etching can be described as a removal of some materials by exposing it to a bombardment of ions. It is usually done in a vacuum. The most common type of dry etching for nano-machining applications is reactive-ion etching (RIE). In the RIE process, an etchant gas is introduced into the chamber continuously and a plasma is generated by radio frequency (rf) power. Then a reactive species of ions and radicals are generated in the plasma for bombardment and chemical reaction, respectively. The species are absorbed on the sample and then a chemical reaction occurs and the products leave the surface as volatile gases. This yields highly anisotropic etching at low pressure [55].

We can control the RIE etching rate by pressure, flow of radical gases and radio frequency power (rf). We have used a RIE machine named RIE (Trion) in the nanoFab as shown in Fig. 3.15(a) to etch 250 nm thick high stress silicon nitride layer. The optimized parameters for etching this layer are as follows: pressure 75 mtorr, rf power 300 W, 45 sccm of SF_6, 60 sccm of O_2 and processing time 65 s, which is also presented in Fig 3.15(b). Note that RIE etches the photoresist, and the addition of O_2 enhances the etching rate. We measured the thickness of the remaining HPR 504 photoresist after the RIE process using the profilometre and by taking SEM images, we found that it is approximately 650 nm.

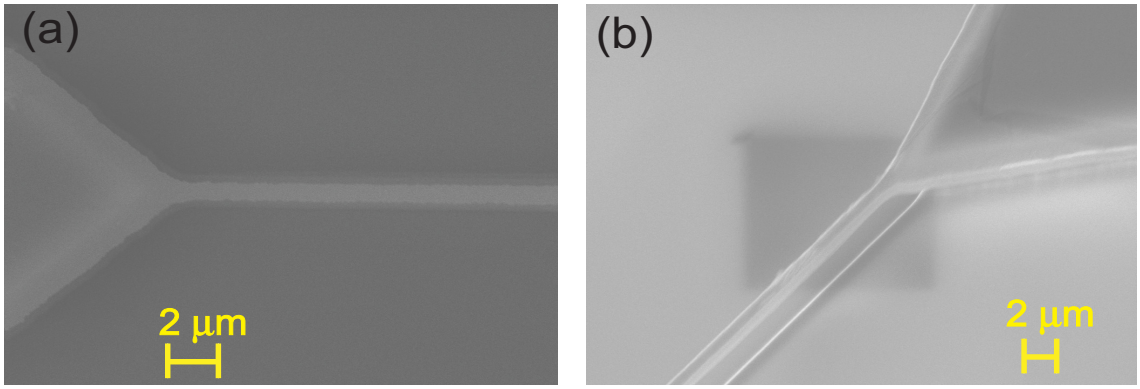

Figure 3.16: A 215 μm long released gold coated silicon nitride string, (a) Top view, (b) 65° tilted view which shows the undercut of the device.

The fabrication process for both gold coated silicon nitride and polymer coated gold devices are the same up to the dry etching of 250 nm Si_3N_4 layer. For gold coated silicon nitride device, we use acetone and isopropyl alcohol (IPA) to remove the remaining approximately 650 nm thickness of photoresist layer. Further dry etching can be done with a different recipe (pressure 400 mtorr, 100% O_2 and 33% rf-power) with a different instrument called RIE (μ etch) if any photoresist residue is left over. However, for HPR 504 coated gold device, we have kept the photoresist as it used in the next step.

3.7.3 Wet-etching the sacrificial layer of SiO_2

Finally, a buffered oxide etch (BOE) process is performed to remove the sacrificial layer of SiO_2. It is a mixture of dilute HF and ammonium bifluoride with the ratio of 10 : 1. The BOE solution etches the SiO_2 layer isotropically, creating an undercut as shown in Fig. 3.16(b) and 3.17(b). The etch rate of this solution was found to be 55 nm/min where the total time for BOE process was determined to be 37 minutes to etch the 2 μm thick SiO_2 layer. The BOE process was performed with extreme caution using plastic beakers (polymethylpentene) and tweezers to immerse the chip in the solution.

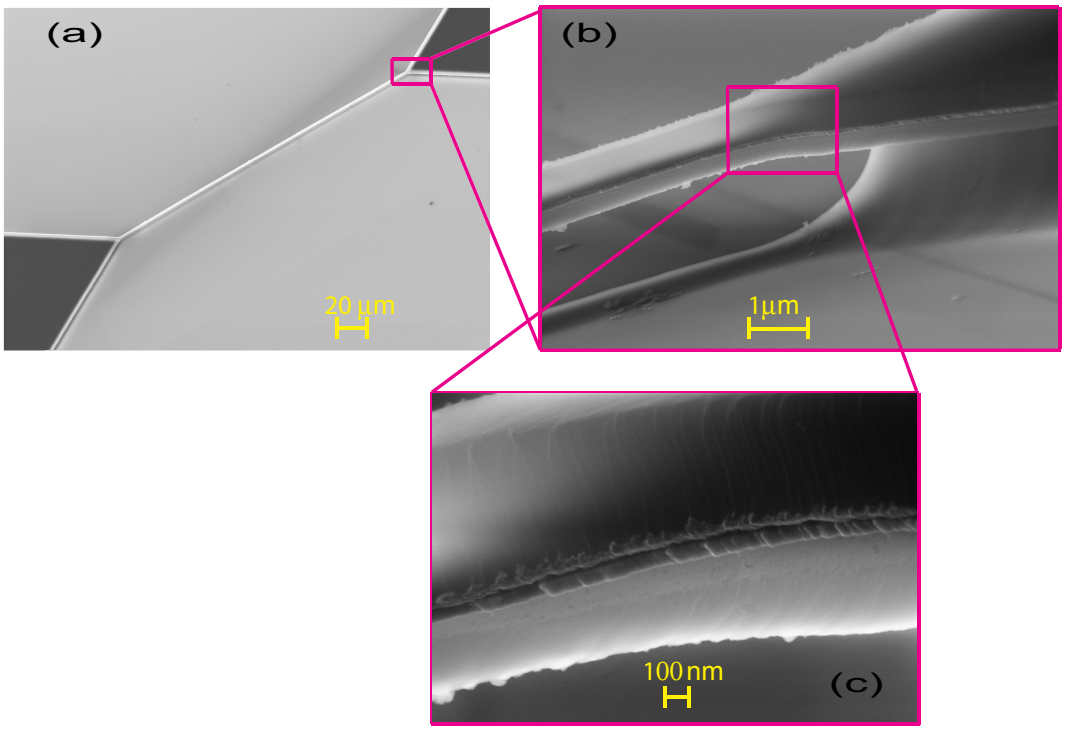

Figure 3.17: A 215 μm long released ethyl lactate coated gold nanostring, (a) Top view, (b) 65° tilted view which shows the undercut of the device, and (c) zoom in image of a portion of the string.

After releasing the chips from the BOE solution, they can be dipped into 5 different water beakers for 1 minute intervals for the polymer coated device. The chips are then dried using nitrogen gas. Finally, the released chips are observed visually. Typically, most of the devices are released properly, however, a few of them may be in striction, which is where the strong capillary force from the surface tension of water makes devices that are close proximity stick together.

However, for gold coated silicon nitride devices, the water-rinsed chips were quickly transferred to an IPA solution, and then underwent a critical drying process at the Nanofab to prevent striction. It is an automated process that needs 45 minutes in duration to complete the process.

There is an alternative method called the solvent method that is used instead of the critical point drier for equivalent results. In this process, I used five different solutions

of pentane and IPA: 100% IPA, 75% IPA + 25% pentane, 50% IPA + 50% pentane, 25% IPA + 75% pentane, and 100% pentane. I dipped chip into each solution for 40 s intervals, which starts with 100% IPA and ends with 100% pentane. After this solvent method, the chips are dried quickly by using nitrogen gas. Finally, we found that, all the devices are released. Figures 3.16 and 3.17 show the SEM of released gold and polymer coated gold devices, respectively.

Chapter 4

Measurement Techniques

This chapter presents the experimental setup and measurement techniques utilized during this study. I have used a simple experimental setup based on optical interference. The description and principle of operation of the interferometric technique is explained in Section 4.1, which has been used for monitoring the resonance frequencies of the nanomechanical resonators. Finally, the resonance frequency measurement of phase-locked loop mode is described briefly in the last section of this chapter.

4.1 Experimental schematic

The apparatus, illustrated in Fig. 4.1, gives an overview of the detection technique of motion of nanostring. The light (a HeNe laser of 632.8 nm wavelength) is passed through a variable optical attenuator (VOA), beam splitter, and an objective and is then focused onto the nanostring, which is in a high vacuum chamber. The split beam can be used for the subtraction of laser noise. Rough alignment can be achieved through the observation of the reflected image through the objective.

The moving nanostring and stationary substrate form a Fabry-Pérot optical cavity, which can be used to sensitively measure the device displacement. In this case, a

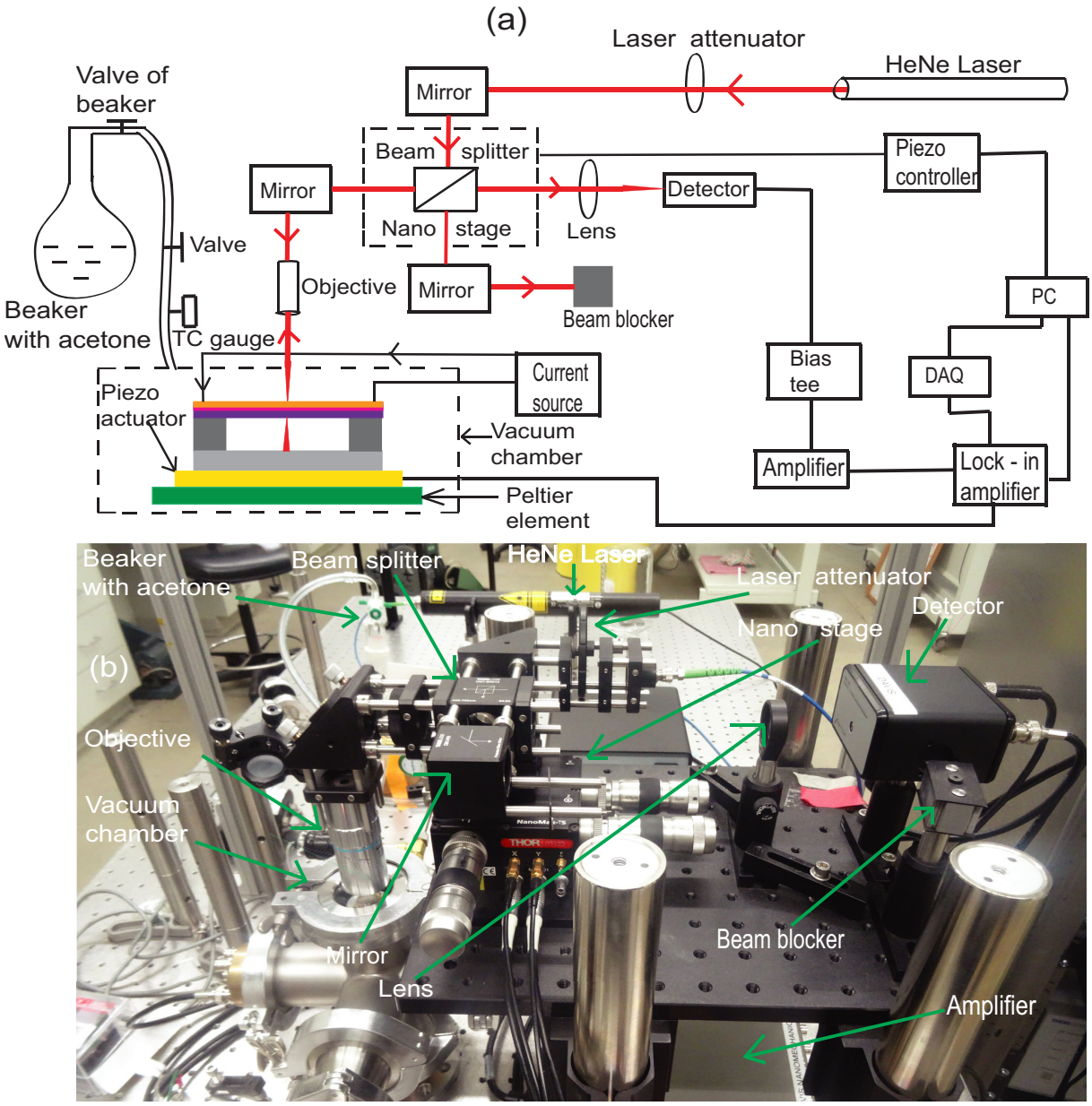

Figure 4.1: (a) Schematic of our experimental setup, and (b) Picture of our experimental setup.

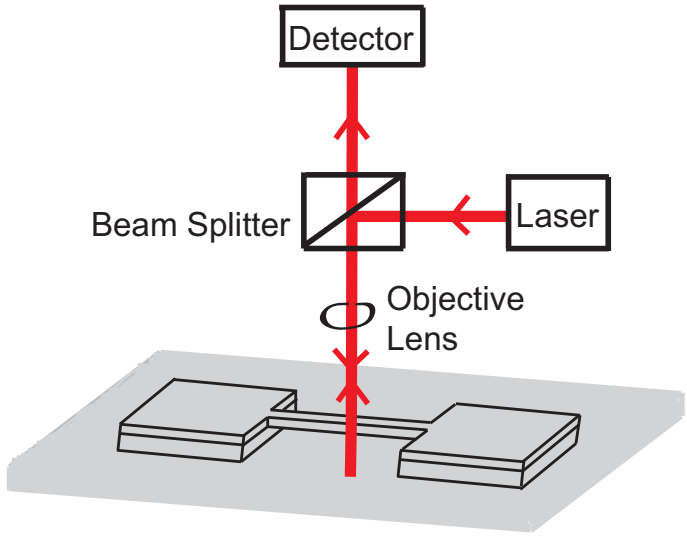

Figure 4.2: Optical interferometric displacement detection in mechanical resonators. A laser beam is focused on the centre of a nanostring through an objective lens. In Fabry-Pérot interferometry, reflected light from the mechanical resonators structure is collimated through the same lens and is directed on to a photodetector. This diagram is adapted from Ref. [39].

small portion of incident light reflects from the upper surface of the moving nanostring and the rest of them reflects from the stationary substrate, as shown Fig. 4.2 [39, 40]. These beams interfere with each other and the resultant interferometric optical signal is transduced to a voltage signal by a photodetector. After that, the photodetector low-pass filters the DC transmission to the data-acquisition (DAQ) device monitored by the computer and high-pass filters the AC signal, which is amplified two times and directed to a high-frequency lock-in amplifier (Zurich Instruments HF2LI) to optimize the amplitude of nanostring mechanical signal motion. A very short BNC cable (10 cm) was used to connect the detector (AC) to the preamplifier to minimize the noise from the cable. For local heating of string resonator, a constant current source (Keithley-2401) is connected to a circuit via BNC such that current flows across the nanostring.

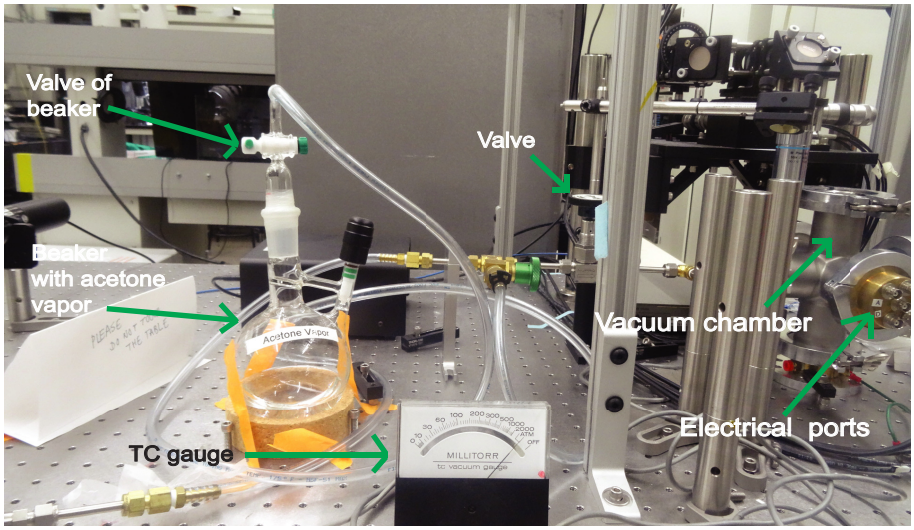

Figure 4.3: Picture of our experimental setup for injection of acetone into the vacuum chamber.

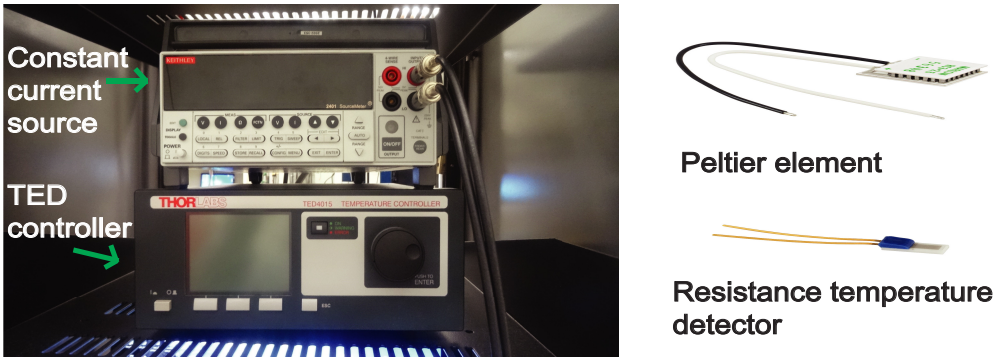

Figure 4.4: Left-top is the constant current source (Keithley-2401) and bottom one is thermoelectric temperature controller. Right top is the Peltier element and bottom one is the resistance temperature detector (PT-1000). The figures of Peltier element and resistance temperature detector are taken from thorlabs website.

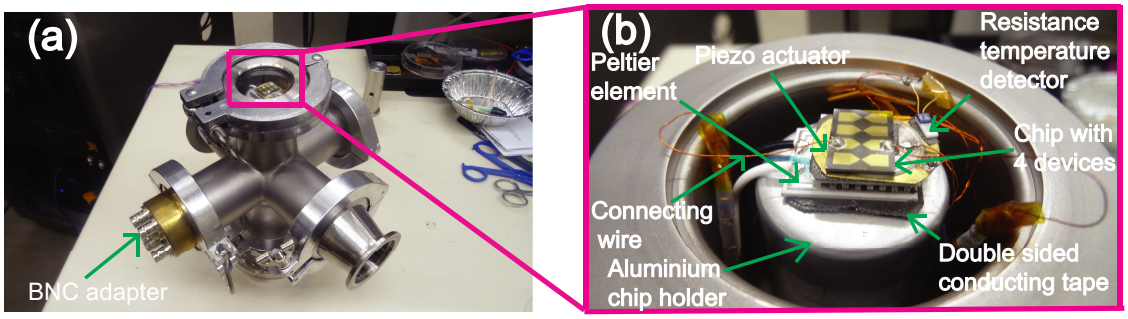

Figure 4.5: (a) A home made vacuum chamber, (b) zoom in (pink inset part) of the important parts of vacuum chamber.

To measure the physisorption of acetone, we have modified our experimental setup. Firstly, we have attached a beaker of liquid acetone to the vacuum chamber through two valves (one is with the beaker and another one is at the middle of connecting pipe), which is shown in Fig. 4.3. The attached thermocouple (TC) vacuum gauge is used to measure the amount of injected acetone into the vacuum chamber. We have also installed a Peltier element which is controlled by a thermoelectric temperature controller (TEC) as shown in Fig. 4.4, that is used to reduce the temperature of the chip and a resistance temperature detector (PT-1000) as shown in Fig. 4.4, that is used to measure the temperature of chip.

4.2 Laser power attenuation

The incident laser power can by varied from 0 to 200 μW by optical power attenuation. It is confirmed in Ref. [23] that the resonance frequency of Si_3N_4 string does not shift as a function of optical laser power due to low absorption in the visible region. However, the metallic layer on the top of the silicon nitride increases the light absorption. In Ref. [34], our group observed that 30 μW is the lowest optical power

capable of removing the gold (43 nm thick) from the string. In order to avoid heating effect by laser, I have used the optical power of laser of 17 μW for all measurements.

4.3 Vacuum chamber

The vacuum chamber, which was machined at the University of Alberta physics machine shop, is shown in Fig. 4.5(a). It is capable holding a vacuum on the order of 2×10^{-6} Torr. Figure 4.5(b) illustrates the cylindrical 6.375-inch long and 1.5-inch diameter aluminium chip holder, which is attached at the centre of the chamber. On the top of aluminium chip holder, we place a piezoelectric buzzer to actuate the nanostring. The chip lies on the top of this piezoelectric buzzer. For the measurement of physisorption of acetone, we insert a Peltier element between the chip holder and piezoelectric buzzer. In addition, we place a resistance temperature detector (PT-1000) to measure the temperature of the chip. A glass window on top of the vacuum chamber allows for accurate alignment of nanostring with the laser beam using nanopositioning stages to manipulate the chip. In addition to the description inside the vacuum chamber, the external 4 ports: vacuum parts, a beaker of acetone, a constant current source, and thermoelectric temperature controller will be explained.

4.3.1 Vacuum parts

The purpose of making a high vacuum chamber is to preserve the intrinsic Q- factor of the device by redusing mechanical damping due to air. In order to ensure high vacuum is obtained, all connections between the vacuum chamber and pump were sealed with O-rings coated in grease. We pumped air out of the chamber and used a He leak sniffer to sense if the seals were leaktight. We found that the seals were leaktight, which allows the chamber to reach approximately 2×10^{-6} Torr.

4.3.2 Beaker of acetone

A beaker of liquid acetone is attached to vacuum chamber. The acetone vapour is at room temperature and ambient pressure. Two valves (one at the beaker, one at the middle of connecting pipe) are used to control the flow of acetone into the vacuum chamber. The pressure of the acetone vapour was calculated using the pressure measured by a thermocouple (TC) vacuum gauge, which is calibrated with nitrogen gas, then divided by the acetone gas correction factor of 2.09 [79].

4.3.3 Constant current source

For local heating of nanostring, we have used a constant current source as shown in Fig. 4.4, which is controlled by labview. Electrically conductive silver epoxy is used to attach two small pieces of wire on either side of the nanostring. The opposite terminals of the wires are connected to BNCs which have terminals inside the vacuum chamber. The current source is connected to the opposite terminal of BNCs (outside of the vacuum chamber) via a KF 25 flange.

4.3.4 Thermoelectric temperature controller

The thermoelectric temperature controller is used to reduce the temperature of the chip. The advantage of this is that, TEC only cools down the chip of nanostrings, and does not adversely affect any other part of our experimental system. It is connected with the Peltier element, which creates a temperature difference between its two surfaces. In our case, when current passes through the Peltier element, its upper surface (piezoelectric buzzer is attached on this surface) becomes cold and lower surface becomes hot (attached with aluminum holder). By optimizing the parameters of a PID controller, we can reach by $-10°$ C. However, when we fill the vacuum chamber with room temperature and ambient pressure acetone vapour, then we can cool down

around $-8°$ C. For this reason, the measurements of the resonance frequency as a function of current and time are performed at $-7.5°$ C. To measure the variation of resonance frequency as a function of temperature, temperature is cooled down from $35°$ C to $-7.5°$ C in steps of $5°$ C and the temperature was allowed to stabilize before the resonance frequency is measured.

4.4 Resonance frequency of phase-locked loop mode

Phase-locked loop (PLL) is a very useful technique in both analog and digital circuits, with applications for radio, telecommunications, and computers [80]. In nanomechanical resonator research, this technique is employed to track the resonance frequency of the resonator in real time. PLL is usually a dynamic mode measurement because the nanostring resonator is kept in oscillation during data acquisition. It can measure only the frequency shift of the resonator and does not provide information about the spectral response. PLL consists of three core elements connected in a fedback loop: a phase detector (PD), a loop filter (LF), and a voltage-controlled oscillator (VCO) [81], as illustrated in the block diagram of Fig 4.6. The working principle of the PLL can be explained as follows: the phase of a periodic input signal is compared with the phase of a VCO signal at the phase detector and the difference is output as an error signal. This error signal is fedback to the control port of the VCO after a low-pass loop filter, and tunes the VCO frequency toward the input signal's frequency to reduce the error signal and close the loop. In the locked state, the VCO frequency will be exactly equal to the frequency of the input signal within the loop bandwidth [80, 82]. If a resonator is actuated, there is a phase difference between the actuator (piezo buzzer in this case) and the amplitude oscillation (nanostring in this case) which is a function of the actuation frequency ω_d [82] as derived in Eq. 2.16

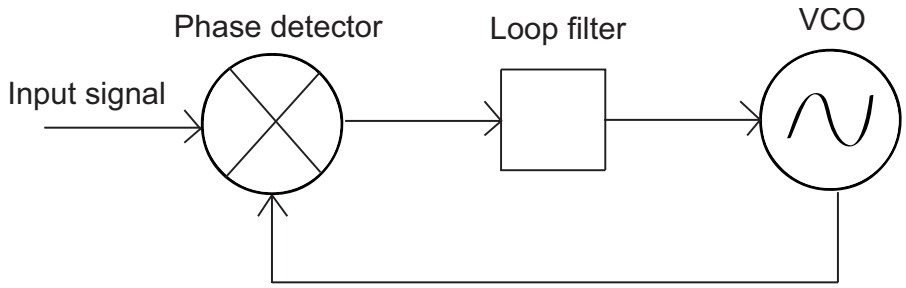

Figure 4.6: Block diagram of the phase-locked loop (PLL) comprising three main components: phase detector, loop filter, and voltage-controlled oscillator (VCO). This diagram is reproduced in Ref. [81].

$$\phi = \tan^{-1}[\frac{-\omega_o \omega_d}{Q(\omega_o^2 - \omega_d^2)}]. \tag{4.1}$$

At the resonance, $\omega_d = \omega_o$, the phase shift is $-90°$. So, the actuating signal is $-90°$ shifted and continuously compared to the signal of the nanostring defection. If ω_d is set to be equal to ω_o, the phase difference of the two signals is zero. If the resonance frequency changes for any reason (in this case, by changing current/temperature), the phase difference (error signal) will be different of zero. This error signal controls the actuating signal and changes it in order to null itself, like in a negative feedback system. In this way, the variation of resonance frequency can be tracked continuously and quickly.

Chapter 5

Detection of Mass of Polymer

Nanomechanical resonators have been demonstrated as a mass sensor with unprecedented sensitivity when the change in their resonance frequency is measured with the change of their inertial mass [6, 7, 8]. This chapter will describe the mass detection of ethyl lactate polymer using nanostring resonator. Note that the polymer was deposited on the nanostring during the fabrication process (particularly during the optical lithography process). A computer-controlled phase-locked loop (PLL) was used to track the resonance frequency of the nanostring in high vacuum approximately 2×10^{-6} Torr and at room temperature in real time. A constant current source (Keithley 2401), controlled by a labview program, is connected across the nanostring to pass current through the device and generates ohmic heating across the device. The resonance frequency of nanostring as a function of current was extracted. Then, I extracted relative resonance frequency shift as a function of current for both gold coated Si_3N_4 (reference device) and polymer coated gold devices. For quantification of desorped polymer, the resonance frequency versus current for different current sweeps was studied. Resonance frequency as a function of time for different values of current was also studied like thermogravimetric analysis and then the desorption of polymer

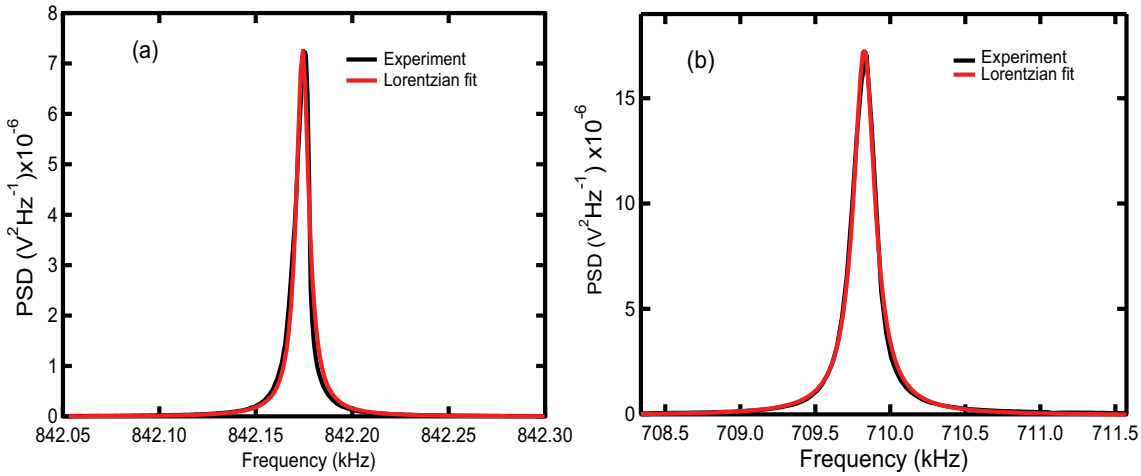

Figure 5.1: Fundamental mode resonance response. Power spectral density of, (a) a gold mechanical resonator (b) a polymer coated mechanical resonator. Red lines are fit of the data to the Lorentzian profile.

was extracted qualitatively with time.

First, the resonance frequency of gold and ethyl lactate polymer coated resonators of the same dimension (215 μm long) were measured. I fitted the data to a Lorentzian profile to extract the resonance frequency of the nanostrings. Figure 5.1 illustrates the experimental power spectral density (PSD) as a function of frequency. This is the fundamental mode response of the gold and the polymer coated nanostrings in vacuum at room temperature. From the fits, we found that the resonance frequencies are 842.174 $\pm$ 0.001 kHz and 709.832 $\pm$ 0.001 kHz for the gold and the polymer coated nanostrings, respectively. There is a large frequency difference of 132.342 kHz which is due to the additional mass of the polymer on the polymer coated device.

The mass of the polymer layer on the nanostring was calculated from the dimensions of the polymer coated device. The thickness of polymer can be measured to be around 650 nm from the SEM pictures of the polymer coated nanostring, which is shown in Fig. 5.2.

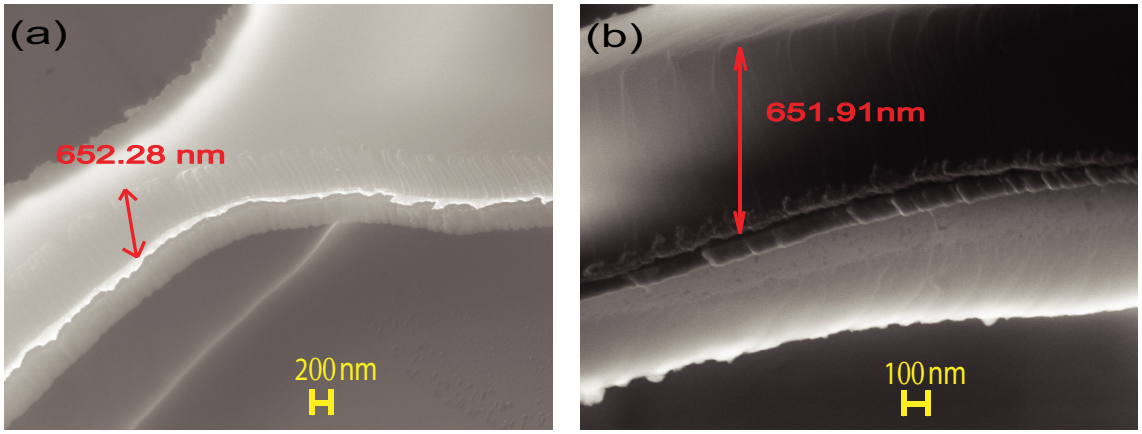

Figure 5.2: (a) SEM image of 215 μm long nanostring. It shows that the thickness of polymer layer is approximately 650 nm, (b) zoom in image of the same nanostring.

For getting a better understanding of dimensions of the devices, I included the schematic diagram of both cross-sectional area of gold and polymer coated gold device in Fig. 5.3. The dimensions of 215 μm long gold and polymer coated devices were presented in table 5.1. The densities of the materials of the nanostring and polymer also were presented in table 5.1. Using the dimensions (volume) and the densities corresponding of them, the mass of each layer was calculated and presented in table 5.1. The calculated masses of 215 μm long gold and polymer coated gold devices are 927 pg and 1252 pg respectively, and hence, the mass of polymer layer is approximately 325 pg.

For observing the behaviour of resonance frequency with current of gold coated silicon nitride nanostring, a direct current (DC) source was connected across the 215 μm long gold nanostring resonator to pass current through it. The ohmic heating is generated only on the surface of the nanostring due to current flow. The resonance frequency with varying current was tracked using PLL in vacuum of approximately 2×10^{-6} Torr at room temperature. Note that, due to the limitations of the lock-in amplifier (Zurich Instruments HF2LI), the PLL can not track the variation of

Table 5.1: Dimensions of 215 μm long polymer coated nanostring resonators, which were measured using the SEM image of the device shown in Fig. 5.2. The density of nanostring materials (Si_3N_4, Cr, and Au) [34] and polymer (HPR 504 photoresist) [83, 84] were also included. From the density and volume relationship, the mass of each layer of the nanostring was calculated.

Layer	Thickness nm	Width μm	Length μm	Volume cm^3	Density g/cm^3	Mass pg
Si_3N_4	250	2.81	215	1.51×10^{-10}	3.05	460
Cr	10	2.32	215	4.98×10^{-12}	7.19	35
Au	45	2.32	215	2.24×10^{-11}	19.30	432
Polymer	650	2.32	215	3.24×10^{-10}	1.03	325

Table 5.2: Dimensions of 195 μm long polymer coated nanostring resonators, which were measured using the SEM image of the device. The density of nanostring materials (Si_3N_4, Cr, and Au) [34] and polymer (HPR 504 photoresist) [83, 84] were also included. From the density and volume relationship, the mass of each layer of the nanostring was calculated.

Layer	Thickness nm	Width μm	Length μm	Volume cm^3	Density g/cm^3	Mass pg
Si_3N_4	250	2.24	195	1.09×10^{-10}	3.05	332
Cr	10	1.92	195	3.74×10^{-12}	7.19	27
Au	45	1.92	195	1.68×10^{-11}	19.30	324
Polymer	650	1.92	195	2.43×10^{-10}	1.03	250

Table 5.3: Material properties of nanostring resonators and substrate. The table is taken from Ref. [34].

Layer	Young's modulus E GPa	Thermal expansion expansion α $\times 10^6 K^{-1}$	Specific heat C J/KgK	Resistivity ρ nΩm	Thermal conductivity κ W/m.K
Au	79	14.2	129.1	22.14	318
Cr	279	4.9	448.2	125	93
Si_3N_4	265	1.27	700	∞	30
Si	-	-	2.59	-	-

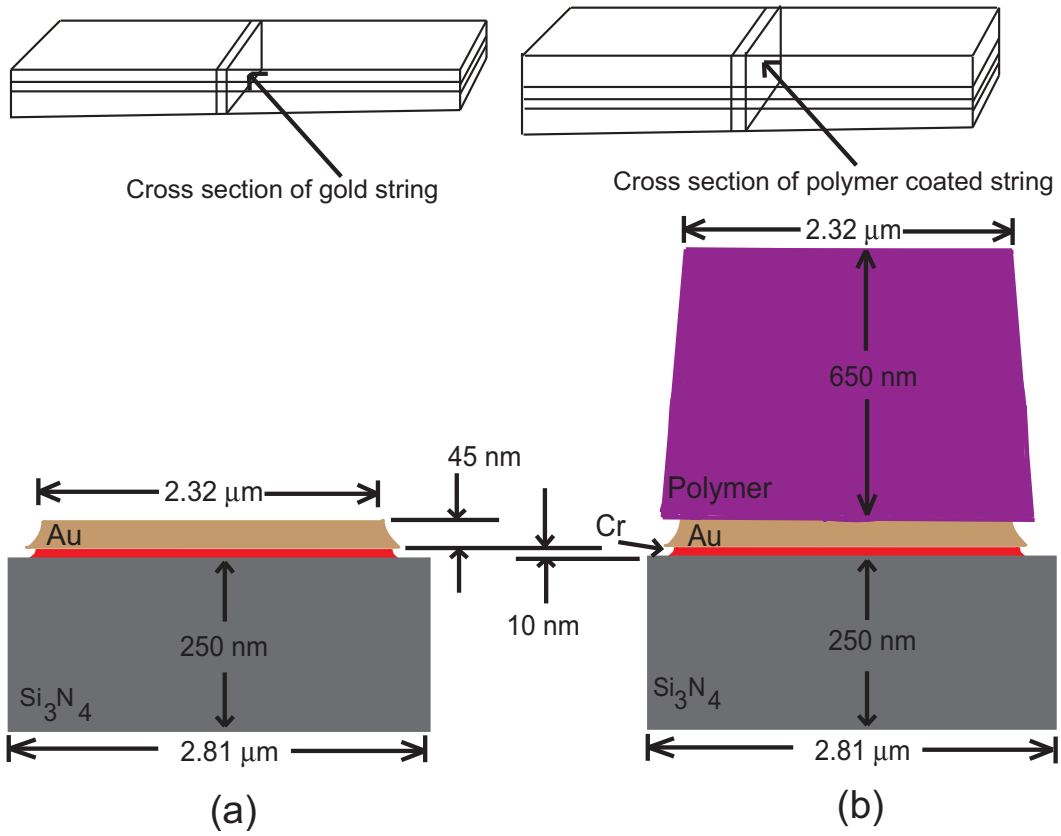

Figure 5.3: Schematic diagram of cross-sectional area of (a) gold coated silicon nitric nanostring, (b) polymer coated gold nanostring.

resonance frequency for the complete 0 μA - 1000 μA range. Due to this reason, the sweep was paused at 450 μA to reset the PLL. This procedure was followed for all measurements of the variation of resonance frequency with current. I found the effect of resetting the PLL drive, these experiments had negligible effect for both gold and polymer coated devices. The obtained data for the variation of resonance frequency with current for gold coated nanostring is presented in Fig 5.4. The relative resonance frequency shift was extracted from the resonance frequency data which is presented in Fig 5.5. Figure 5.4 shows that resonance frequency decreases with current. The reason behind this behaviour is that when current passes through the nanostring, the Ohmic heating generates on the surface of the nanostring only. The resistance

to an electrical current through the metallic gold layer of the string causes this local heating. In the presence of this local heating on the string surface, the materials of the string expand while the substrate does not change. Note that, based on Eq. 2.32, the resonance frequency of the resonator depends on the effective mass of the resonator and its spring constant. As the temperature increases due to local heating, the spring constant of the nanostring decreases while the mass of the nanostring remains the same. So, the nanostring's strain is reduced. Thus, the resonance frequency decreases with current. Recently our group in [34] has modeled this phenomenon. They have derived the resonance frequency shift due to local heating on the surface of the nanostring, which is given by

$$\begin{aligned}\frac{f_n(I)-f_n(0)}{f_n(0)} &= -\frac{L}{8\sigma A_1 R}\left(\frac{\sum_{k=1}^{3} A_k E_k \alpha_k}{\sum_{k=1}^{3} A_k E_k \kappa_k}\right) V^2 \\ &= -\frac{LR}{8\sigma A_1}\left(\frac{\sum_{k=1}^{3} A_k E_k \alpha_k}{\sum_{k=1}^{3} A_k E_k \kappa_k}\right) I^2, \end{aligned} \tag{5.1}$$

where $f_n(I)$, $f(0)$, L, R and σ are the resonance frequency at current I, the resonance frequency at zero current, the length, resistance of the nanostring and tensile stress of the Si_3N_4 layer, respectively. Note that, α_k, E_k, A_k and κ_k are the corresponding thermal expansion coefficients, Young's moduli, and cross-sectional areas, and thermal conductivity, respectively. Here V is the applied DC voltage across the nanostring and I is the corresponding current. The material parameters are defined for each layer with indices $k = 1$ (silicon nitride), $k = 2$ (chromium), and $k = 3$ (gold). Eq. 5.1 describes that the relative frequency shift is quadratic in I and always negative. The coefficient of I^2 in Eq. (5.1) can be written as

$$\frac{LR}{8\sigma A_1}\left(\frac{\sum_{k=1}^{3} A_k E_k \alpha_k}{\sum_{k=1}^{3} A_k E_k \kappa_k}\right) = \frac{LR}{8\sigma A_1}\left(\frac{A_1E_1\alpha_1 + A_2E_2\alpha_2 + A_3E_3\alpha_3}{A_1E_1\kappa_1 + A_2E_2\kappa_2 + A_3E_3\kappa_3}\right) \tag{5.2}$$

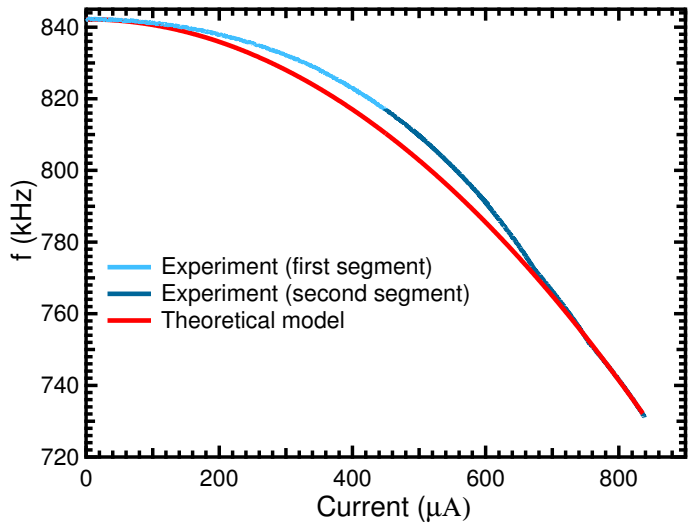

Figure 5.4: Resonance frequency versus current of gold nanostring. The blue line (lower current region) is the first segment of the phase-locked loop data and the deep blue (higher current region) is the second segment of the phase-locked loop data. Red line is the theoretical model of Eq. 5.3, where $f_n(0)$ is the resonance frequency (842.17 kHz) at current zero.

Using the tabulated values of the dimensions of the nanostring in table 5.1, the material properties of nanostring in table 5.3, and also plugging the measured values of R (165 Ω) and reported values of σ (0.8 GPa) [23, 75, 76], the values of Eq. 5.2 to be 185674 A^{-2}. Thus, Eq. 5.1 can be written as

$$\frac{f_n(I) - f_n(0)}{f_n(0)} = 185674 I^2 \tag{5.3}$$

I plotted resonance frequency, $f_n(I)$ with I, using Eq. 5.3, where $f_n(0)$ (842.174 kHz) is the resonance frequency at zero current, which is presented in Fig. 5.4. The graph shows that the theoretical model agrees well with experimental data.

For the calculation of desorption of ethyl lactate polymer, I mounted a polymer coated nanostring in the vacuum chamber and connected a DC current source across it. After that, I tracked the resonance frequency of the nanostring (same dimensions of gold device that I plotted before) with current in vacuum at room temperature.

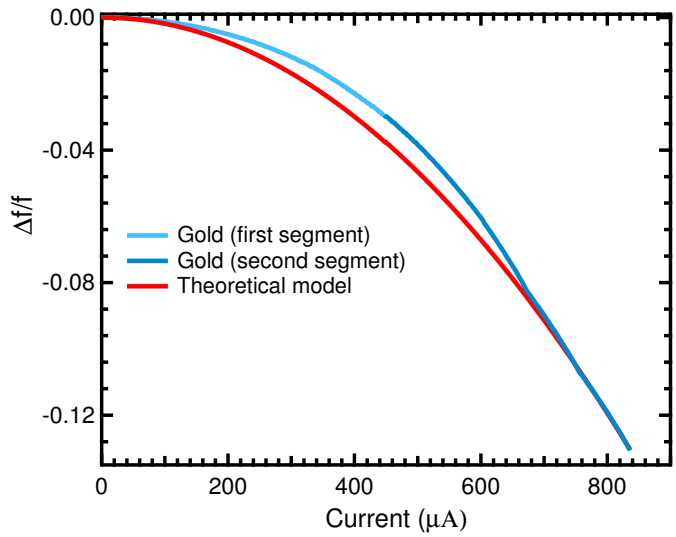

Figure 5.5: Relative resonance frequency shift versus current of gold nanostring. The blue line (lower current region) is the first segment of the phase-locked loop data and the deep blue (higher current region) is the second segment of the phase-locked loop data. Red line is the theoretical model of Eq. 5.3.

Note that, I took current sweep by two segments due to unlocked the PLL at around the middle of the sweep similar to the current sweep of gold device. I plotted the obtained result in Fig. 5.6 and then compared it with the gold coated silicon nitride nanostring. Figure 5.6 shows that there is a large frequency difference, 132.342 kHz, between the gold and polymer coated nanostrings. This difference is due to the mass of additional layer of polymer as mentioned earlier. To get better understanding about these results (with and without polymer), I extracted the relative resonance frequency shift, $\frac{\Delta f}{f}$, as a function of current, which is demonstrated in Fig. 5.7. The polymer coated string, resonance frequency decreases identically to the gold string up to 400 μA. Above this current, it decreases more slowly than the gold string until 650 μA, where the resonance frequency begins to increase slowly up to 800 μA. This trend is opposite to that of gold nanostring. Finally, the resonance frequency of the polymer coated nanostring decreases sharply. The reason behind this behaviour is as follows: in the low current region (up to 400 μA), both nanostrings follow the same nature because the spring constant changes in the same rate for both nanostrings due

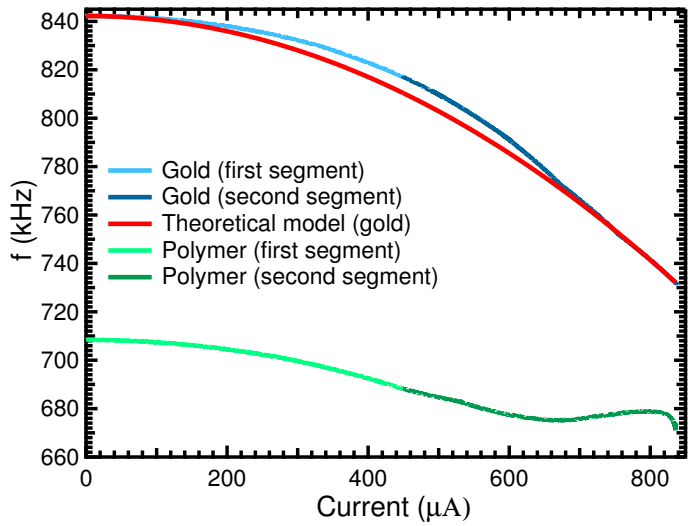

Figure 5.6: Resonance frequency versus current for both 215 μm long gold (blue for lower current region and deep blue for higher current region) and polymer coated (cyan for lower current region and green for higher current region) devices. Red line is the theoretical model of Eq. 5.3, where $f_n(0)$ is the resonance frequency (842.17 kHz) at current zero. The frequency difference between these two same dimension of devices is due to the additional mass of polymer.

to Ohmic heating. The mass of polymer remains the same due to insufficient amount of heat generated by this amount of current to remove the polymer.

The behaviour from 400 μA to 650 μA indicates that, for gold coated device, the spring constant decreases with current but for polymer coated device, both spring constant and mass of the polymer change with current. Due to this reason, the polymer coated device does not follow the behaviour of gold device. So, generated heat produced by current starts removing polymer from the nanostring slowly. On the other hand, after 650 μA, the gold and polymer coated nanostrings follow opposite behaviour, which indicates that the rate of change of spring constant is the same for both gold and polymer nanostring but the mass of polymer for polymer coated nanostring decreases due to the generated heat produced by current while the mass remains the same for gold nanostring.

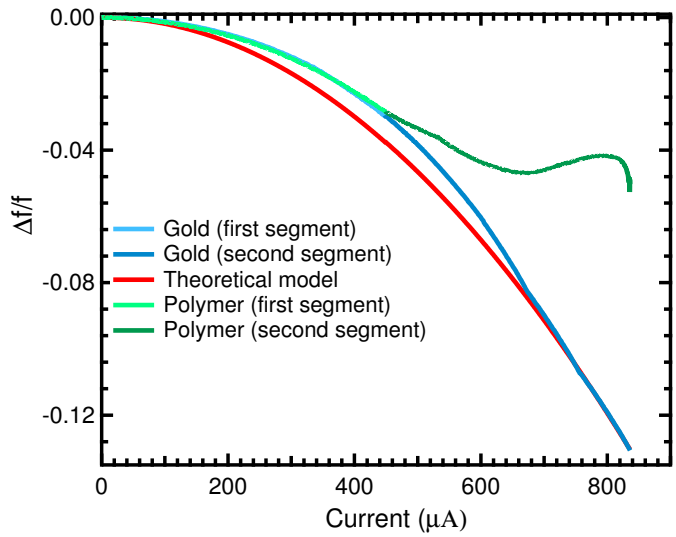

Figure 5.7: Relative resonance frequency shift versus current for both 215 μm long gold (blue for lower current region and deep blue for higher current region) and polymer coated (cyan for lower current region and green for higher current region) devices. Red line is the theoretical model of Eq. 5.3. The frequency difference between these two same dimension of devices is due to the additional mass of polymer.

In the high current region (after 800 μA), they follow the same nature. The reason behind this observation is that at high current, there is a competition between the effect of the change of spring constant and the polymer desorption. Note that the required time for a complete current sweep from 0 μA to 850 μA is around 2 minutes. Since the current sweep is fast, the effect of change of spring constant dominates, rather than polymer desorption. Thus, the relative resonance frequency decreases sharply with high current.

For checking the reproducibility, I measured the resonance frequency as a function of current for 3 different lengths of polymer coated devices: 195 μm, 205 μm, and 215 μm. I followed the same procedure to take the current sweep as described before. From their resonance frequency, the relative resonance frequency shifts were extracted as a function of current, which is presented in Fig. 5.8. It shows that the

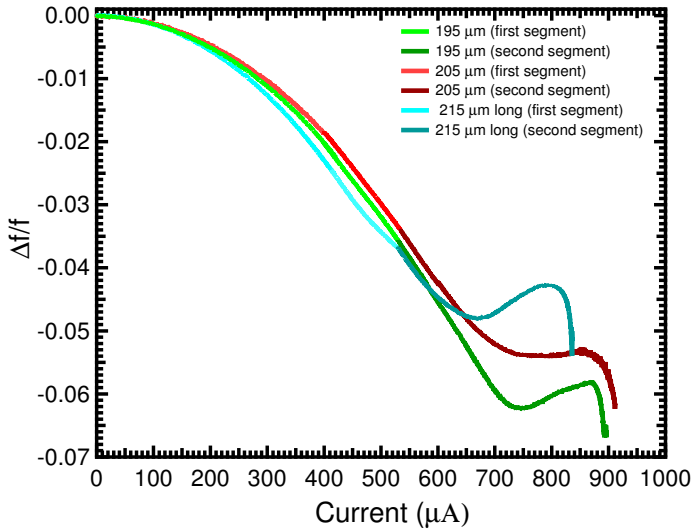

Figure 5.8: Relative shift of the resonance frequency as a function of current for three different dimensions of polymer coated devices. Blue one is 215 μm long, red one is 205 μm long, and cyan one is 195 μm long. I used two different colours for each device to indicate different segments of phase-locked loop data.

behaviour of the devices is reproducible.

For the quantification of desorped polymer, I measured the resonance frequency of the same devices for different current sweeps. After completion of each sweep, there was an initial frequency shift (when current is equal to zero) to the upper value. This frequency shift is due to the change of mass of the polymer not the change of spring constant and mass of any other materials (gold and chromium) of the nanostring. This is evident because the frequency shift was measured at zero current which was independent of the effect of spring constant. I also measured the resistance of the device before and after current sweeps and found that it was the same which means that gold and chromium remain the same after current sweeps. The authors in Ref. [34] described that the whole gold layer of the gold coated silicon nitride device remains the same up to 2.0 mA current passing along the metallic gold layer. For my experimental measurements, I passed maximum 1.0 mA current to ensure the materials (Au and Cr) of the devices remain unchanged. Figure 5.9 shows the

resonance frequency of the 215 μm long string for 3 different current sweeps. From this graph, I measured the resonance frequency after the completion of each current sweep and found that the resonance frequency shifts to the upper value, which is presented in table 5.4. This frequency shift indicates that the desorption of polymer is due to local ohmic heating, which is generated by current passing through the metallic gold layer of the string. The amount of desorption of polymer due to local heating can be calculated quantitatively using Eq. 2.43. The calculated desorption of polymer for the 215 μm nanostring is tabulated in table 5.4. After the 1st sweep, around 12% mass of polymer is removed from the string and after the 2nd sweep, 26% mass is removed from the nanostring. Note that, we were not able to measure the frequency shift for the 3rd sweep due to destroying the device during the 3rd sweep in higher current region. The remaining mass of polymer on the nanostring after these current sweeps was 241 pg.

Table 5.4: Qualitative measurement of desorption of polymer of the 215 μm long polymer coated device using frequency shift after each current sweep, which was taken from Fig. 5.9. The total mass of the device was taken from table 5.1, which is 1251 pg and the effective mass of the device is 626 pg.

Sweep No.	Initial frequency f kHz	Frequency shift Δf kHz	Effective mass of string m_{eff} pg	Desorption of polymer Δm pg
1st	710.7	21.9	626	38
2nd	732.5	28.8	587	46

I repeated the same measurement using different device dimensions. In this case, I used a nanostring of length 195 μm. Here, resonance frequency was measured as a function of current for 5 different current sweeps, which is presented in Fig. 5.10. It shows that the resonance frequency shifts to the upper value after each current sweep which is presented in table 5.5. Note that I could not measure the frequency shift for 5th sweep because of destroying the nanostring during the 5th sweep in higher current

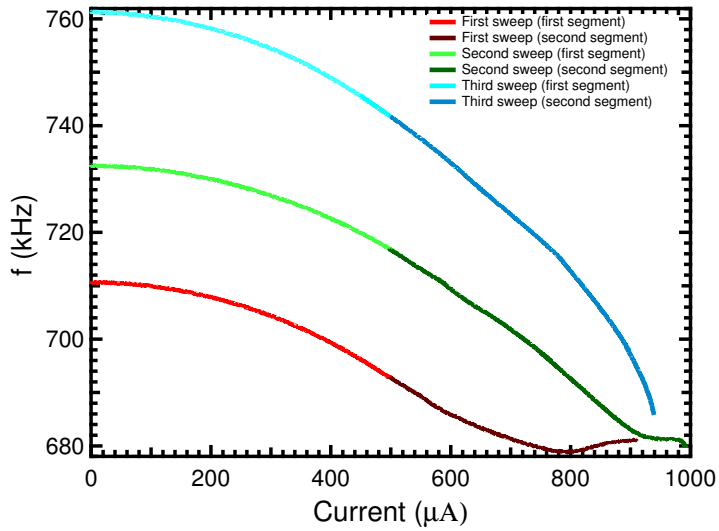

Figure 5.9: Resonance frequency as a function of current for different current sweeps of 215 μm long device. I used two different colours for each current sweep to indicate different segments of phase-locked loop data. The frequency shift after each current sweep is due to the desorption of polymer.

Table 5.5: Qualitative measurement of desorption of polymer of the 195 μm long polymer coated device using frequency shift after each current sweep which was taken from Fig. 5.10. The total mass of the device was taken from table 5.2, which is 933 pg and the effective mass of the device is 466.5 pg.

Sweep No.	Initial frequency f kHz	Frequency shift Δf kHz	Effective mass m_{eff} pg	Desorption of polymer Δm pg
1st	768.7	20.9	466.5	25
2nd	789.6	0.1	441.5	0.11
3rd	789.7	6.1	441.4	6
4th	795.7	43.9	435.4	48

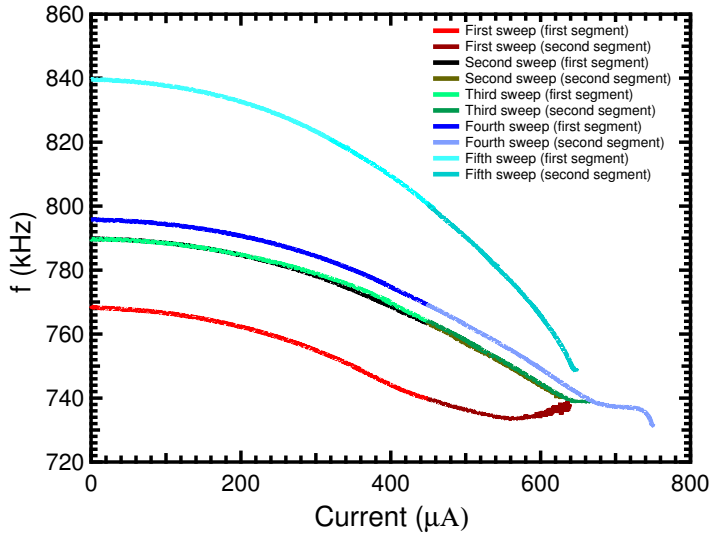

Figure 5.10: Resonance frequency as a function of current for different current sweeps of 195 μm long device. I used two different colours for each current sweep to indicate different segments of phase-locked loop data. The frequency shift after each current sweep is due to the desorption of polymer.

region. The desorption of polymer for different current sweeps was calculated using its initial frequency shift (when current is equal to zero), initial resonance frequency, and effective mass of the nanostring with the help of Eq. 2.43, which was tabulated in table 5.5.

To confirm the amount of remaining polymer mass on the nanostrings after the current sweeps, I took SEM images of the devices and measured the remaining mass from the thickness of polymer. The SEM of the 215 μm long and 195 μm long devices after current passing through them are presented in Fig. 5.11. It shows that the thickness of the polymer of the 215 μm long device was approximately 406 nm which was reduced by 37% of its initial thickness due to three current sweeps. It is also shown in Fig. 5.11(b) that polymer was removed from the device due to current passing through it. The calculated remaining mass of the polymer using the thickness of the polymer after current sweeps was 208 pg which was 13% lower than our expected mass (241 pg). Note that, I considered the uniform thickness

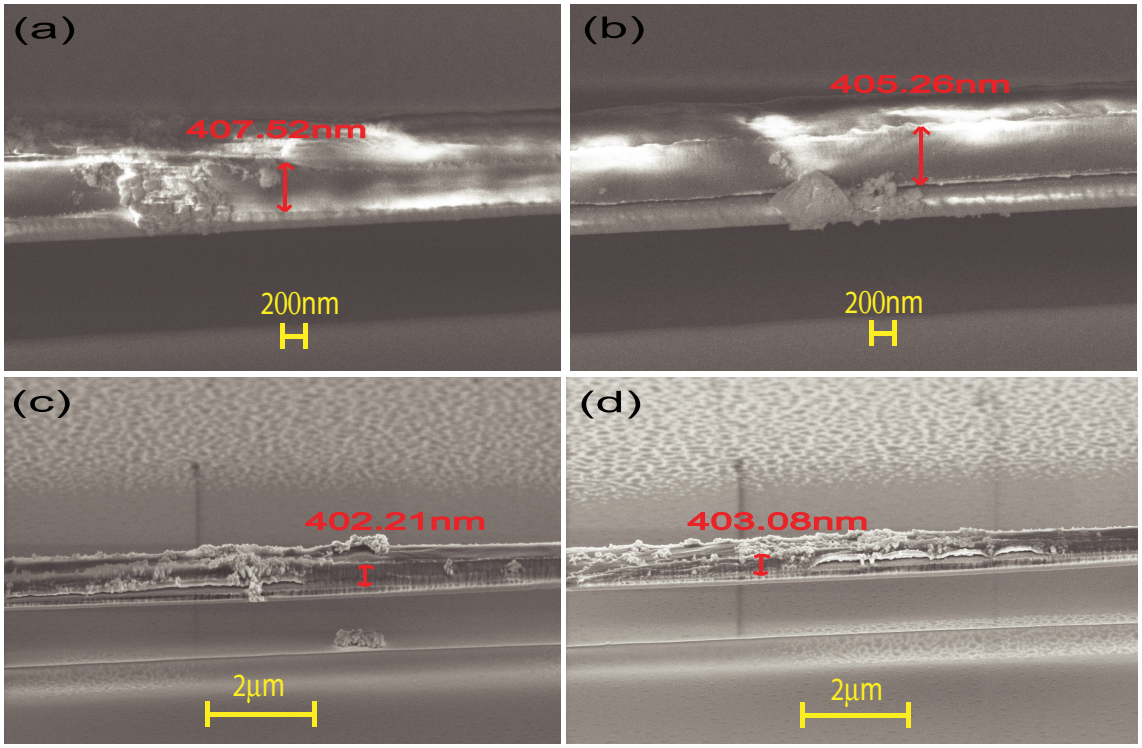

Figure 5.11: (a) SEM image of 215 μm long device after current sweeps. It shows that the thickness of the device after current sweeps is smaller around (406nm) than before (650 nm), (b) SEM image of the same device but different position. It shows that polymer is removed from the device due to Ohmic heating, (c) SEM image of 195 μm long device after current sweeps. (d) SEM image of the same device but different position.

(406 nm) of the whole polymer layer after current sweeps for mass calculation. But, SEM images show that the thickness of polymer was not uniform and it was thicker at the middle of the nanostring than at the ends. I also was not able to measure the desorption of polymer for the last current sweep due to destroying the device. Therefore, the 13% mass discrepancy between the nanostring frequency shift calculations and the SEM measurements may be due to the inaccurate measurement of the thickness of the polymer layer and the uncounted mass of the last current sweep.

The thickness of 195 μm long device using SEM images after current sweeps was around 402 nm, which corresponds the remaining mass of the polymer was 155 pg. On the other hand, the remaining calculated mass of the ethyl lactate polymer

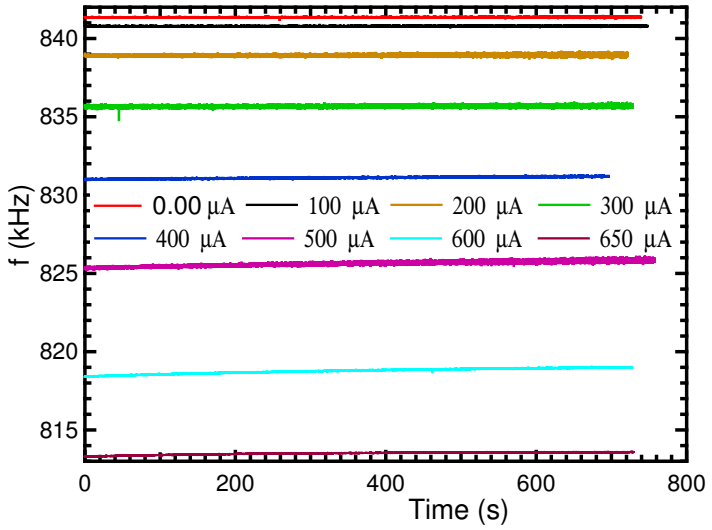

Figure 5.12: Resonance frequency as a function of time for different values of current for gold device. It describes that the resonance frequency is fairly constant with time for all values of current.

using the frequency shift of nanostring resonator was 171 pg. Likewise, the 9% mass discrepancy may be due to the inaccurate measurement of the thickness of the polymer layer and the uncounted mass of the last current sweep.

As mentioned before, the required time to complete a current sweep was around 2 minutes. Here, I passed current along the length of nanostring for approximately 12 minutes which was more than the required time to complete a single sweep. First, I measured the resonance frequency as a function of time without passing current (0 μA) along the nanostring for 12 minutes. After that, I set the current to 100 μA and measured the resonance frequency for another 12 minutes. I then set the current to 0 μA before proceeding with the next trial of the experiment. I followed this procedure for 8 different values of current (0 μA, 100 μA, 200 μA, 300 μA, 400 μA, 500 μA, 600 μA, and 650 μA), which are presented in Fig. 5.12 and Fig. 5.13 for gold and polymer coated nanostring, respectively. For gold coated nanostring, the resonance frequency is fairly constant with time for all current. This means that effective mass

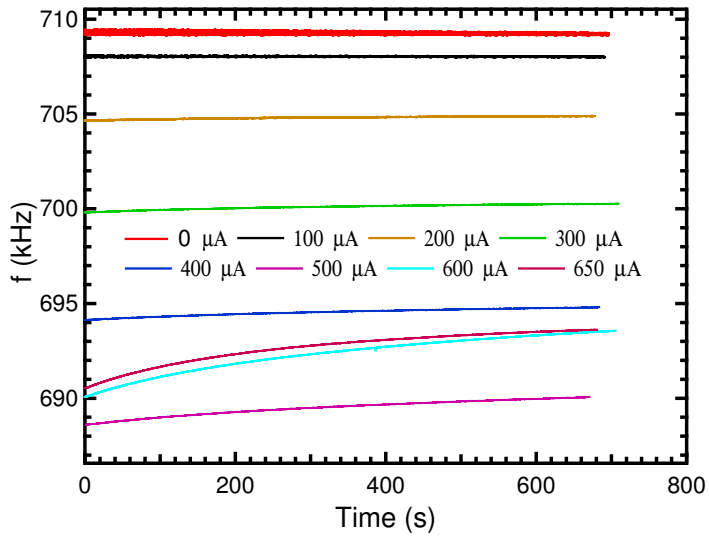

Figure 5.13: Resonance frequency as a function of time for different values of current for polymer coated device. It describes that the resonance frequency remains the same for lower current, but for higher current it changes significantly.

and the spring constant of the nanostring remain the same after setting a particular current of the device. Note that the resistance of the nanostring was measured before and after current sweep and found to be the same (165 Ω). Therefore, there was not any effect of current in the materials of the layers of the nanostring.

However, for polymer coated string, the resonance frequency shows the same behaviour as the gold device up to 400 μA, after this current, it increases with time. Note that that maximum resonance frequency increases for 600 μA current.

This behaviour indicates that at lower current (up to 400 μA), the mass of the polymer and spring constant remain the same. As a result, the resonance frequency does not change with time. However, at a particular value of higher current, the spring constant is the same but the polymer is removed from the nanostring resonator. As a result, the effective mass of the nanostring decreases with time like thermogravimetric analysis and the resonance frequency increases with time. I also measured the resistance of the polymer coated string before (167 Ω) and after (169 Ω) each current sweeps and found that they are very close. Note that, since the silicon nitride is insulating, the

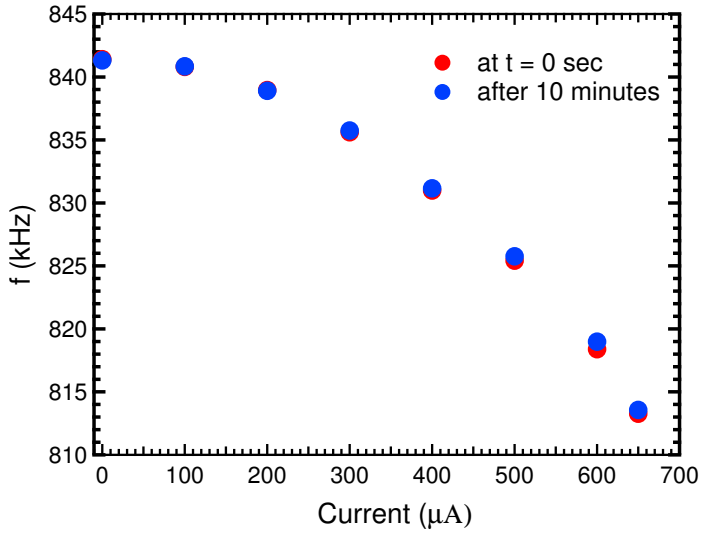

Figure 5.14: Resonance frequency as a function of current for two different waiting time of current (gold nanostring). Blue one is at the starting time of current through the device and red one is after 10 minutes from the starting point.

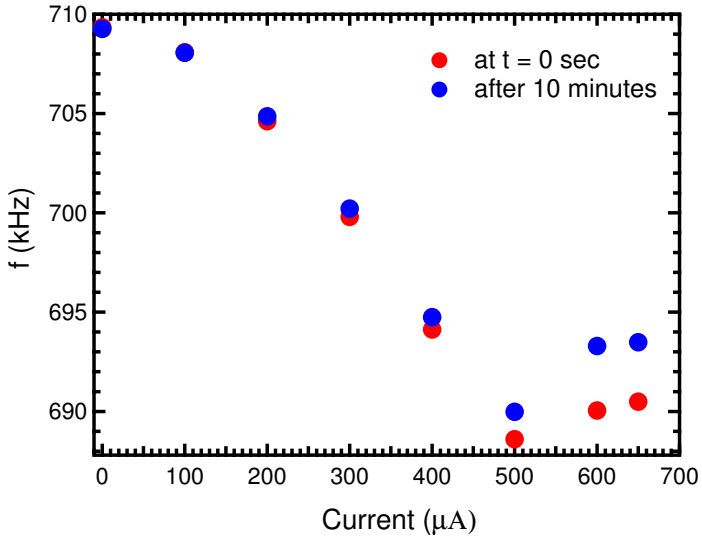

Figure 5.15: Resonance frequency as a function of current for two different waiting time of current (polymer coated nanostring). Blue one is at the starting time of current through the device and red one is after 10 minutes from the starting point.

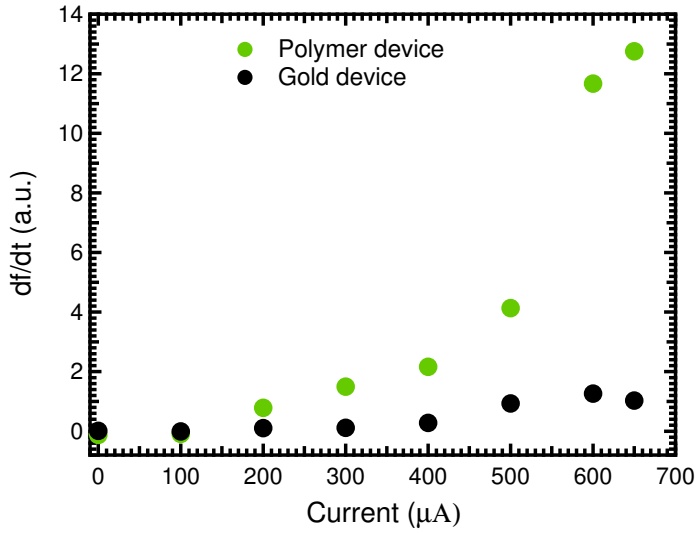

Figure 5.16: Derivative of the change in frequency of the nanostrings. Black circle is the gold nanostring and green circle is the polymer coated nanostring. It is shown that up to 400 μA the derivative (black circle) is constant for gold device, after that it increases a little bit. However, for polymer coated device, the derivative increase sharply, and there is a big jump from 500 μA to 600 μA.

resistance of the device depends on the metallic layer of Cr and Au. If the resistance of the device remains the same by passing current along the length of the device, then these two metallic layers are not affected by current. Thus, the mass reduction of the nanostring is only the desorption of polymer not any other materials of the nanostring.

The resonance frequency as a function of current for two different times (one is at the starting time, $t = 0$ s and another one is after 10 minutes from the beginning, $t = 10$ minutes) of gold string is plotted in Fig. 5.14. Figure 5.14 shows that the measured resonance frequency for two different times are the same for a particular current. However, in case of polymer coated nanostring, the resonance frequency for the measurement after 10 minutes shifts to a significantly higher value with respect to starting time (t =0 s) for high current, which is presented in Fig. 5.15. That means the mass of the polymer is removed from the device for high current during 10 minutes period.

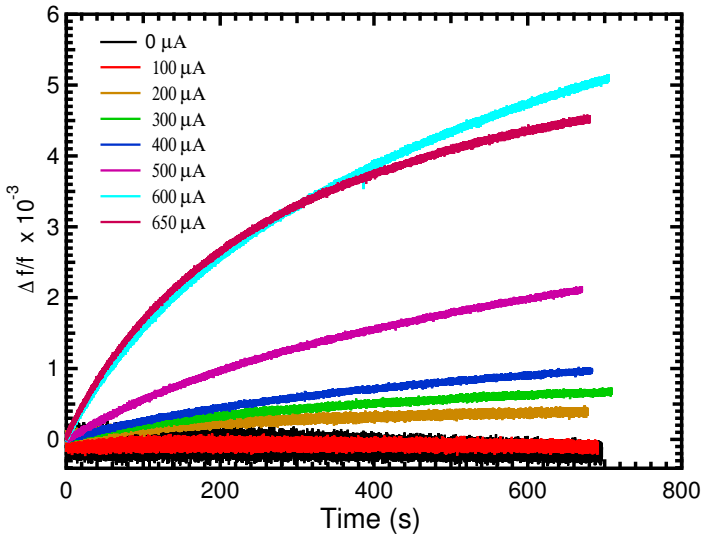

Figure 5.17: Relative resonance frequency shift as a function of time for different values of current for polymer coated device. It describes that the relative resonance frequency shift remains the same (close to zero) for lower current (from 0 μA to 400 μA), but for higher current it changes significantly.

Here, I calculated the initial derivative (when t = 0 s) of resonance frequency with respect to time using Fig. 5.12 and Fig. 5.13 for the gold coated silicon nitride and the polymer coated devices, respectively. The calculated initial slope of them are plotted as a function of current in Fig. 5.16. It shows that for the gold device, the derivative of resonance frequency is the same (close to zero) up to 400 μA and then increases a little bit. This small increase may be due to the desorption of unknown molecules/particles which were attached to the nanostring from the chamber or during the fabrication process. On the other hand, the derivative of resonance frequency increases sharply with current for polymer coated device. It shows that for small current, the derivative of frequency is as same as the gold device (close to zero), therefore, there is no desorption of polymer at low current. However, for 650 μA current, the rate of change of frequency is 13.2 (a.u.). Therefore, the derivatives of the frequency change, $\frac{df}{dt}$ for polymer coated nanostring (green circle) reveals the desorption rate of the polymer.

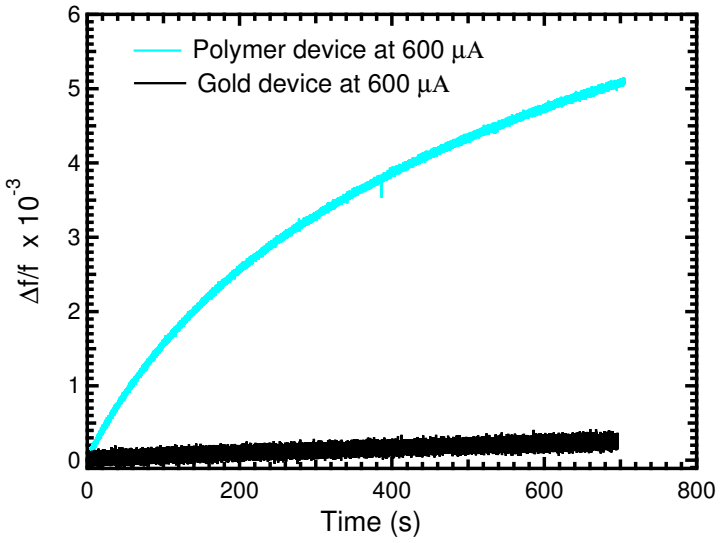

Figure 5.18: Resonance frequency shift as a function of time for both gold and polymer coated string at current 600 μA. It describes that the relative resonance frequency shift is linear and close to zero for gold device but for polymer coated device, it increases sharply.

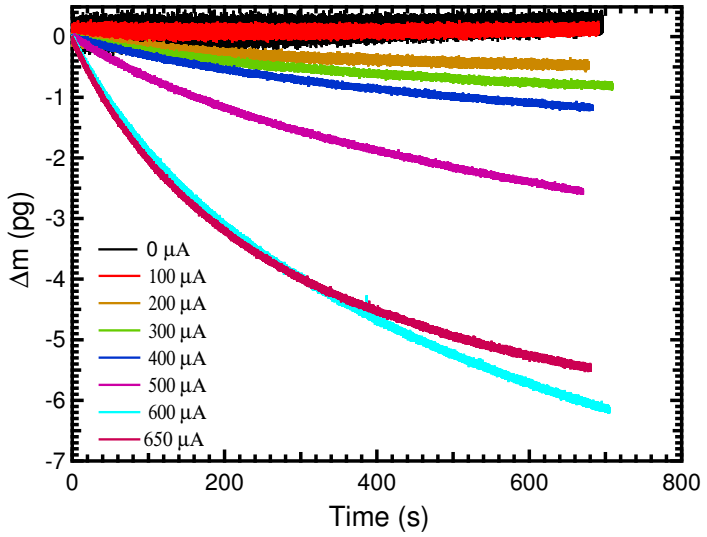

Figure 5.19: Desorption of ethyl lactate polymer as a function of time for different values of current. It describes that there is no desorption of polymer at lower current, but for higher current it occurs significantly.

For quantitative measurements of desorption of the polymer, I plotted the relative resonance frequency shift as a function of time for 8 different values of current (0 μA, 100 μA, 200 μA, 300 μA, 400 μA, 500 μA, 600 μA, and 650 μA), which are shown in Fig. 5.17. Figure 5.17 was extracted from Fig. 5.13, where $\frac{\Delta f}{f}$ is the relative resonance frequency and f is the initial resonance (when t = 0 s) frequency of that corresponding current. It shows that for currents below 400 μA, the relative resonance frequency shift with time is close to zero. When the value of current increases, the relative resonance frequency shift increases sharply as shown in Fig. 5.17. The maximum relative resonance frequency shift is found for 600 μA current.

Table 5.6: Desorption of polymer for 10 minute period for different values of current. It was calculated using Eq. 2.43, where $\frac{\Delta f}{f}$, the relative resonance frequency, was taken from the Fig. 5.17 and f was the initial resonance frequency of that corresponding current.

Time Period minute	Current μA	Desorption of mass pg
	0	0.00
	100	0.06
	200	0.45
	300	0.73
10	400	1.87
	500	2.39
	600	5.76
	650	5.28

Next, I compared the relative resonance frequency of the polymer coated nanostring as a function of time with the gold coated silicon nitride nanostring for the same current (600 μA current) in Fig. 5.18. We see that, for the gold coated silicon nitride nanostring, the relative frequency shift is close to zero, however, for the polymer coated device, it increases sharply. This is an indicator that the mass of the polymer changes with time due to ohmic heating like thermogravimetric analysis.

Finally, the desorption of the polymer was calculated using Eq. 2.43, where $\frac{\Delta f}{f}$, the relative resonance frequency is taken from the Fig. 5.17 and f is the initial resonance

frequency of that corresponding current. The obtained desorption of the polymer as a function of time is presented in Fig. 5.19. The amount of desorption of the polymer for a 10 minute period for each current was calculated from Fig. 5.19 and presented in Table 5.6.

Table 5.6 shows that, for small current (from 0 μA to 300 μA), the desorption of the ethyl lactate polymer was close to zero. After 400 μA current, the desorption of polymer increases with time significantly. The maximum desorption of ethyl lactate polymer was found for 600 μA current and it was 5.76 pg for the 10 minute period.

In conclusion, thermogravimetric analysis was demonstrated on a 325 pg polymer deposited on the nanostring resonators. One of the nanostring was used as a reference resonator (gold coated nanostring) and the another (polymer coated gold nanostring) was used to characterize the thermally activated desorption of the polymer. The desorped polymer was measured from the change in resonant frequency due to local heating.

Chapter 6

Results of Acetone Detection

In Chapter 5, we see that Ohmic heating is sufficient to remove polymer from the nanostring. Now, we would like to use the Ohmic heating for chemical signature of molecules particularly acetone. Acetone is a colourless, volatile flammable liquid, which is normally produced during biosynthetic processes and escapes the body through the exhaled breath of a person with certain diseases, such as diabetes and lung cancer [41, 42]. The main challenge for acetone detection is that it does not stick well to the surface of nanostrings. There are two different process to stick the molecules on the nanostring surface which are chemisorption and physisorption. In this chapter, I will discuss an attempt of the physisorption of acetone on the gold coated silicon nitride nanostring.

I modified the experimental setup for the attempt of physisorption of acetone molecules. We attached a beaker of liquid acetone to the vacuum chamber through two valves. A Peltier element was inserted between the chip holder and piezoelectric buzzer in the vacuum chamber which is controlled by a thermoelectric temperature controller (TEC). In addition, we placed a resistance temperature detector (PT-1000) to measure the temperature of the chip.

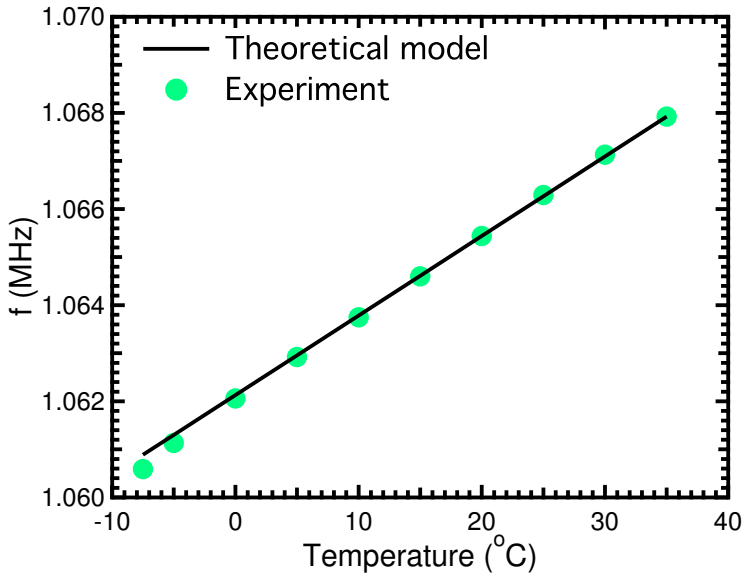

Figure 6.1: Resonance frequency of the fundamental mode in vacuum versus temperature as the chip is heated by Peltier element without filling the chamber with acetone vapour. Black line is theoretical model by Eq. 6.2, where $f_n(T_0)$ (1066.295 kHz) is the resonance frequency at room temperature and cyan circular dots are the experiment.

After modifying the measurement setup, I mounted a 10 mm $\times$ 15 mm gold coated silicon nitride chip, which has 4 nanostrings. Then, the vacuum chamber was pumped out around 2×10^{-6} Torr. The chip was then cooled down from 35° C to $-7.5°$ C in steps of 5° C and the temperature was allowed to stabilize before the resonance frequency was measured. The temperature dependent resonance frequency of a 205 μm long nanostring was measured without filling the chamber with acetone vapour. Figure 6.1 shows the variation of resonance frequency with temperature. It shows the frequency decreasing linearly with temperature. The frame material (Si) is compressing less than the nanostring materials (Au, Cr and Si_3N_4) with decreasing temperature. Thus the nanostring's strain is reduced as the temperature goes down. Because of this, the tensile stress in the string decreases which results in a lower resonance frequency [36].

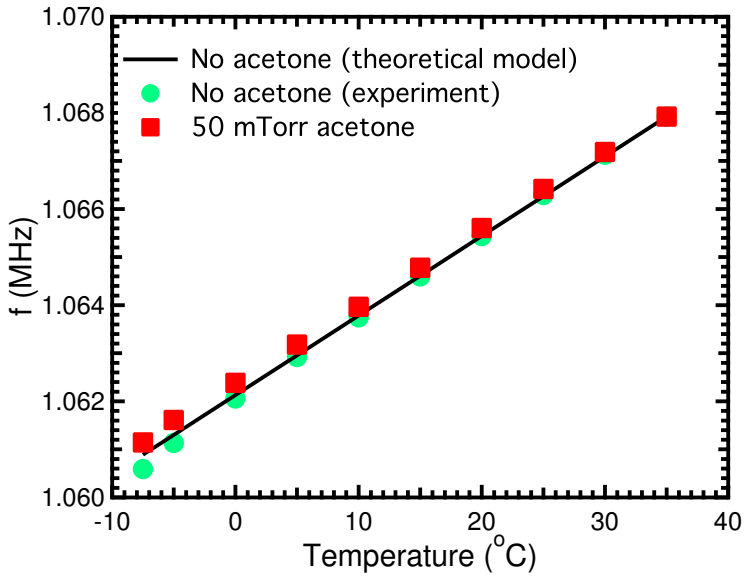

Figure 6.2: Resonance frequency of the fundamental mode in vacuum versus temperature for both without and with 50 mTorr acetone vapor. Both follow the same nature. The black line is the theoretical model by Eq. 6.2 in the case of without acetone, where $f_n(T_0)$ (1066.295 kHz) is the resonance frequency at room temperature.

Tushar *et al.* [34] also have established a theoretical model to explain the global temperature effect on nanostring. They have derived the linearized relative frequency shift for small temperature changes, which is

$$\frac{f_n(T) - f_n(T_0)}{f_n(T_0)} = -\left[\frac{1}{2\sigma A_1}\sum_{k=1}^{3} A_k E_k \alpha_{k,o}\right]\Delta T, \tag{6.1}$$

where $\alpha_{k,0} = \alpha_k - \alpha_0$ are the relative thermal expansion coefficients measured with respect to that of substrate, α_0. Note that, $f_n(T)$ and $f_n(T_0)$ are the resonance frequency at temperature T and room temperature, T_0, respectively and $\Delta T = T - T_0$. The parameters E_k, A_k and σ are the corresponding Young's modulus, cross-sectional areas and tensile stress (Si_3N_4), respectively. The material parameters are defined for each layer with indices $k = 1$ (silicon nitride), $k = 2$, (chromium), and $k = 3$ (gold).

Equation 6.1 describes a relative frequency shift that is linear with temperature. I calculated the slope of Eq. 6.1, $\left[\frac{1}{2\sigma A_1}\sum_{k=1}^{3} A_k E_k \alpha_{k,o}\right]$ to be 1.30×10^{-4} K^{-1} using the numerical values of nanostring parameters from table 5.1 and 5.3. Thus, Eq. 6.1 can be written as

$$\frac{f_n(T) - f_n(T_0)}{f_n(T_0)} = -1.30 \times 10^{-4} \Delta T. \tag{6.2}$$

Then, I extracted the resonance frequency using Eq. 6.2, where $f_n(T_0)$ (1066.295 kHz) is the resonance frequency at room temperature, and compared it with our experimental data in Fig. 6.1. The obtained data shows a good agreement with the theoretical model.

For the attempt of the physisorption of acetone, the vacuum chamber was slowly filled with 50 mTorr of acetone vapour at room temperature. The amount of injected acetone vapour was calculated using the pressure measured by a thermocouple (TC) vacuum gauge, which is calibrated with nitrogen gas, then divided by the acetone gas correction factor of 2.09 [79]. The chip was then cooled down from 35° C to −7.5° C in steps of 5° C and the temperature was allowed to stabilize before the resonance frequency was measured. The obtained resonance frequency was plotted in Fig. 6.2. The resonance frequency of experimental data and theoretical model without acetone are also plotted in Fig. 6.2. It shows that all three graphs provide exactly the same linear behaviour. It also indicates that the frequency for 50 mTorr acetone vapour graph is little bit higher than without acetone at lower temperatures (for 0° C, −5° C and −7.5° C). However, if acetone molecules form a monolayer film on the surface of the 205 μm long nanostring at lower temperatures such as 0° C, −5° C and −7.5° C, then the additional mass of physisorped acetone molecules would reduce the resonance frequency of the nanostring by 112 Hz (detailed calculation in the Appendix A). Hence we can say that the acetone is not physisorped on the string

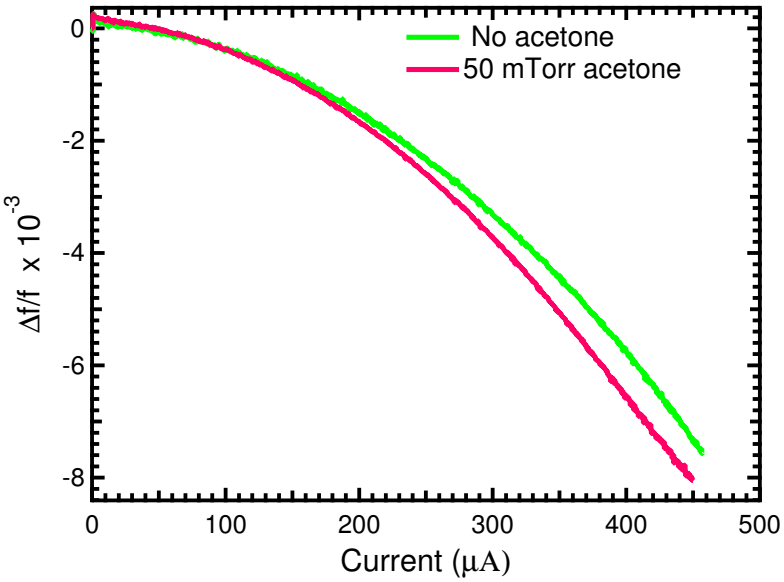

Figure 6.3: Relative resonance frequency in vacuum versus current for both without and with 50 mTorr acetone vapour at $-7.5°$ C.

at these low temperatures when the chamber is filled with 50 mTorr acetone vapour. I repeated this experiment several times by filling the vacuum chamber with different amount of acetone vapour (25 mTorr, 75 mTorr, 150 mTorr, and 250 mTorr) and found the same results.

Next, I set the temperature of the chip to $-7.5°$ C and stabilized the resonance frequency of the nanostring. For local heating of string resonators, a constant DC current source (Keithley 2401)-controlled by lab view, was connected across the string. The current was raised at the rate 7.5 μA/s, and the resonance frequency was tracked as a function of current without acetone vapour. After taking this measurement, we filled the chamber with 50 mTorr of acetone in the same environment of $-7.5°$ C temperature. Again, I measured the resonance frequency as a function of current. Figure 6.3 shows the relative resonance frequency as a function of current for both without and with 50 mTorr acetone vapour at $-7.5°$ C. It shows that the relative frequency shift for both cases decreases with current due to the local heating of the string, which is explained in detail in Chapter 5. If the acetone vapour is

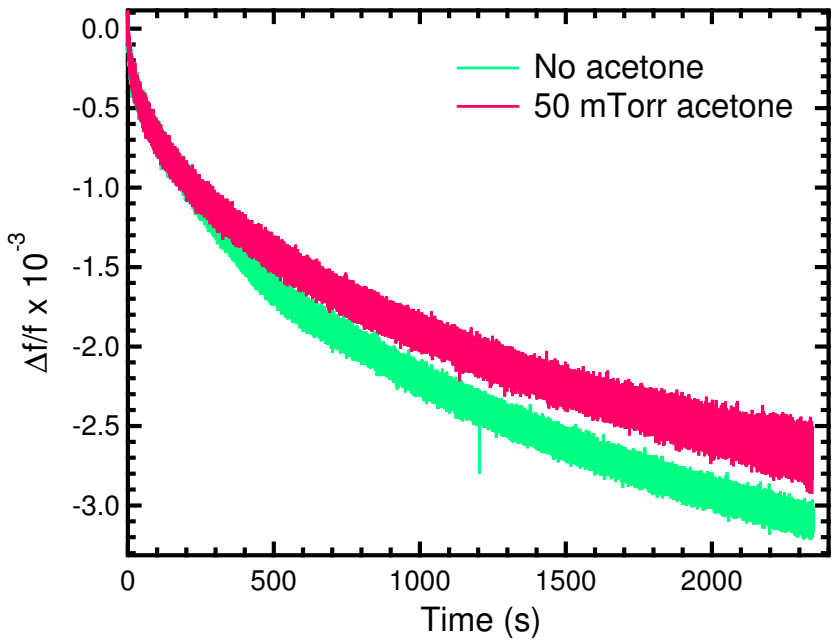

Figure 6.4: Relative resonance frequency shift in vacuum as a function of time at -7.5^o C for both without and with 50 mTorr acetone vapour.

physisorped on the nanostring surface at $-7.5°$ C in the presence of 50 mTorr acetone vapour, then the relative resonance frequency shift would show a sharp shift at higher current, similar behaviour of polymer which is presented in Fig. 5.7. A higher current produces more local heating on the surface of the string and as a result, the volatile physosorped acetone would be evaporated suddenly at a higher current. Therefore, the effective mass of the string resonator would decrease suddenly and relative frequency shift would increase sharply. However, this behaviour is not present here which indicates the absence of physisorption of acetone vapour on the nanostring surface at $-7.5°$ C in the presence of 50 mTorr acetone vapour. This experiment was also repeated several times at $-7.5°$ C with varying the amount of acetone vapour (25 mTorr, 75 mTorr, 150 mTorr, and 250 mTorr) and found the same results.

The final attempt to test the presence of physisorped acetone on the nanostring, I again fixed the temperature of the chip to $-7.5°$ C and stabilized the resonance

frequency of the nanostring. In this case, I mounted a 215 μm long nanostring and tracked the resonance frequency in real time without acetone vapour. Then, the vacuum chamber was filled with 50 mTorr acetone vapour. After getting stable resonance frequency, the resonance frequency was tracked by PLL in real time. The relative resonance frequency shift for both without and with acetone was calculated and presented in Fig. 6.4. This figure shows that the relative resonance frequency shift for both cases decrease with time. The decrease of relative resonance frequency shift with time is due to the deposition of unknown molecules, possibly water which is inside the chamber, but not acetone molecules. This was determined from the relative frequency shift with 50 mTorr acetone vapour which was 2.73×10^{-3}, less that the relative frequency shift without acetone vapour, 3.12×10^{-3} for the same time period of 30 minute. If the acetone is physisorped on the nanostring resonator at $-7.5°$ C in the presence of 50 mTorr acetone vapour, then the relative resonance frequency shift with acetone vapour would be larger than without acetone due to the additional deposition of acetone on the string. Therefore, we can say that the acetone vapour is not physisorped at $-7.5°$ C on nanostring when the chamber is filled with 50 mTorr acetone vapour.

In conclusion of this chapter, the resonance frequency was studied as a function of temperature for both cases, without and with different amount of injected acetone (maximum up to 250 mTorr). The variation of relative resonance frequency shifts with current and time were studied at $-7.5°$ C for both without and with different values of acetone vapour (maximum up to 250 mTorr). All measurements show that the temperature of $-7.5°$ C and vapour pressure of acetone up to 250 mTorr are not sufficient to physisorb acetone vapour on the nanostring surface. However, we could not go beyond $-7.5°$ C using our existing thermoelectric temperature controller and

Peltier element, and are able to measure the resonance response of nanostring up to the maximum of 250 mTorr amount of acetone vapour.

Chapter 7

Conclusions

In this study, I had two goals: first one was the detection of mass of ethyl lactate polymer and second one was detection of acetone molecules using nanostring resonators. For achieving these goals, I fabricated two types of nanostring resonators: gold coated silicon nitride nanostrings and gold nanostrings coated in a ethyl lactate polymer. Optical lithography technique, and both dry and wet etching techniques were used to fabricate both types of nanostrings. A highly sensitive interferometric technique was used to measure the motion of nanostring. The nanostring was actuated using a piezo element at above room temperature for mass detection of polymer and below room temperature for the detection of acetone in high vacuum.

For the detection of polymer, the gold coated silicon nitride nanostring was mounted in a vacuum chamber and a constant current source was connected across it. Then, the current dependent resonance frequency was measured as a reference. After that, the same measurement was taken for the polymer coated nanostring. The relative resonance frequency shift was extracted for both types of nanostrings from the resonance frequency.

In order to get a qualitative measurement of desorption of the polymer, we measured the resonance frequency as a function of current for different current sweeps using different lengths of nanostrings (lengths 195 μm and 215 μm). The desorption of the polymer was calculated from the frequency shift after the completion of each current sweep. The calculated results were then compared with the desorption of polymer measured using the thickness of the polymer layer after current sweeps. We found that the mass discrepancy of 195 μm long and 215 μm long nanostrings were 9% and 13%, respectively. This mass discrepancy might be due to the inaccurate measurement of the thickness of the polymer layer after current sweeps and the uncounted mass of the last current sweep.

Finally, thermogravimetric analysis was demonstrated on both the gold coated silicon nitride and polymer coated gold nanostrings. The gold coated silicon nitride nanostring was used as a reference resonator and the other was used to characterize the thermally activated desorption of the polymer. The resonance frequency as a function of time for different values of current was measured for both nanostrings. Then the relative resonance frequency shift and the desorption of polymer were extracted from the resonance frequency as a function of time.

For the detection of acetone molecules, I tried to physisorb acetone on the gold coated silicon nitride nanostring. To do this, I cooled down a chip of 4 devices from 35° C to −7.5° C in step of 5° C and simultaneously measured the resonance frequency. The same measurement was repeated using the same device in the presence of different amount of acetone vapour (maximum up to 250 mTorr). The compared results for resonance frequency both with and without acetone are similar. In fact, the resonance frequency with acetone is higher than without acetone at lower temperature (0° C, −5° C and −7.5° C) which is the opposite of our expectations

due to additional mass of physisorped acetone.

Finally, I set the temperature of the chip to $-7.5°$ C and stabilized the resonance frequency of the nanostring. When the resonance frequency was stable, the resonance frequency was tracked as a function of current, without and with different amount of acetone vapour (maximum up to 250 mTorr). In addition, the variation of relative resonance frequency with time also was studied at $-7.5°$ C for both cases (with different amount of injected acetone vapour (maximum up to 250 mTorr) and without acetone). These measurements confirmed that acetone vapour was not physisorped at $-7.5°$ C when the vacuum chamber was filled with up to 250 mTorr acetone vapour.

7.1 Future work

In this study, we developed a measurement technique for the detection of small masses of polymer, based on changes in the resonant frequency due to the Ohmic heating along the nanostring resonator. However, we could not achieve our second goal, which was the detection of physisorped acetone on the nanostring resonator. We made the following suggestions to detect the physisorption of acetone on a gold coated nanostring resonator:

We tried to physisorb acetone vapor at $-7.5°$ C on the nanostring surface. Here we set the temperature of the nanostring to $-7.5°$ C at first using the combination of Peltier element and thermoelectric temperature controller and then vacuum chamber was filled with different amount of acetone vapour (maximum up to 250 mTorr). Note that we could not reach beyond $-7.5°$ C temperature due to the limitations of the cooling systems and are able to measure the resonance response of nanostring up to the maximum of 250 mTorr amount of acetone vapour.

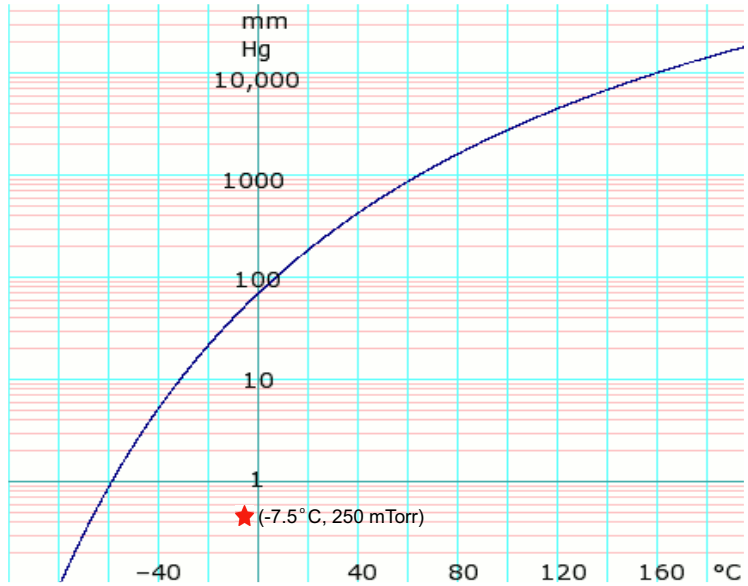

Figure 7.1: Vapour pressure of acetone (log scale) based on formula $\log_{10} P_{mmHg} = 7.02474 - \frac{1161.0}{224+T}$ from [85]. The red star point on the graph indicates the temperature that we can reach using our existing cooling system, and the maximum pressure that we can measure the frequency response of nanostring.

From the vapour pressure curve of acetone in Fig. 7.1, we see that the saturated vapour pressure of acetone at $-7.5°$C is 50 Torr, i.e. 200 times larger than the maximum acetone pressures of 250 mTorr. The temperature at which acetone would condense at 250 mTorr is much lower, about $-72°$C.

An acetone film will be adsorbed on the nanostring's surface at lower pressure or higher temperature but its thickness depends on how close the system is to the saturated vapour pressure. The authors in Ref. [86] studied the ellipsometric thickness (the difference of the ellipsometric angle between the film covered and the bare substrate) and corresponding layer index of an acetone film on the surface of graphite at 184 K as a function of the relative vapour pressure, p/p_∞ of acetone, where p_∞ is the saturated vapour pressure of acetone. As shown in Fig. 7.2 the thickness of the adsorbed acetone on the graphite surface is about 1.6 layers when p/p_∞ is between 0.2 and 0.8. When the pressure is $p/p_\infty \geq 0.8$, i.e. close to the

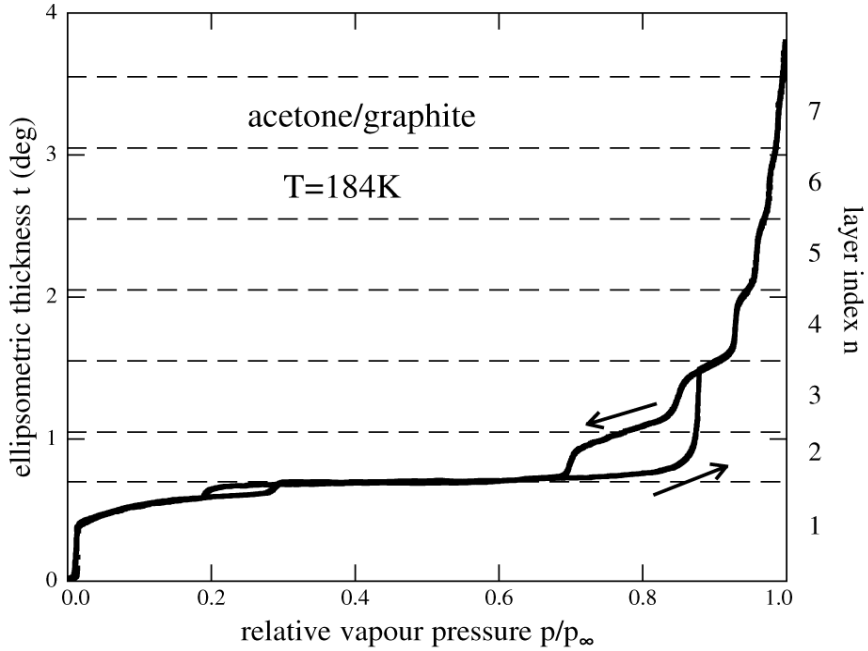

Figure 7.2: Ellipsometric thickness and layer index of adsorbed acetone on graphite surface as a function of relative vapour pressure at 184 K. This graph is taken from [86].

saturated vapour pressure, then the thickness of the physisorped film increases rapidly.

A monolayer film would be expected at much lower pressure, example for $p/p_\infty \approx 0.01$ (see Fig. 7.2). For example, if the nanostring is at $-7.5°$ C, a monolayer might be adsorbed if $p \approx 0.01 p_\infty \approx 500$ mTorr. At a pressure of 250 mTorr, the string would need to be cooled to about $-20°$ C to adsorb a monolayer and below $-70°$ C to adsorb a thick film.

The precision of the resonance frequency measurement of our technique is 1 Hz. However, the frequency shift of the 205 μm long nanostring would be 112 Hz (detailed calculation in Appendix A) due to formation of a uniform monolayer film of acetone on it. Therefore, the mass of physisorped acetone would be detected but only if the temperature of the nanostring and pressure of the acetone vapour are close enough

to the saturated vapour pressure curve of acetone. However, we would not be able to confirm that the frequency shift of the nanostring is due to the mass of adsorbed acetone molecules on the nanostring, because water or some other molecules could also be asdorbed on the nanostring at low temperature.

Bibliography

[1] R. H. Bishop. *The Mechatronics Handbook*. CRC Press, USA, 2002.

[2] G. Coussot. Electromechanical resonance device and its application to filtering of television signals. *US Patent*, US5920417A, July 6, 1976.

[3] M. D. Johnson. Microelectromechanical television scanning device and method for making the same. *US Patent*, US3968462A, July 6, 1999.

[4] D. Rugar, R. Budakian, H.J. Mamin, and B.W. Chui. Single spin detection by magnetic resonance force microscopy. *Nature*, **430**: 329 (2004).

[5] R. Budakian, H. J. Mamin, and D. Rugar. Spin manipulation using fast cantilever phase reversals. *Applied Physics Letters*, **89**: 113113 (2006).

[6] Y. T. Yang, C. Callegari, X. L. Feng, K. L. Ekinci, and M. L. Roukes. Zeptogram-scale nanomechanical mass sensing. *Nano Letters*, **6**: 583 (2006).

[7] M. Li, H. X. Tang, and M.L. Roukes. Ultra-sensitive NEMS-based cantilevers for sensing, scanned probe and very high-frequency applications. *Nature Nanotechnology* , **2**: 114 (2007).

[8] A. K. Naik, M. S. Hanay, W. K. Hiebert, X. L. Feng, and M.L. Roukes. Towards single-molecule nanomechanical mass spectrometry. *Nature Nanotechnology*, **4**: 445 (2009).

[9] A. D. O′Connell, M. Hofheinz, M. Ansmann, R. C. Bialczak, M. Lenander, E. Lucero, M. Neeley, D. Sank, H. Wang, M. Weides, J. Wenner, J. M. Martinis, and A. N. Cleland. Quantum ground state and single-phonon control of a mechanical resonator. *Nature*, **464**: 697 (2010).

[10] C. Doolin, P. H. Kim, B. D. Hauer, A. J. R. MacDonald, and J.P. Davis. Multidimensional optomechanical cantilevers for high-frequency force sensing. *New Journal of Physics*,**16**: 035001 (2014).

[11] M. R. Paul, M. T. Clark, and M. C. Cross. The stochastic dynamics of micron and nanoscale elastic cantilevers in fluid: fluctuations from dissipation. *Nanotechnology*, **17**: 4502 (2006).

[12] J. Tamayo, M. Calleja, D. Ramos, and J. Mertens. Underlying mechanisms of the self-sustained oscillation of a nanomechanical stochastic resonator in a liquid. *Physical Review B*, **76**: 180201 (2007).

[13] R. L. Badzey, and P. Mohanty. Coherent signal amplification in bistable nanomechanical oscillators by stochastic resonance. *Nature*, **437**: 995 (2005).

[14] T. Kwon, K. Eom, J. Park, D. S. Yoon, H. L. Lee, and T. S. Kim. Micromechanical observation of the kinetics of biomolecular interactions. *Applied Physics Letters*, **93**: 173901 (2008).

[15] T. P. Burg, M. Godin, S. M. Knudsen, W. Shen, G. Carlson, J.S. Foster, K. Babcock, and S. R. Manalis. Weighing of biomolecules, single cells and single nanoparticles in fluid. *Nature*, **446**: 1066 (2007).

[16] K. M. Goeders, J. S. Colton, and L. A. Bottomley. Microcantilevers: sensing chemical interactions via mechanical motion. *Chemical Reviews*, **108**: 522 (2008).

[17] T. P. J. Knowles, W. Shu, F. Huber, H. P. Lang, C. Gerber, C. M. Dobson, and M. E. Welland. Label-free detection of amyloid growth with microcantilever sensors. *Nanotechnology*, **19**: 384007 (2008).

[18] K. L. Ekinci, X. M. H. Huang, and M. L. Roukes. Ultrasensitive nanoelectromechanical mass detection. *Applied Physics Letters*, **84**: 4469 (2004).

[19] T. Braun, V. Barwich, M. K. Ghatkesar, A. H. Bredekamp, C. Gerber, M. Hegner, H. P. Lang. Micromechanical mass sensors for biomolecular detecti on in a physiological environment. *Physical Review E*, **72**: 031907 (2005).

[20] A. N. Cleland. Thermomechanical noise limits on parametric sensing with nanomechanical resonators. *New Journal of Physics*, **7**: 235 (2005).

[21] B. Lassagne, D. Garcia-Sanchez, A. Aguasca, and A. Bachtold. Ultrasensitive mass sensing with a nanotube electromechanical resonator. *Nano Letters*, **8**: 3735 (2008).

[22] K. Jensen, K. Kim, and A. Zettl. An atomic-resolution nanomechanical mass sensor. *Nature Nanotechnology*, **3**: 533 (2008).

[23] A. Suhel, B. D. Hauer, T. S. Biswas, K. S. D. Beach and J.P. Davis. Dissipation mechanisms in thermomechanically driven silicon nitride nanostrings. *Applied Physics Letters*, **100**: 173111 (2012).

[24] S. S. Verbridge, H. G. Craighead, and J. M. Parpia. A megahertz nanomechanical resonator with room temperature quality factor over a million. *Applied Physics Letters*, **92**: 013112 (2008).

[25] S. Schmid, and C. Hierold. Damping mechanisms of single-clamped and prestressed double-clamped resonant polymer microbeams. *Journal of Applied Physics*, **104**: 093516 (2008).

[26] J. Sulkko, M. A. Sillanpää, P. Häkkinen, L. Lechner, M. Helle, A. Fefferman, J. Parpia, and P. J. Hakonen. Strong gate coupling of high-Q nanomechanical resonators. *Nano Letters*, **10**: 4884 (2010).

[27] M. L. Roukes. Nanoelectromechanical Systems. arXiv:cond-mat/0008187v2.

[28] M. L. Roukes. Yoctocalorimetry: phonon counting in nanostructures. *Physica B*, **1**: 263 (1999).

[29] J. L. Arlett, E. B. Myers, and M. L. Roukes. Comparative advantages of mechanical biosensors. *Nature Nanotechnology*, **6**: 203 (2011).

[30] Y. K. Yoo, M. S. Chae, J. Y. Kang, T. S. Kim, K. S. Hwang, and J. H. Lee. Multifunctionalized cantilever systems for electronic nose applications. *Analytical Chemistry*, **84**: 8240 (2012).

[31] L. He, M. D. Musick, S. R. Nicewarner, F. G. Salinas, S. J. Benkovic, M. J. Natan, and C. D. Keating. Colloidal Au-enhanced surface plasmon resonance for ultrasensitive detection of DNA hybridization. *Journal of the American Chemical Society*, **122**: 9071 (2000).

[32] D. Saya, L. Nicu, M. Guirardel, Y. Tauran, and C. Bergaud. Mechanical effect of gold nanoparticles labeling used for biochemical sensor applications: A multimode analysis by means of SiNx micromechanical cantilever and bridge mass detectors. *Review of Scientific Instruments*, **75**: 3010 (2004).

[33] R. Sandberg, K. Molhave, A. Boisen, and W. Svendsen. Effect of gold coating on the Q-factor of a resonant cantilever. *Journal of Micromchabics and Microengineering*, **15**: 2249 (2005).

[34] T. S. Biswas, A. Suhel, B. D. Hauer, A. Palomino, K. S. D. Beach, and J. P. Davis. High-Q gold and silicon nitride bilayer nanostrings. *Applied Physics Letters*, **101**: 093105 (2012).

[35] S. P. Lacour, S. Wagner, Z. Huang, and Z. Suo. Stretchable gold conductors on elastomeric substrates. *Applied Physics Letters*, **82**: 2004 (2003).

[36] S. Bose, S. Schmid, T. Larsen, S. S. Keller, P. S. Larsen, A. Boisen, and K. Almdal. Micromechanical string resonators: analytical tool for thermal characterization of polymers. *ACS Macro Letters*, **3**: 55 (2014).

[37] C. Meyer, H. Lorenz, and K. Karrai. Optical detection of quasi-static actuation of nano-electromechanical systems. *Applied Physics Letters*, **83**: 2420 (2003).

[38] D. W. Carr, S. Evoy, L. Sekaric, A. Olkhovets, J. M. Parpia, and H. G. Craighead. Parametric amplification in a torsional microresonator. *Applied Physics Letters*, **77**: 1545 (2000).

[39] D. Karabacak, T. Touh, and K. L. Ekinci. Analysis of optical interferometric displacement detection in nanoelectromechanical systems. *Journal of Applied Physics*, **98**: 124309 (2005).

[40] T. Kouh, D. Karabaacak, D. H. Kim, and K. L. Ekinci. Diffraction effects in optical interferometric displacement detection in nanoelectromechanical systems. *Applied Physics Letters*, **86**: 013106 (2005).

[41] I. Horvath, Z. Lazar, N. Gyulia, M. Kollai and G. Losonczy. Exhaled biomarkers in lung cancer. *European Respirratory Journal*, **34**: 261 (2009).

[42] M. Li, S. Biswas, M. H. Nantz, R. M. Higashi, and X. Fu. A microfabricated preconcentration device for breath analysis. *Sensors and Actuators B*, **180**: 130 (2013).

[43] American Chemistry Council. Acetone VCCEP submission. **9**: (2003).

[44] T. Han, J. M. Williams, and T. P. Beebe. Chemical bonds studied with functionalized atomic force microscopt tips. *Analytica Chimica Acta*, **307**: 365 (1995).

[45] B. Ilic, D. Czaplewski, H. G. Craighead, P. Neuzil, C. Campagnolo, and C. Batt. Mechanical resonant immunospecific biological detector. *Applied Physics Letters*, **77**: 450 (2000).

[46] J. H. Pei, F. Tian, and T. Thundat. Glucose biosensor based on the microcentilever. *Analytical Chemistry*, **76**: 292 (2004).

[47] A. Venkatasubramanian, V. T. K. Sauer, S. K. Roy, M. Xia, D. S. Wishart, and W. K. Hiebert. Nano-optomechanical systems for gas chromatography. *Nano Letters*, **16**: 6975 (2016).

[48] M. Li, E. B. Myers, H. X. Tang, S. J. Aldridge, H. C. McCaig, J. J. Whiting, R. J. Simonson, N. S. Lewis, and M. L. Roukes. Nanoelectromechanical resonator arrays for ultrafast: Gas-phase chromatographic chemical analysis. *Nano Letters*, **10**: 3899 (2010).

[49] A. Wig, E. T. Arakawa, A. Passian, T. L. Ferrell, and T. Thundat. Photothermal spectroscopy of Bacillus anthracis and Bacillus cereus with microcantilevers. *Sensors and Actuators B*, **114**: 206 (2006).

[50] A. R. Krause, C. V. Neste, L. Senesac, T. Thundat, and E. J. Finot. Trace explosive detection using photothermal deflection spectroscopy. *Journal of Applied Physics*, **103**: 094906 (2008).

[51] T. Larsen, S. Schmid, L. G. Villanueva, and A. Boisen. Photothermal analysis of individual nanoparticulate samples using micromechanical resonators. *ACS Nano*, **7**: 6188 (2013).

[52] S. Yamada, S. Schmid, T. Larsen, O. Hansen, and A. Boisen. Photothermal infrared spectroscopy of airborne samples with mechanical string resonators. *Analytical Chemistry*, **85**: 10531 (2013).

[53] A. N. Cleland. *Foundations of Nanomechanics*. Springer, 2003.

[54] G. C. King. *Vibrations and Waves*. John Wiley and Sons Ltd, 2009.

[55] A. N. Cleland. *Foundations of Nanomechanics*. Springer-Verlag Berlin Heidelberg New York, (2002).

[56] S. D. Senturia. *Microsystem Design*. Kluwer Academic Publishers, 2001.

[57] A. Boisen, S. Dohn, S.S. Keller, S. Schmid, and M. Tenje. Cantilever-like micromechanical sensors. *Reports on Progress in Physics*, **74**: 036101 (2011).

[58] S. Schmid, *Organic Resonant MEMS Devices*, (2013).

[59] T. S. Biswas, J. Xu, N. Miriyala, C. Doolin, T. Thundat, J. P. Davis, and K. S. D. Beach. Time-resolved mass sensing of a molecular adsorbate nonuniformly distributed along a nanomechnical string. *Physical Review Applied*, **3**: 064002 (2015).

[60] B. D. Hauer, C. Doolin, K. S. D. Beach, and J. P. Davis. A general procedure for thermomechanical calibration of nano/micro-mechanical resonators. *Annals Physics*, **339**: 181 (2013).

[61] M. P. Norton, D. G. Karczub. *Fundamentals of Noise and Vibration Analysis for Engineers*. Cambridge University Press, Cambridge, UK, 2003.

[62] W. H. Press, S. A. Teukolsky, W. T. Vetterling, B. P. Flannery. *Numerical Recipes: The Art of Scientific Computing*, Cambridge University Press, Cambridge, UK, 2007.

[63] R. Bowley, M. Sanchez. *Introductory Statistical Mechanics*. Oxford University Press, Oxford, UK, 1999.

[64] W. K. Hiebert, D. Vick, V. Sauer, and M. R. Freeman. Optical interferometric displacement calibration and thermomechanical noise detection in bulk focused ion beam-fabricated nanoelectromechanical systems. *Journal of Micromchabics and Microengineering*, **20**: 115038 (2010).

[65] H. I. Rasool, P. R. Wilkinson, A. Z. Stieg, and J. K. Gimzewski. A low noise all-fiber interferometer for high resolution frequency modulated atomic force microscopy imaging in liquids. *Review of Scientific Instruments*, **81**: 023703 (2010).

[66] K. Prashanthi, A. Phani, and T. Thundat. Photothermal electrical resonance spectroscopy of physisorbed molecules on a nanowire resonator. *Nano Letters*, **15**: 5658 (2015).

[67] W. L. Huang, Z. Ren, and C. T. C. Nguyen. Nickel vibrating micromechanical disk resonator with solid dielectric capacitive-transducer gap. *IEEE International Frequency Control Symposium*, Miami, Florida, 839 (2006).

[68] M. L. Roukes. Nanoelectromechanical systems: Technical Digest of the 2000 Solid State Sensor and Actuator Workshop. Hilton Head Isl. SC, 6/4 - 8/2000 (ISBN 0-9640024-3-4).

[69] A. Agoston, F. Keplinger, B. Jakoby. Evaluation of a vibrating micromachined cantilever sensor for measuring the viscosity of complex organic liquids. *Sensors and Actuators A: Physical*, **123-12**: 82 (2005).

[70] Y. T. Yang, K. L. Ekinci, X. M. H. Huang, L. M. Schiavone, and M. L. Roukes C. A. Zorman and M. Mehregany. Monocrystalline silicon carbide nanoelectromechanical systems. *Applied Physics Letters*, **78**: 162 (2001).

[71] B. Ilic, Y. Yang, K. Aubin, R. Reichenbach, S. Krylov, and H. G. Craighead. Enumeration of DNA molecules bound to a nanomechanical oscillator. *Nano Letters*, **5**: 925 (2005).

[72] J. Mertens, C. Rogero, M. Calleja, D. Ramos, J. A. Martin-Gago, C. Briones, and J. Tamayo. Label-free detection of DNA hybridization based on hydration-induced tension in nucleic acid films. *Nature Nanotechnology*, **3**: 301 (2008).

[73] H. S. Park, and P. A. Klein. Surface cauchy-born analysis of surface stress effects on metallic layer. *Physical Review B*, **75**: 085408 (2007).

[74] H. S. Park, and P. A. Klein. A surface cauchy-born model for silicon nanostructures. *Computer Methods in Applied Mechanics and Engrineering*, **197**: 3249 (2008).

[75] S. Schmid, K. D. Jensen, K. H. Nielsen, A. Boisen. Damping mechanisms in high-Q micro and nanomechanical string resonators. *Phyical Review B*, **84**: 165307 (2011).

[76] S. S. Verbridge, D. S. Shapiro, H. G. Craighead, J. M. Parpia. Macroscopic tuning of nanomechanics: substrate bending for reversible control of frequency and quality factor of nanostring resonators. *Nano letters*, **7**: 1728 (2007).

[77] K. R. Williams, and R. S. Muller. Etch rates for micromachining processes. *Journal of Microelectromechanical systems*, **5(4)**: 256269 (1996).

[78] S. Franssila, *Introduction to Micro Fabrication*. John Wiley and Sons Ltd, 2nd Edition.

[79] K. Jousten. *Handbook of vacuum technology*. 2nd Edition, Wiley-VCH, Verlag GmbH and Co. KGaA, 2016.

[80] F. M. Garden. *Phaselock technique*. 3rd edition, (John wiley and sons, Hoboken, NJ, 2005).

[81] H. S. Wasisto, Q. Zhang, S. Merzsch, A. Waag, and E. Peiner. A phase-locked loop frequency tracking system for portable microelectromechanical piezoresistive cantilever mass sensors. *Microsystem Technologies* (Springer-Verlay Berlin Heidelberg 2013), **20**: 559 (2014).

[82] R. E. Best. *Phase-Locked Loops: Design, Simulation, and Applications*. 6th Edition, McGraw, Hill Professional, 2007.

[83] P. Anilaa, K. R. Reddya, G. S. Rao, P. V. S. Sairamb, D. Ramachandran, and C. Rambabu. Comparative studies of intermolecular interaction of aromatic amines with ethyl lactate at different temperatures. *The Journal of Chemical Thermodynamics*, **104**: 24 (2017).

[84] P. Anilaa, K. Rayapa Reddya, G. Srinivasa Raob, P. V. S. Sairamb, D. Ramachandran, and C. Rambabu. Densities, speed of sound, and IR studies of Ethyl lactate with 2-alkoxyethanols at different temperatures. *Thermochimica Acta*, **620**: 1 (2015).

[85] J. G. Speight. *Lange's Handbook of Chemistry*. 17th edition, (McGraw-Hill Education 2017).

[86] F. Kruchten and K. Knorr. Multilayer Adsorption andWetting of Acetone on Graphite. *Physical Review Letters*, **91**: 085502-1 (2003).

Appendix A

Frequency shift for a monolayer acetone

In this Appendix, we calculated the frequency shift of the nanostring due to an additional uniform monolayer formed by the adsorbed acetone molecues on it. The detail calculations are presented below:

The molar mass of acetone is 58.08 g/mol. So the mass of a single acetone molecule is, $m_s = \frac{\text{Molar mass}}{\text{Avogadro's number}} = 9.64 \times 10^{-23}$g.

The molecular radius of a acetone molecule is, $r_s = 0.308$ nm. So the surface area covered by a single acetone molecule is, $a_s = \pi r_s^2 = 0.298$ nm^2.

The surface area of a 205 μm long and 2.75 μm width nanostring is, A = 563750000 nm^2. If we assume that number of adsorbed acetone molecules on the surface is equal to the number of acetone molecules in a filled monolayer on the surface (the surface coverage is unity), then the number of acetone molecules covered by the whole nanostring surface is, $n = \frac{A}{a_s} = 1.89 \times 10^9$. Thus, the total mass of the adsorbed acetone molecules formed a monolayer on the nanostring surface is, $m_{\text{acetone}} = m_s \times n$ $= 1.82 \times 10^{-13}$ g. If we assume that the adsorbed acetone molecules are distributed uniformly on the whole nanostring surface, then the effective mass of the adsorbed

molecules is $\Delta m = m_{\text{acetone}}/2 = 9.1 \times 10^{-14}$ g. The total mass of the 205 μm long and 2.75 μm width nanostring is, $m_{\text{string}} = 8.63 \times 10^{-10}$ g (using the dimensions and density of the nanostring materials) and thus the effective mass of the nanostring is, m = $m_{\text{string}}/2 = 4.315 \times 10^{-10}$ g. From Fig. 6.1, the resonance frequency of the 205 μm long nanostring is, f = 1066.295 kHz. Using Eq. 2.43, the frequency shift for a uniform monolayer film of adsorbed acetone molecules on the whole nanostring surface is, Δf = - 112 Hz. However, if the same amount of acetone molecules (1.82×10^{-13} g) land at the middle on the nanostring surface, then the effective mass of the adsorbed acetone molecules is the same as the total mass of them. Therefore, the frequency shift due to adsorbed acetone molecules at the middle of the nanostring would be double (-224 Hz) with respect to the uniformly distributed adsorbed molecules on the whole nanostring surface.